A Multi-Scale Approach for the Control of Thermoelectric Properties in Bismuth Telluride Alloys Through Laser Powder Bed Fusion

---

A Dissertation

Presented to:

The Faculty of the School of Engineering and Applied Science

at the University of Virginia

In partial fulfillment of the requirements for the degree of

Doctor of Philosophy in Materials Science and Engineering

Prepared by:

Connor V. Headley

April 8th, 2024

APPROVAL SHEET

This Dissertation is submitted in partial fulfillment of the requirements for the degree of
Doctor of Philosophy

Headley

Author

The dissertation has been read and approved by the examining committee:

Ji Ma

Jon F. Ihlefeld

James M. Fitz-Gerald

S. Joseph Poon

Saniya LeBlanc

Accepted for the School of Engineering and Applied Science:

Jennifer L. West, School of Engineering and Applied Science
May 2024

Abstract

Thermoelectric (TE) materials have garnered interest over the past several decades as a potential solution to rampant industrial heat waste due to their ability to convert between heat and electrical energy directly and reversibly. However, their widespread adoption has been hindered by their low conversion efficiency (≈5 %) and high production cost. Laser powder bed fusion (LPBF) is an additive manufacturing (AM) technique with the ability to create free form geometries through layer-by-layer construction and reduce cost through the minimization of material waste and manufacturing steps. This work summarizes a series of hierarchical approaches to leverage LPBF and purposefully affect the TE properties of bismuth telluride alloys across multiple length-scales. First, through an iterative process of augmented machine learning and experimental validation, optimized LPBF processing parameters were rapidly identified for the construction of highly dense (>99 %), crack-free $Bi_2Te_{2.7}Se_{0.3}$ parts in nonstandard geometries. Second, an annealing-induced enhancement of TE efficiency was achieved, and potential mechanisms were explored. Specifically, manipulation of the point defect and charge carrier concentrations was proposed as a driver of improved electrical conductivity and Seebeck coefficient values, while simultaneous grain boundary manipulation provided the necessary pathway for a reduced thermal conductivity. Third, the ability to create intentional thermal and electrical transport behavior anisotropy was demonstrated through LPBF-induced crystallographic orientation control. Fourth, an ability to control the sign and magnitude of the Seebeck coefficient through LPBF processing parameter alterations was discovered. Possible methods for this experimental control were explored, including bismuth-rich oxide formation, matrix composition changes, and bulk porosity development. Ultimately, these studies collectively advance the control of TE properties using LPBF while providing a framework for broader AM material strategies.

Acknowledgements

In looking back at the last several years of my academic journey, it is sometimes difficult to wrap my head around how I got here and even harder to imagine where I would be without all those who have helped and supported me along the way. After nearly a decade as a student at UVA, I cannot understate the profound amount of gratitude that I have for those in my community. They say that it takes a village to raise a child and if that's true, then you can only imagine the city it took to turn this child at heart into the researcher and engineer that I can now proudly claim to be. I'll start by thanking my advisor, Prof. Ji Ma. I have the unusual distinction of predating my advisor in our department, so I got to see firsthand the level of excitement and commitment he brought to starting a new lab in a new city. Never before have I had the pleasure of meeting or experiencing an individual with such boundless curiosity. Seriously, I doubt that I will ever find someone else who would use a sick day to read scientific literature about the nasal cycle.[1] Over the years together, Prof. Ma has guided me in becoming a better scientist and shown by example that over every hurdle is a reason to keep running. For all these things and so much more, I am deeply grateful.

I would also like to thank my committee members for their time and guidance along the way, including Prof. Jon Ihlefeld, Prof. James Fitz-Gerald, Prof. Joseph Poon, and Prof. Saniya LeBlanc. Your continued attention and advice have helped to shape this dissertation into a product that I can be proud to see cap off my Ph.D. experience. I would also like to thank all the professors in our Materials Science and Engineering department who have either aided my path in the classroom or helped to form the culture of collective progress that our department embodies. In particular, I need to thank my undergraduate advisors: Prof. Jerrold Floro and Prof. James Fitz-

---

[1] I almost cited the paper in this acknowledgement section, but I'll let Prof. Ma tell you more about it.

Gerald (double shout-out). You both took a chance on a 19-year-old to step into a laser-filled, academic lab and just look at me now, still working with lasers and still with two functioning eyes and ten whole fingers. Talk about beating the odds. I can genuinely say that I would not be where I am today without the care, trust, and direction that both of you provided all those years ago. I also need to thank Jonathan Skelton, who truly took on the greatest burden during my fledgling years in research as my Graduate Student Mentor. Jonathan not only gave me the tools to succeed in research, but his endless patience and genuine friendship also showed me what it means to be a steadfast leader and an inquisitive world citizen. Endless thanks to the NMCF staff who provided the necessary training and technical support to conduct the characterization methods vital to this work. Thanks also to the MSE administrative staff for putting up with all my emails and questions.

To those who had a direct hand in collaborating on the critical works of this dissertation, I would also like to thank: Dr. Saniya LeBlanc, Dr. Vijayabarathi Ponnambalam, Dr. Joshua Martin, Dr. Dylan Kirsch, Dr. Prasanna Balachandran, and Roberto Herrera del Valle. Our numerous meetings and cooperation showed me at an early stage just how much there was to learn and appreciate in the worlds of thermoelectrics and machine learning. Many thanks also to all my past and present labmates: Dr. Wenhao Lin, Prosenjit Biswas, Fanyue Kong, Minh Tran, Rachel McNamara, Mrinaal Lorengo, Abayomi Akinwande, and all the undergraduate students who got to peek behind the curtain at graduate school life, especially Spencer Barnes who played a significant role in the survival of my sanity during the bulk porosity measurement process.

Of course, I can’t forget to thank my incredible family and especially my parents, Karl and Michelle, who constantly and unquestioningly lent me their support in whatever form I needed it. Whether it was a home-cooked meal or a random phone call, they never let me forget who was in my corner no matter what. Out of principle, I will also thank my little brother, Matthew, who has always been there when I needed a laugh and to remind me that medical school is much, much harder. I would also like to thank and acknowledge John, Claudia, Jack, and Libbie Ryan for all their warmth and advice. I consider myself unbelievably lucky to have not only been born with an amazing family but to have also been gifted a second one later in life.

Most importantly, I could not have done any of this without my best friend, my editor, and my wonderful wife, Caroline Headley, who picked up her life and moved with me to a new city in a hurricane during a global pandemic so that I could take the next step in my academic path. As daunting as any of those obstacles should have been, you wouldn't have known it watching her. We have been a team for almost eight years now and everything I have done since would not have been possible without her rocksteady presence at my side. Thank you for everything, Caroline, and I can't wait for the next step in our journey together.

There are so many others who I wish that I had the word count to thank as fully as they deserve, but I will simply say that your unwavering support has laid the foundation upon which any present or future success I may achieve is built. To all my friends in Charlottesville and beyond, thank you for the roles you have played in helping me reach this place in my life. I will always work to ensure that you feel the same level of kindness and encouragement in return.

Table of Contents

List of Figures

List of Tables

List of Terms and Symbols

TE: Thermoelectric

AM: Additive manufacturing

LPBF: Laser powder bed fusion

ZT: Thermoelectric figure of merit (dimensionless)

σ: Electrical conductivity [S/cm]

e: Elementary charge (1.602 x 10^{-19} C)

n: Electron charge carrier concentration [cm^{-3}]

p: Hole charge carrier concentration [cm^{-3}]

μ: Charge carrier mobility [cm^2/(V*s)]

κ: Thermal conductivity [W/(m*K)]

κ_L: Lattice component of the thermal conductivity [W/(m*K)]

κ_E: Electronic component of the thermal conductivity [W/(m*K)]

S: Seebeck coefficient [µV/K]

T: Temperature [K]

TEG: Thermoelectric generator

TEC: Thermoelectric cooler

V_2VI_3 Materials: V = Group V elements Sb and Bi; VI = Group VI elements S, Se, and Te

n-type: Electrons are the dominant charge carrier

p-type: Holes are the dominant charge carrier

VED: Volume energy density

p: Laser power [W]

v: Laser scan speed [mm/s]

h: Hatch spacing [µm]

t: Layer thickness [µm]

IED: Input energy density

SLM: Selective laser melting

ML: Machine learning

SS: Stainless steel

UHP: Ultra high purity

XRD: X-ray diffraction
TEM: Transmission electron microscopy
SEM: Scanning electron microscopy
SE: Secondary electron
BSE: Backscattered electron
SVR: Support vector regression
LOOCV: Leave-one-out cross-validation
Type A uncertainty: *aleatoric* or statistical
Type B uncertainty: *epistemic* or systematic
Bi'_{Te}: Cationic antisite defect
$Te^{\cdot}_{Bi}$: Anionic antisite defect
V'''_{Bi}: Cationic bismuth vacancy
$V^{\cdot\cdot}_{Te}$: Anionic tellurium vacancy
n*: equilibrium point defect concentration
N: total number of crystal lattice sites
E_d: Defect formation energy
k_B: Boltzmann constant (1.38 x 10^{-23} J/K)
SPS: Spark plasma sintered
PAS: Positron annihilation spectroscopy
PALS: Positron annihilation lifetime spectroscopy
DBS: Doppler broadening spectroscopy
τ: Phonon lifetime [ps]
τ^{-1}: Phonon scattering time
ω: Frequency
TD-NMA: Time-domain normal-mode analysis
FFT: Fast Fourier transform
at%: Atomic percentage
d: Thermal diffusivity [cm^2/s]
D: Density [g/cm^3]
C_p: Specific heat [J/(g*K)]
V_{th}: Thermoelectric voltage

dE: Electromotive force

ΔT: Temperature gradient

I: Current

V: Voltage

L: Length

A: Cross-sectional area

LFA: Laser flash analysis

DSC: Differential scanning calorimetry

XRF: X-ray fluorescence

μXRF: Micro X-ray fluorescence

EDS: Energy-dispersive X-ray spectroscopy

WDS: Wavelength dispersive spectroscopy

LAGB: Low angle grain boundary

HAGB: High angle grain boundary

EBSD: Electron backscatter diffraction

B: Magnetic field

R_H: Hall resistance

h: Sample thickness

k: Standard deviation

RT: Room temperature

TD: Temperature-dependent

m^*: Transport effective mass

L: Lorenz number

F: Kearns texture factor

G: Temperature gradient [K/m]

S: Liquid/solid interface velocity [m/s]

PF: Pole figure

IPF: Inverse pole figure

E_{AS}: Antisite defect formation energy

E_V: Vacancy formation energy

χ: Electronegativity

r: Covalent radius

EPMA: Electron probe microanalyzation

NIST: National Institute of Standards and Technology

PDF: Pair distribution function

PEEM: Photoemission electron microscopy

Chapter 1. Introduction

1.1 Motivation

A clear and present danger exists in our excessive and inefficient use of non-renewable fossil fuels. Rapid global industrialization has yielded an ever-increasing demand for electricity, which has so far been met through a commensurate rise in the burning of fossil fuels and emission of greenhouse gases [1]. Transport vehicle fuel inefficiency is often cited as a major example, where the energy equivalent of 46 billion gallons of gasoline are wasted each year through the exhaust pipes of roughly 200 million light-duty cars in the United States of America [2]. Globally, about two-thirds of produced energy is lost as unutilized heat into the atmosphere [3,4]. Therefore, the need to improve localized cooling technologies [5] and recapture wasted heat energy in the form of usable electricity has both economic and environmental advantages. Thermoelectric (TE) materials have garnered interest over the past several decades as a potential solution to this crisis due to their ability to convert between heat and electrical energy directly and reversibly and offer a unique opportunity to reduce industrial and automobile heat waste [1–3,6]. However, their widespread adoption has been hindered by their low conversion efficiency (≈5 %) and high production cost [7–9].

Further, a notable gap has been identified in the field of additive manufacturing (AM). AM techniques have emerged in the past several decades as novel processes for creating materials with unique geometries and properties via layer-by-layer construction. In this time, numerous studies have been conducted on the impact that AM techniques and process parameter manipulation can have on the physical, mechanical properties of a material [10]. These have included studies involving hardness [11–13], ultimate tensile strength [14–19], and fracture toughness [15,20,21]. However, not as much work has been focused on the potential ability of AM to influence the efficiency and directionality of a material's functional properties, such as piezoelectricity, magnetoelasticity, and thermoelectricity. By learning more about the mechanisms through which AM can alter the structure and performance of functional materials, one can utilize this understanding to build new materials with enhanced and intentional properties for practical applications.

Therefore, the goals and motivations of this dissertation not only have significance in the fields of energy harvesting and TE materials, but will also contribute to the still rapidly expanding pool of knowledge in the realm of AM.

1.2 Background

1.2.1 Thermoelectric (TE) Materials

When a temperature gradient is applied across a TE material, the more energetic charge carriers on the hot side will diffuse to the cold side, generating a proportional voltage. This phenomenon is known as the Seebeck effect, one of three thermoelectric effects [7,22]. The conversion efficiency of a TE material can be qualitatively evaluated by the dimensionless figure of merit (ZT):

$$ZT = \frac{\sigma S^2}{\kappa} T,$$

where σ is the electrical conductivity, S is the Seebeck coefficient, κ is the combined lattice (κ_L) and electronic (κ_E) thermal conductivities, and T is the temperature [7,22,23]. TE materials are most often assembled into devices known as TE modules, which are composed of many TE unicouples arranged thermally in parallel and electrically in series. Each TE unicouple consists of a grouped pair of n-type and p-type units called TE legs, as shown in **Figure 1-1**. These modules are not only capable of using the Seebeck effect to reversibly convert between thermal and electrical energy, but they also have the advantages of being noise-free, pollution-free, and solid-state with no moving parts [1,24].

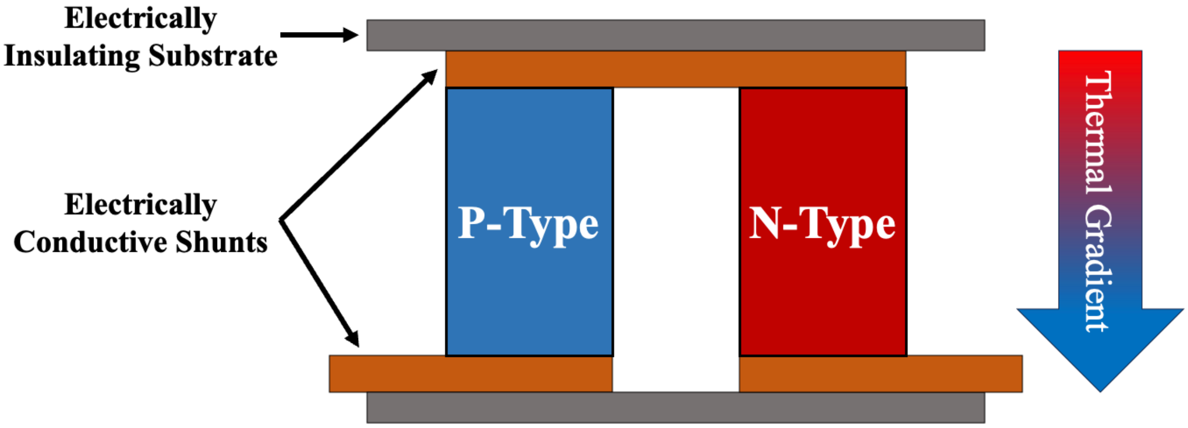

Figure 1-1. *Schematic of a typical thermoelectric unicouple (not to scale).*

However, current TE generators (TEGs) and TE coolers (TECs) are predominantly used sparingly and in niche refrigeration and power generation markets, such as radioisotope TEGs in spacecrafts created by NASA [23]. This is largely attributed to two main factors: low energy conversion efficiency and high production cost [7,23,24].

The charge carriers involved in these TE materials are either negatively charged electrons or positively charged holes. The most common and efficient TE materials are often semiconductors that have been doped with either electron donors or acceptors to promote a majority of one charge carrier type [25]. When the majority charge carriers in a material are negatively charged electrons, that material is said to be n-type. In contrast, a material is said to be p-type when the majority charge carriers are positively charged holes. When the concentration of one charge carrier is dominant, then the electric field will be stronger and more established in a single direction in response to the Seebeck effect.

V_2VI_3 compounds (V = trivalent Group V elements Sb and Bi; VI = Group VI chalcogen elements S, Se, and Te) have been the cornerstone TE materials, finding roles in both research and industrial settings due to their high TE figure of merit (*ZT*) at room temperature (RT) [26,27]. Bismuth telluride (Bi_2Te_3) is the most commonly used V_2VI_3 compound; however, it is frequently doped with another cationic Group V or anionic Group VI element to enhance the strength of its p-type or n-type character, respectively [27]. While a range of *ZT* values have been achieved and reported in literature, peak *ZT* values for traditionally manufactured, commercially available V_2VI_3 TE parts are typically reported at values of ≈1 [28].

The typical manufacturing process for TE devices is a lengthy, arduous procedure that limits the available TE leg geometries to simple shapes. Traditionally, the constituent elemental materials are mechanically alloyed into a starting powder. Then, conventional sintering techniques (*e.g.*, hot pressing or spark plasma sintering) are employed to consolidate the alloyed powders into ingots, which are then diced to produce the TE legs (**Figure 1-1**). However, this dicing process accounts for about 50 % of the material losses due to chipping, cracking, and kerf losses [29,30]. Additionally, it often constrains the possible TE leg geometries to rectangular prisms and cubes. The resulting TE legs are ultimately integrated for TE module assembly through costly and time-consuming pick-and-place operations [7].

1.2.2 Laser Powder Bed Fusion (LPBF)

Laser powder bed fusion (LPBF) is an additive manufacturing (AM) technique with the ability to create free form geometries and potentially reduce cost through the minimization of material waste and manufacturing steps [7]. LPBF is a non-equilibrium process that features rapid heating and cooling by using a laser beam to selectively and successively melt thin layers of powder particles in desired two-dimensional patterns [7,31–33]. This layer-by-layer construction can be utilized to produce fully dense, three-dimensional parts in complex geometries that are difficult to achieve through conventional manufacturing methods [24]. The primary input build parameters for the LPBF process involve the laser beam and are summarized in the volume energy density (VED) [J/cm^3] equation: $VED = \frac{p}{vht}$, where p is the laser power [W], v is the laser scan speed [mm/s], h is the hatch spacing [µm], and t is the layer thickness [µm] [24]. The hatch spacing refers to the distance between adjacent line scans. These LPBF processing parameters are shown in a representative diagram in **Figure 1-2**.

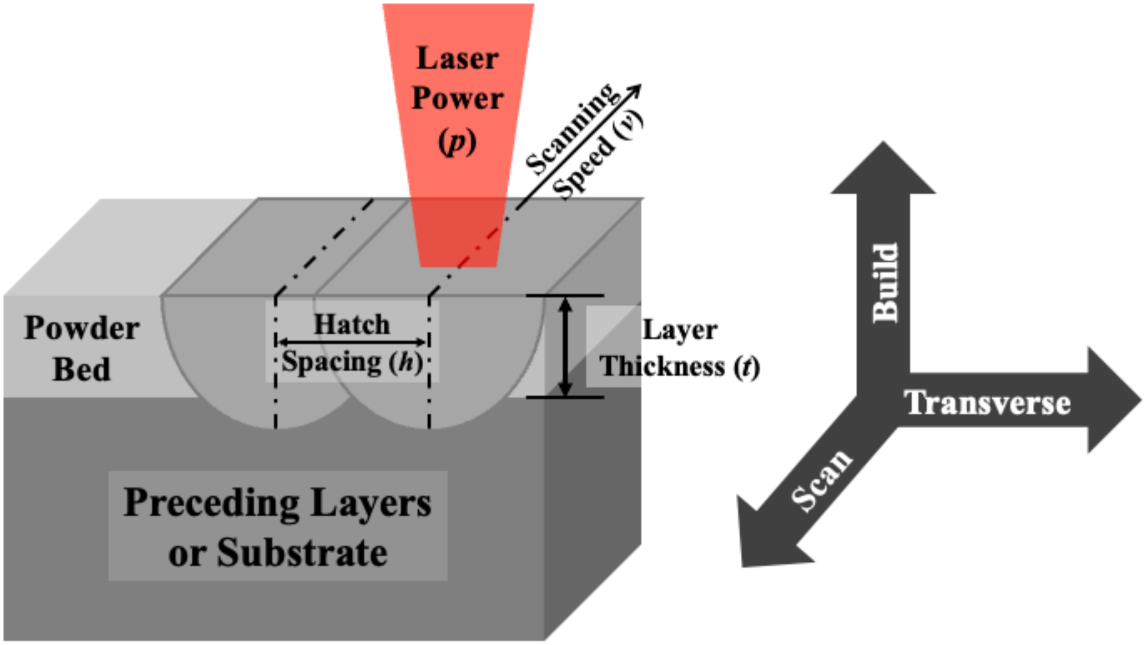

Figure 1-2. *LPBF process parameters: laser power (p), scanning speed (v), layer thickness (t), and hatch spacing (h). The scan, transverse, and build directions are also shown.*

Further, the ability to manipulate these laser process parameters during part fabrication provides a unique opportunity to construct materials with intentional, altered material properties. This can even be utilized to achieve spatially variant properties by altering the process parameters throughout a single build. This capability has been previously demonstrated through both laser and electron beam-based AM techniques, where process parameter adjustments were used to deliberately alter the temperature gradients and cooling rates to produce a variety of predictable microstructures [34–37]. The rapid solidification associated with LPBF has been previously shown to enhance the material performance of stainless steel 316L through hierarchical microstructure alterations to simultaneously achieve higher strength and ductility [38–40]. However, similar comparisons between LPBF-produced microstructures and resulting functional properties have not yet been as thoroughly investigated.

For many LPBF parts, there are three significant sample directions: scan, transverse, and build (see **Figure 1-2**). The scan direction aligns with the laser scan vector and is especially relevant for builds with unidirectional laser scan strategies. The build direction refers to the direction normal to the surface of the substrate and is the direction of the layer-by-layer construction. Finally, the transverse direction is perpendicular to both the build and scan directions (orthogonal to the build-scan plane).

The specific LPBF system employed in this work is a SLM®125 from SLM Solutions Group AG (Lübeck, Germany). It utilizes a single fiber laser from IPG Photonics (Oxford, Massachusetts) with adjustable power (0 W to 400 W) and scan speed (0 m/s to 10 m/s). The wavelength of the laser is 1070 nm, and the spot size is 60 μm. The chamber is kept under an inert argon environment during all builds, with the oxygen content held to less than 1,000 ppm.

1.3 Overview of Work

The goal of this work is to develop processes and investigate mechanisms that will allow for the intentional manipulation of TE properties using LPBF. To achieve this goal, a thorough study of the process-structure-properties relationships for LPBF-built bismuth telluride parts has been undertaken. Namely, this work sets out to investigate the ways in which LPBF processing parameters and post-processing techniques can affect a material's structure and properties to yield the resulting TE behavior. The reality is that TE properties are complex in their interrelationships, and it is often the case that the enhancement of one can be to the detriment of another. Therefore, this throughline understanding is best addressed using a broad consideration spanning multiple length-scales: bulk, micro, and atomic. A diagram demonstrating this hierarchical approach is provided in **Figure 1-3**.

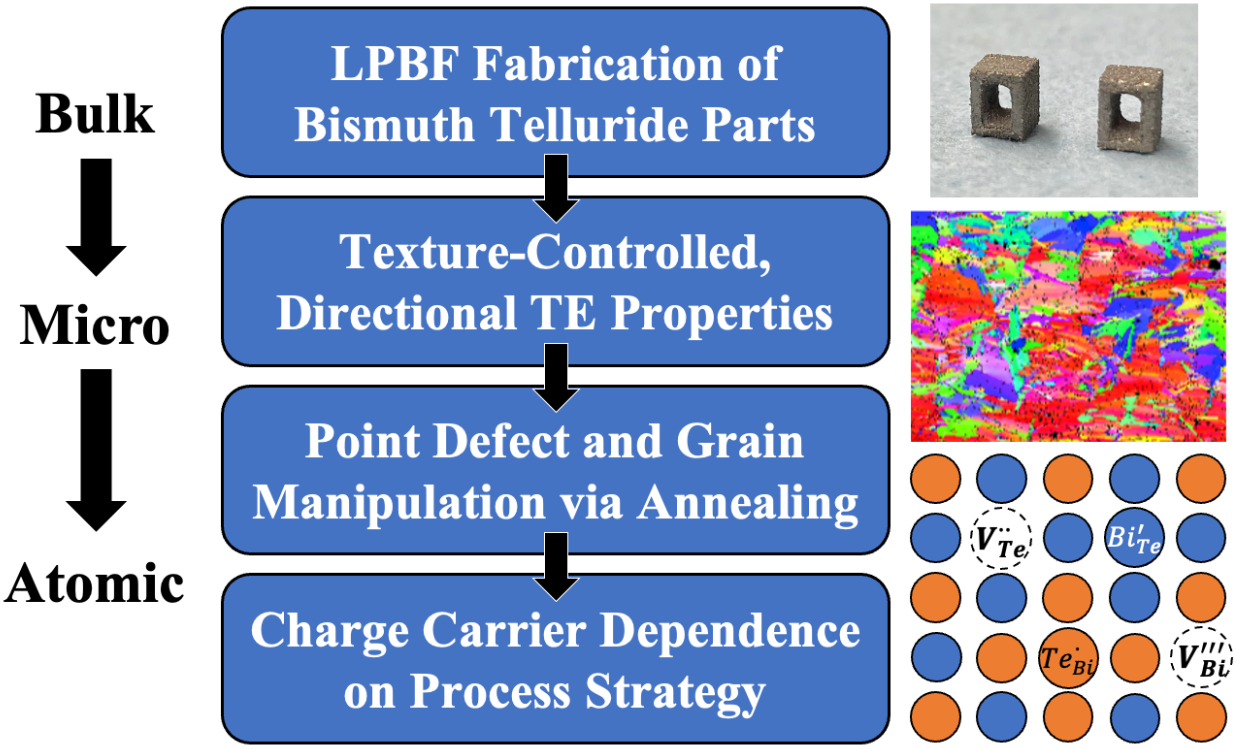

Figure 1-3. *Diagram illustrating the hierarchical approach taken to influencing TE properties across multiple length-scales (bulk, micro, and atomic) through LPBF in this work.*

The original major undertaking of this dissertation was to accomplish and demonstrate the LPBF fabrication of highly dense, crack-free bismuth telluride parts. Consequently, a process was created and discussed that featured an iterative system of experimental validation and augmented machine learning (ML) allowing for the rapid identification of optimal LPBF processing parameters. This initial work was also driven by two primary motivations. First, prior modeling predictions had emphasized the potential benefit of nonstandard TE leg geometries to improve the

TE efficiency at the bulk scale [25,41]. Ultimately, the fabrication of $Bi_2Te_{2.7}Se_{0.3}$ parts in these enhanced geometries was achieved and an example is shown in **Figure 1-3**. Second, the successful construction of high quality, three-dimensional bismuth telluride parts was a critical requirement for the subsequent studies into LPBF's ability to alter TE properties through material changes at finer length-scales. Simply, if LPBF could not build bismuth telluride materials, then there was no reason or ability for further study on the LPBF-controlled alteration of their TE properties.

The next step of this work involved the implementation of a post-processing heat treatment to study its impact on the material properties and corresponding TE behaviors of LPBF-built $Bi_2Te_{2.5}Se_{0.5}$ samples. Experimentally, it was demonstrated that a 350 ºC anneal for 24 hours could effectively improve the TE properties and efficiency of as-built LPBF parts. Mechanisms were proposed involving microstructural and atomic level material adjustments that could be connected to the maximum bulk ZT of 0.43 achieved at room temperature. Specifically, a beneficial reduction in the thermal conductivity was attributed to annealing-induced changes in dislocation density at low angle grain boundaries (LAGBs). Simultaneously, an advantageous increase in the electrical conductivity was ascribed to an observed reduction in the intrinsic point defect and charge carrier concentrations after annealing.

Additional work focused on the potential ability of LPBF to generate predictable crystallographic orientations in bismuth telluride parts to take advantage of the natural TE property anisotropy found in V_2VI_3 compounds. It is shown that the LPBF process is capable of controlling grain growth in polycrystalline, $Bi_2Te_{2.5}Se_{0.5}$ samples to produce strong crystallographic textures and anisotropic transport properties that agree with established literature for traditionally manufactured bismuth telluride compounds. In the end, this crystallographic orientation control can be leveraged to intentionally manufacture LPBF-built, $Bi_2Te_{2.5}Se_{0.5}$ parts with enhanced transport properties in specific sample directions. The impact of annealing on these directionally dependent TE properties was also explored.

Finally, a unique phenomenon was observed where LPBF processing parameter manipulation could be used to purposefully control the dominant charge carrier type (n-type to p-type) and concentration of $Bi_2Te_{2.7}Se_{0.3}$ samples. This was demonstrated both experimentally and through ML predictions via changes in the Seebeck coefficient (S) sign and magnitude across the processing parameter space. The roles of bulk porosity formation, oxide inclusion development, and matrix compositional changes were considered as possible explanations for this behavior.

Over the course of this dissertation, a hierarchical methodology is applied to investigate and unify the impact of LPBF on material properties across a wide range of length scales, including crystallographic orientations, dislocation manipulation, and point defect concentrations. Further, posited mechanisms are discussed to connect these LPBF-controlled material properties to the final, bulk TE behaviors. Ultimately, it is the hope that in the successful argumentation of these results and conclusions, it will be convincingly shown that LPBF is a viable manufacturing process for the intentional alteration and enhancement of TE properties through a multi-scale approach in bismuth telluride alloys.

Chapter 2. LPBF Fabrication of High-Quality, Bismuth Telluride Parts via an Augmented Machine Learning Approach

2.1 Introduction

2.1.1 Motivation

LPBF has emerged as a promising new approach to creating better TE devices [42]. Prior modeling work has shown that TE legs with more complex geometries and non-uniform cross-sectional areas result in larger thermal gradients and higher power generation potential than standard rectangular prism legs [7,25,41]. This would increase the effective, system-level *ZT* and conversion efficiency of the TE parts. **Figure 2-1** shows simulation results that demonstrate the predicted impact of hollow and trapezoidal geometries on thermal resistance when compared to a more traditional, rectangular prism TE leg. Unfortunately, the limitations of traditional TE manufacturing techniques restrict the possible geometries of TE legs to simple cuboids and cylinders. In contrast, LPBF techniques can theoretically allow for the fabrication of more complex geometries, such as those shown **Figure 2-1**.

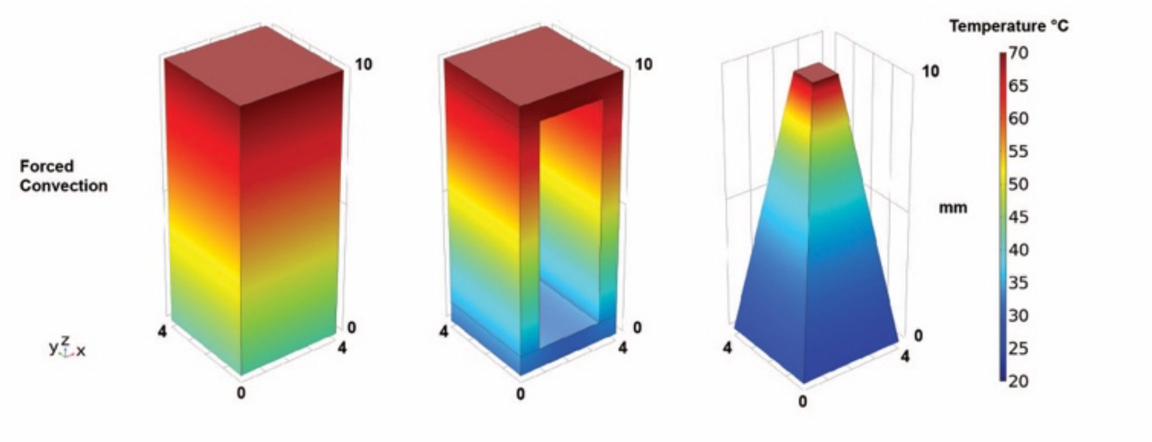

Figure 2-1. *Simulation results demonstrating the difference in the thermal gradient developed across three bismuth telluride geometries (from left to right): rectangular prism, hollow rectangle, and trapezoid. The simulations were performed with thermal boundary conditions of 70 ºC on the hot side and forced convective cooling with a convection coefficient of h = 200 W/m^{2}K on the cold side* [41].

2.1.2 Prior Efforts

The successful construction of crack-free and highly dense bismuth telluride parts through LPBF is challenging. This is due to the fact that bismuth telluride is a brittle and often difficult to process material with no room temperature ductility [43]. Even still, multiple groups have previously worked on the AM of TE parts to take advantage of the predicted benefits of nonstandard geometries [22,24,44]. In 2018, Zhang *et al*. [31] demonstrated the first successful LPBF of three-dimensional bismuth telluride (Bi_2Te_3) parts with TE properties comparable to those created through traditional manufacturing methods. However, a lack of optimized build parameters produced a low final part relative density of 88 %. Consequently, these parts were only constructed in simple cylinders and bars like those already being built using traditional manufacturing methods.

2.1.3 Augmented Machine Learning Approach

It is believed that high densities in LPBF-built bismuth telluride parts can be achieved through process optimization. In doing so, the successful construction of bismuth telluride parts in more complex geometries can be achieved. Traditionally, AM process optimization for a new material requires extensive and time-consuming experimentation. A complementary approach using machine learning (ML) could potentially accelerate the understanding of the entire material processing space using fewer experiments and fewer data points. More specifically, the proposed benefit lies in augmenting human intuition with predictions (along with the associated uncertainties) from ML models such that the human-ML interaction will lead to efficient navigation of the LPBF processing space. This is especially important in problems where one seeks to adopt LPBF-based techniques to rapidly optimize high quality parts of a novel material whose thermophysical properties (*e.g.*, latent heat of phase transformations, temperature-dependent thermal conductivity, specific heat capacity, density, etc.) are not known or well-studied. Lack of thermophysical data precludes the use of numerical models to inform the experimental approach.

Prior works have demonstrated the successful implementation of iterative Bayesian optimization and active (or adaptive) learning methods to AM systems. A vast majority of the effort has relied on constructing surrogate models to mimic the predictions of either simple (*e.g.*, Eagar-Tsai model) and/or complex numerical models (*e.g.*, finite element analysis) [45–48]. Subsequently, these surrogate models have guided the AM process space exploration. However, there are very few efforts dedicated to the construction of surrogate models for AM experiments (without the intermediate physical models). For example, Ye *et al*. [49] employed Bayesian optimization to identify the optimal processing parameters to fabricate high-density NiTi samples using the LPBF process. The authors started with nine samples to train the ML model and added three more samples (one sample per iteration) in a sequential manner as guided by the Bayesian optimization algorithm. In another study, Kitano *et al*. [50] discussed the use of Bayesian optimization method to identify the optimal laser irradiation conditions of Hastealloy X. More recently, Agarwal *et al*. [51] demonstrated the promise of classification learning methods to identify key processing parameters and in-situ sensor features that will result in a high power factor for LPBF-processed Bi_2Te_3. Although this work is strictly not active learning, it demonstrates the growing interest in adopting data-driven ML methods to guide LPBF processing of complex materials.

In the present work, the principles borrowed from Bayesian optimization and active learning are leveraged to efficiently navigate the LPBF processing space. One of the key outcomes is the development of an understanding of the melt pool geometry trends (in terms of width and depth) as a function of laser power and scan speed. At the end of every ML training iteration, two maps are generated (both as functions of laser power and scan speed): 1) the ML predictions of melt pool width and depth and 2) the associated uncertainties in the ML predictions that collectively capture the total variation due to sampling, ML model bias, and inherent process uncertainties. These maps are consequently used as a guide to select the next set of LPBF conditions. It is important to note that the trained ML models do not recommend specific LPBF conditions, but instead augment the LPBF-based insights for ultimate decision making. As a result, the data-driven ML strategy is best described as augmented ML. The LPBF experimental efforts in turn use the knowledge gained from ML augmented single-track experiments to rapidly optimize LPBF process parameters capable of building highly dense, crack-free bismuth telluride parts in the nonstandard geometries that have been predicted to yield higher thermoelectric performance.

2.2 Material and Methods

2.2.1 Bismuth Telluride Powder Synthesis

Mechanical milling techniques were employed to synthesize n-type bismuth telluride ($Bi_2Te_{2.7}Se_{0.3}$) alloy powder in an inert argon atmosphere. Constituent elements Bi (> 4N purity, Alfa Aesar), Te (4N purity, Alfa Aesar), and Se (5N purity, Alfa Aesar) were weighed in appropriate quantities and loaded into a stainless steel (SS) vial. Several SS balls with diameters in the range of 10 mm to 12 mm were also added, and the vials were sealed in dry argon (99.999 % UHP). Depending on the quantity of starting materials, either high energy vibratory milling unit or planetary milling unit was employed. For smaller quantities (< 30 g), a SPEX 8000 Mixer/Mill high energy milling unit capable of vibrating at 1060 cycles/min. was employed.

For larger quantities (> 30 g), a Torrey Hills ND0.4L planetary milling unit capable of rotating in both directions at 10 Hz (600 rpm) was used.

Milling was interrupted periodically for powder X-ray diffraction (XRD) of the milled powder to be conducted to assess the quality of the phase formation. Milling continued until only the XRD peaks for $Bi_2Te_{2.7}Se_{0.3}$ were observed. Typically, 11 hrs. to 16 hrs. of milling were required to obtain $Bi_2Te_{2.7}Se_{0.3}$ alloy without any observable impurities from XRD. **Figure 2-2** shows the final XRD pattern collected for the planetary milled $Bi_2Te_{2.7}Se_{0.3}$ alloy powder with significant peaks indexed. **Figure 2-3** contains a scanning electron microscopy (SEM) micrograph of the same planetary milled $Bi_2Te_{2.7}Se_{0.3}$ alloy powder, which possessed a range of sizes and irregular shapes.

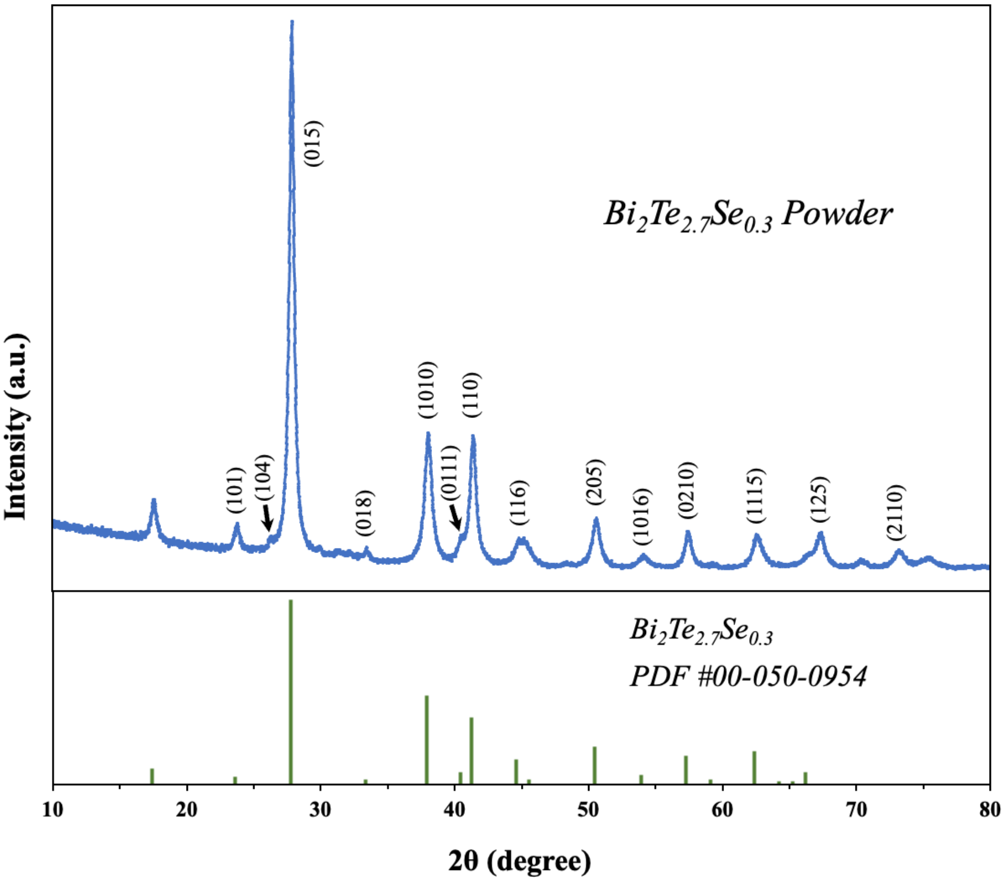

Figure 2-2. *XRD pattern of the planetary milled* $Bi_2Te_{2.7}Se_{0.3}$ *alloy powder. The pattern is well-matched in position and intensities to the database values for* $Bi_2Te_{2.7}Se_{0.3}$ *(PDF#00-050-0954).*

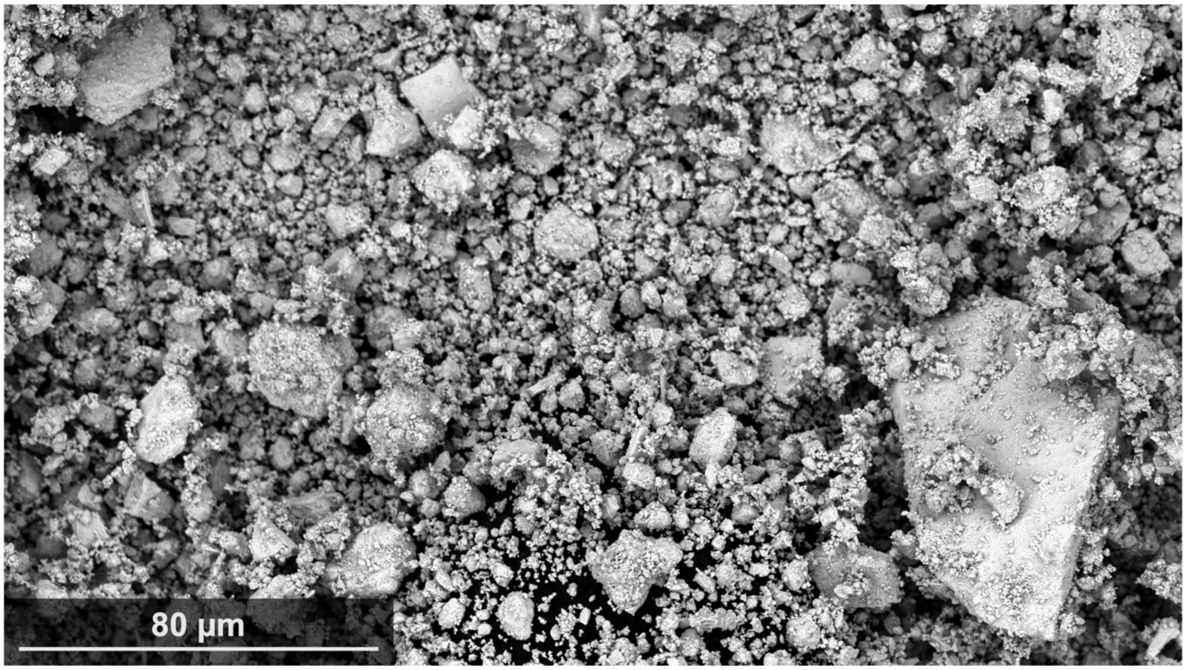

Figure 2-3. *Secondary electron (SE) micrograph of the planetary milled Bi2Te2.7Se0.3 alloy powder.*

For build substrates, p-type bismuth antimony telluride ingots were purchased from Tecteg Mfr. based in Ontario, Canada. These ingots were then sectioned using a diamond wafering blade into roughly 5mm thick discs that could be used as substrates for the LPBF process.

2.2.2 Line Scan Experiments

To study the laser interaction with n-type bismuth telluride, line scan experiments were used. These line scans were run in the SLM$^{®}$125 system and across bulk n-type BiTeSe wafers from Coherent, an example of which is shown in Figure 6a. Laser power (*p*) and scan speed (*v*) were adjusted as processing parameters for each line scan.

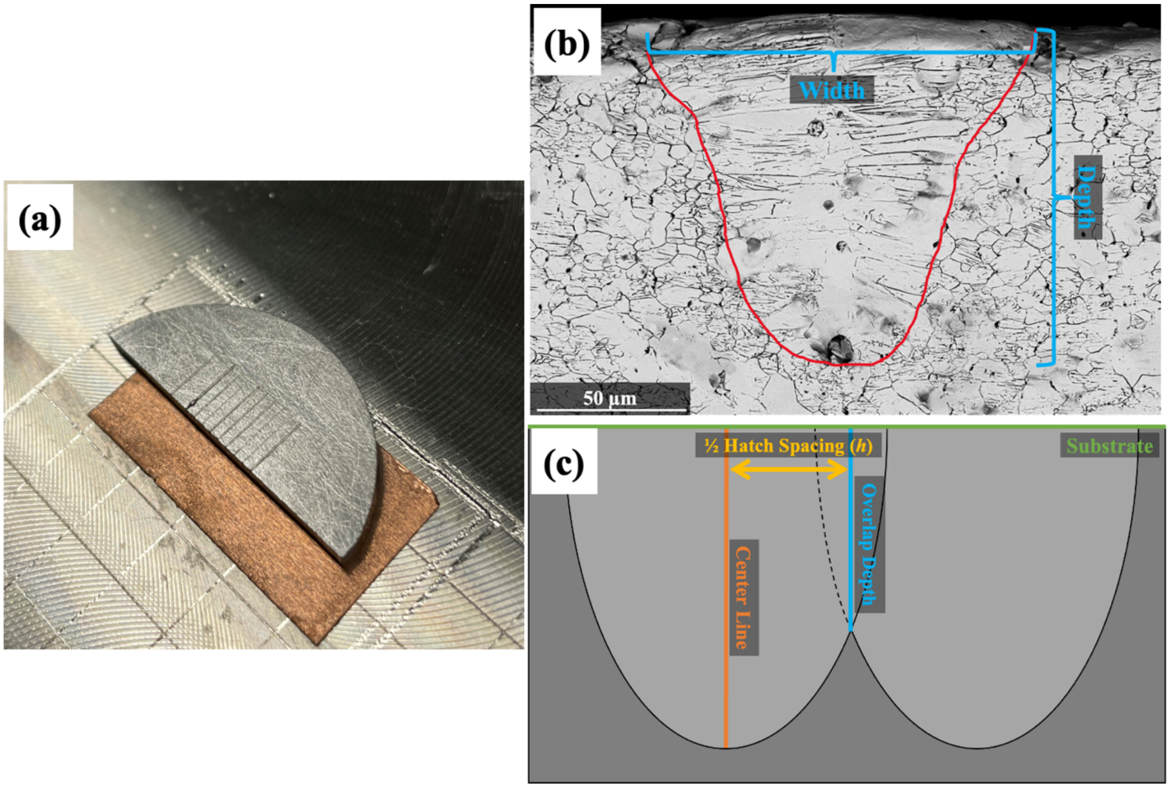

Figure 2-4. *(**a**) Multiple laser line scans run across a solid disc of n-type BiTeSe (diameter = 2 cm), shown adhered to the build plate using copper tape. (**b**) Backscattered electron micrograph of the cross-section (perpendicular to the laser scan direction) of a laser scan melt pool (p = 20 W, v = 350 mm/s) in n-type bismuth telluride that was etched for 15 seconds in aqua regia (3 HCl: 1* HNO_3*). The melt pool is outlined in red. (**c**) Diagram demonstrating how to calculate the hatch spacing from a melt pool cross-section perpendicular to the laser scan direction.*

To measure the widths and depths of these melt pools, the laser-scanned discs with diameters of 2 cm (as in **Figure 2-4a**) were polished to expose their cross-sections perpendicular to the laser scan direction. Then, these samples were etched in aqua regia (3 HCl: 1 HNO_3) for 15 seconds to visualize the line scan melt pools. An example is shown in **Figure 2-4b**. The melted region can be distinguished by the columnar grains bridging from the edges of the melt pools to their centers, in contrast to the equiaxed grains of the surrounding unmelted material. Melt pool width and depth measurements were made from electron micrographs using ImageJ. We estimate the uncertainty for these measurements to be ± 5 %. This process was repeated across three cross-sections for each sample, so that multiple measurements could be averaged for each line scan and laser parameter combination (laser power and scan speed) to account for fluctuations in melt pool size along a single laser scan track [52,53]. In total, 93 line scans were conducted and the laser parameters are provided in **Table 2-2** in the Appendix along with their average experimental melt pool widths and depths.

These line scan melt pool tracks were used to determine the other two key parameters necessary for building three-dimensional parts in LPBF: hatch spacing (h) and layer thickness (t). The values for these parameters were chosen to ensure sufficient fusion between the adjacent line scans and consecutive layers of powder during the build. For this reason, the layer thickness was chosen first and could be no deeper than half the melt pool depth.

The process for determining the appropriate hatch spacing value is demonstrated using **Figure 2-4c**. Adjacent line scans must overlap at a depth that is at least equivalent to the layer thickness. To account for the mild fluctuation in melt pool size along its track, an error of 25 % is assumed when deciding the overlap depth (*i.e.*, overlap depth = $1.25t$). This adjusted overlap depth is then found along the melt pool edges and a straight line is drawn up to the surface of the substrate. The distance between that overlap depth line and the center line of the melt pool is then measured and doubled to find the hatch spacing value. Another 20 % uncertainty is used when deciding the final hatch spacing value to account for the melt pool size fluctuations. This is a 20 % reduction in the measured hatch spacing value to bring the adjacent line scans closer together and increase their overlap (*i.e.*, h = 0.8 x measured hatch spacing).

2.2.3 Three-Dimensional Sample Fabrication and Porosity Measurements

Due to limitations in feedstock quantity and morphology, the LPBF builds were performed manually. The powder was deposited and leveled by hand in the argon-filled chamber of the SLM®125 system between each layer. Powder spreading was accomplished through a rolling metal rod, which simulates the action of the recoater blade. The rod was counter-rotated (against its natural rolling direction) to ensure that excess powder above the layer thickness was pushed off the substrate.

Rectangular bars of $Bi_2Te_{2.7}Se_{0.3}$ were built with dimensions of 1.5 mm x 6 mm x 0.525 mm using a scan strategy where the laser line scans are unidirectional and parallel to the long axis of the samples without rotation between layers. To quantitatively evaluate their relative densities, the volume of the pores was estimated from micrographs and images such as those shown in **Figure 2-5**. First, secondary electron micrographs were collected across multiple polished cross-sections perpendicular to the laser scans and long axis for each of the samples. Then, ImageJ was used to create a binary image that differentiated the pores from the polished surface based upon contrast. The porosity fraction was measured and averaged across three cross-sections for each sample.

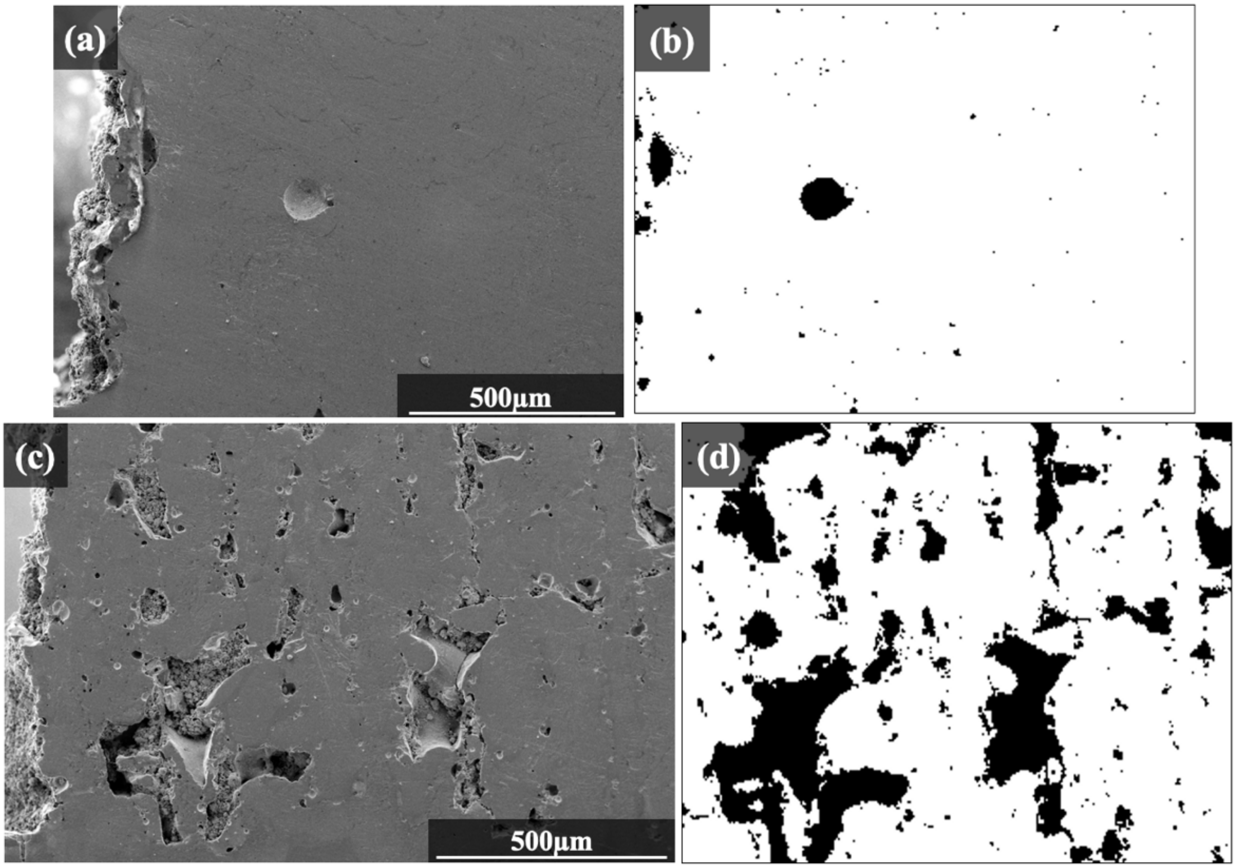

Figure 2-5. *Representative porosity calculations for LPBF-built $Bi_2Te_{2.7}Se_{0.3}$ parts demonstrating low porosity (**a** & **b**: p = 25 W, v = 100 mm/s, h = 90 µm, t = 75 µm) and high porosity (**c** & **d**: p = 25 W, v = 400 mm/s, h = 130 µm, t = 75 µm). (**a**, **c**) show the secondary electron micrographs and (**b**, **d**) show the binary images created through ImageJ that mark all pores in black.*

When building the enhanced, nonstandard geometry parts, the same manual build strategy was employed, with powder deposition and leveling being carried out by hand in between layers in the SLM$^{®}$125 build chamber. Additionally, the scan strategy was altered to minimize potential build defects. The line scan angles were rotated 33 degrees from layer to layer and were constrained to a 90 degree window centered around the shortest axis of the samples. This variation in direction and reduction in line scan vector length was used to reduce the buildup of thermal stress in the LPBF-built part [54,55].

2.2.4 Machine Learning (ML)

The goal of ML is to predict melt pool width and depth as a function of LPBF process parameters (laser power and scan speed). In addition, the trained models should be able to quantify uncertainties in the predicted values. We accomplished the task by building an ensemble of ML models (as opposed to a single ML model) using the bootstrap resampling method, which is a well-known sampling technique used to estimate statistics on a population by sampling the dataset with replacement (*i.e.*, the bootstrapped dataset can have multiple duplicate entries) [56]. For example, if we considered 50 bootstrap samples, then we trained 50 independent ML models. The mean value and standard deviation from the 50 trained models are then used as the predicted response and the associated uncertainty in the response, respectively. Hence the name ensemble ML, which is a well-established approach in the materials informatics literature [57–60].

Support vector regression (SVR) was employed as the ML method for ensemble model building [57,61]. In general, SVR is of the form,

$$f(\mathbf{x}) = \langle \mathbf{w}, \mathbf{x} \rangle + \mathbf{b},$$

where $\mathbf{x}$ is a vector of descriptors, $\mathbf{w}$ are coefficients that fit the training data, and $\mathbf{b}$ is the intercept. The objective function is then given as:

$$\min \frac{1}{2} \|\mathbf{w}\|^{2} + \mathbf{C} \sum_{\boldsymbol{i}=\mathbf{1}}^{\boldsymbol{n}} (\boldsymbol{\xi}_{\boldsymbol{i}} + \boldsymbol{\xi}_{\boldsymbol{i}}^{*})$$

$$\text{subject to} \begin{cases} f(\mathbf{x}) - \langle \mathbf{w}, \mathbf{x}_{\boldsymbol{i}} \rangle - \mathbf{b} \ \leq \in + \boldsymbol{\xi}_{\boldsymbol{i}} \\ \langle \mathbf{w}, \mathbf{x}_{\boldsymbol{i}} \rangle + \mathbf{b} - \boldsymbol{f}(\mathbf{x}) \ \leq \in + \boldsymbol{\xi}_{\boldsymbol{i}}^{*} \\ \boldsymbol{\xi}_{\boldsymbol{i}}, \boldsymbol{\xi}_{\boldsymbol{i}}^{*} \ \geq \mathbf{0} \end{cases},$$

where $\mathbf{C}$ is the regularization term, *n* is the total number of data points, ∈ is the insensitive tube around the target values that provides the magnitude of the amount of permitted error (only those target values greater than ∈ are penalized by the optimization), $\boldsymbol{\xi}_{\boldsymbol{i}}, \boldsymbol{\xi}_{\boldsymbol{i}}^{*}$ are the nonnegative slack variables that permit a certain level of violation of the ∈-tube bounds, and $\mathbf{x}_i$ is the descriptor for the i^{th} training data. The regularization term $\mathbf{C}$ balances the model complexity and training error (large $\mathbf{C}$ and small $\mathbf{C}$ can lead to overfitting and underfitting, respectively). In this work, we use the nonlinear Gaussian radial basis function of the form:

$$\boldsymbol{\kappa}(\mathbf{x}, \mathbf{x}') = exp\left(-\frac{\|\mathbf{x} - \mathbf{x}'\|^2}{2\boldsymbol{\sigma}^2}\right)$$

The hyperparameters, $\mathbf{C}$ and $\boldsymbol{\sigma}$ were determined by using leave-one-out cross-validation (LOOCV) from the training data to balance the bias–variance tradeoff. We chose four different values for the number of bootstrap samples: $\{25, 50, 75, 100\}$. The following values were explored for C = {0.001, 0.01, 0.1, 1, 2, 3, 4, 5, 6, 7, 8, 9, 10, 100} and σ = {0.001, 0.01, 0.1, 0.2, 0.3, 0.4, 0.5, 0.6, 0.7, 0.8, 0.9, 1.0}. For each bootstrap resample dataset, exhaustive grid search was used for hyperparameter optimization. Finally, the hyperparameters that minimize the LOOCV error are used for training the final model. The SVR method was utilized as implemented in the open source e1071 R-package for this work [62]. After model training, the mean and standard deviation were calculated from the ensemble of SVR models and served as the ML prediction of melt pool width (or depth) and the associated uncertainties, respectively.

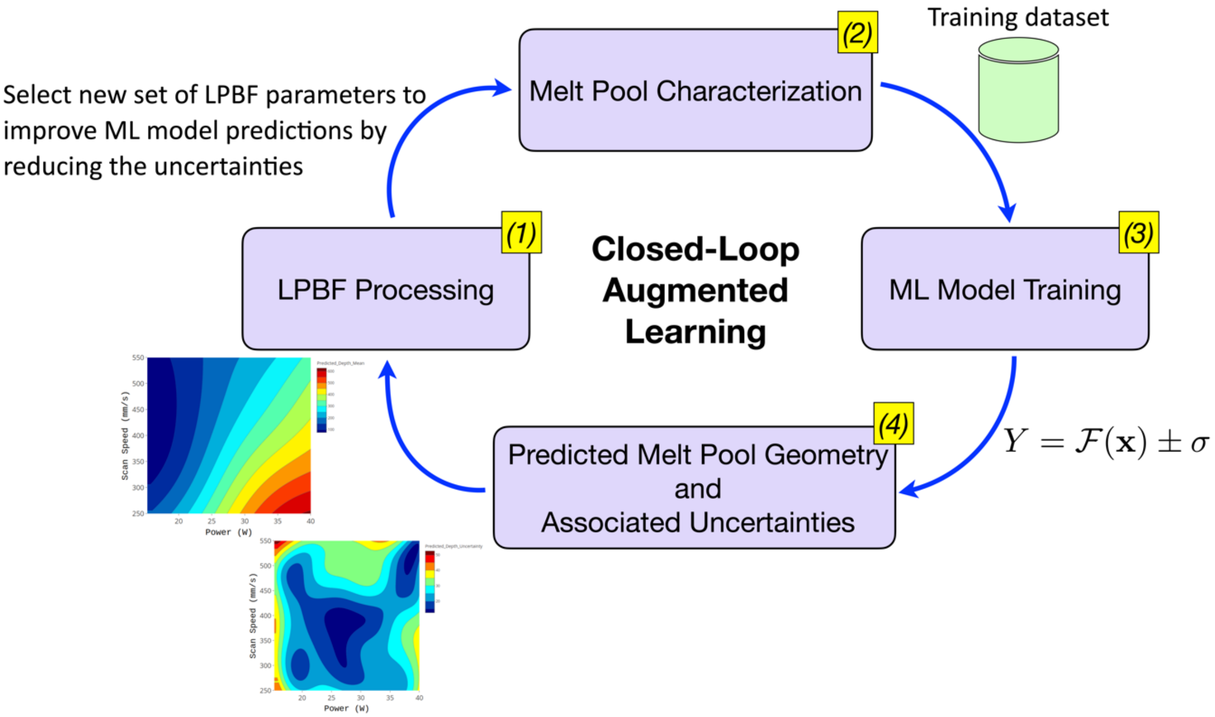

Figure 2-6. *A schematic showing the iterative augmented learning strategy used to develop a predictive understanding of the melt pool geometry (width and depth) using LPBF processing of n-type* $Bi_2Te_{2.7}Se_{0.3}$ *thermoelectric. A total of six iterations were performed with feedback.*

2.3 Results and Discussion: Laser-Material Interactions

2.3.1 Melt Pool Width and Depth Maps

The initial step of process optimization was an iterative combination of ML and experimental data that produced predictive models for the melt pool widths and depths within the build parameter space of interest. The iterative augmented learning strategy is schematically shown in **Figure 2-6**.

First, a small experimental dataset was generated to create an initial model using ML. Multiple laser lines were scanned across a solid substrate of n-type bismuth telluride, an example of which is shown in Fig. 6a. In total, 13 line scans were conducted with laser powers (*p*) ranging from 10 W to 40 W and laser scan speeds (*v*) ranging from 250 mm/s to 550 mm/s. These values spanned the initial parameter space of interest, which was chosen to expand around the parameter combinations that had previously been tested in similar works [22,24,31,44]. The melt pool widths and depths for these initial line scan parameter combination experiments were measured experimentally as in **Figure 2-4b** and can be found in **Table 2-1**.

Table 2-1. *Initial experimental and ML-predicted line scan data used to generate the predicted melting behavior maps from ML. We estimate the uncertainty for the experimentally measured dimensions to be ±5 % (1 sigma). Italicized parameter combinations were ultimately chosen to build three-dimensional, rectangular bar samples. These 13 line scan parameter combinations represent the first iteration of experimental data used to train the initial ML model. Ultimately, 93 line scan parameter combinations (**Table 2-2**) were used to generate the final ML predictive model for n-type bismuth telluride melt pool dimensions.*

Line Scan Parameters		**Experimental Dimensions**		**ML-Predicted Dimensions**		**ML Prediction Uncertainty**		**Relative Uncertainty**	
Power p (W)	**Scan Speed v (mm/s)**	**Width (μm)**	**Depth (μm)**	**Width (μm)**	**Depth (μm)**	**Width (μm)**	**Depth (μm)**	**Width**	**Depth**
10	300	No melting		No melting		No melting		No melting	
10	400	No melting		No melting		No melting		No melting	
10	550	No melting		No melting		No melting		No melting	
20	*350*	*125*	*117*	*128*	*130*	*13.5*	*20.7*	*0.105*	*0.159*
20	*450*	*110*	*86.5*	*118*	*104*	*12.0*	*19.3*	*0.101*	*0.186*
20	550	99.0	75.0	112	112	12.4	34.9	0.111	0.312
25	350	133	237	149	235	13.1	14.8	0.088	0.063
25	350	136	239	149	235	13.1	14.8	0.088	0.063
25	*400*	*135*	*207*	*150*	*201*	*9.08*	*13.4*	*0.061*	*0.067*
25	*400*	*128*	*215*	*150*	*201*	*9.08*	*13.4*	*0.061*	*0.067*
30	300	151	412	187	405	19.6	19.5	0.105	0.048
30	500	124	267	165	228	24.6	33.3	0.149	0.146
40	250	172	626	200	607	42.0	37.7	0.211	0.062

The absence of a melt pool indicated that no melting occurred for that line scan parameter combination. It was observed experimentally and predicted using ML that no melting occurs when the laser power is below 15 W. Therefore, the parameter space could be narrowed to exclude this nonmelting region going forward.

The ten experimentally measured melt pool dimensions were then used to create the initial model from ML, which was visualized using a heat map. An additional heat map was also created that showed the uncertainty of the model's predictions within the same parameter space. Subsequent line scan experiments were chosen that targeted parameter combinations in the regions with greater uncertainties. In total, 93 line scan parameter combinations were conducted and their melt pools measured across six iterations of closed-loop augmented learning with feedback. The full experimental line scan melt pool data is provided in **Table 2-2** in the Appendix. Ultimately, the final melt pool width and depth ML prediction maps were generated from these 93 data points and are shown in **Figure 2-7**. The associated uncertainty maps are also provided in **Figure 2-8**. The ML-predicted melt pool dimensions and associated uncertainties can be found in **Table 2-1** for the initial 13 line scan parameter combinations.

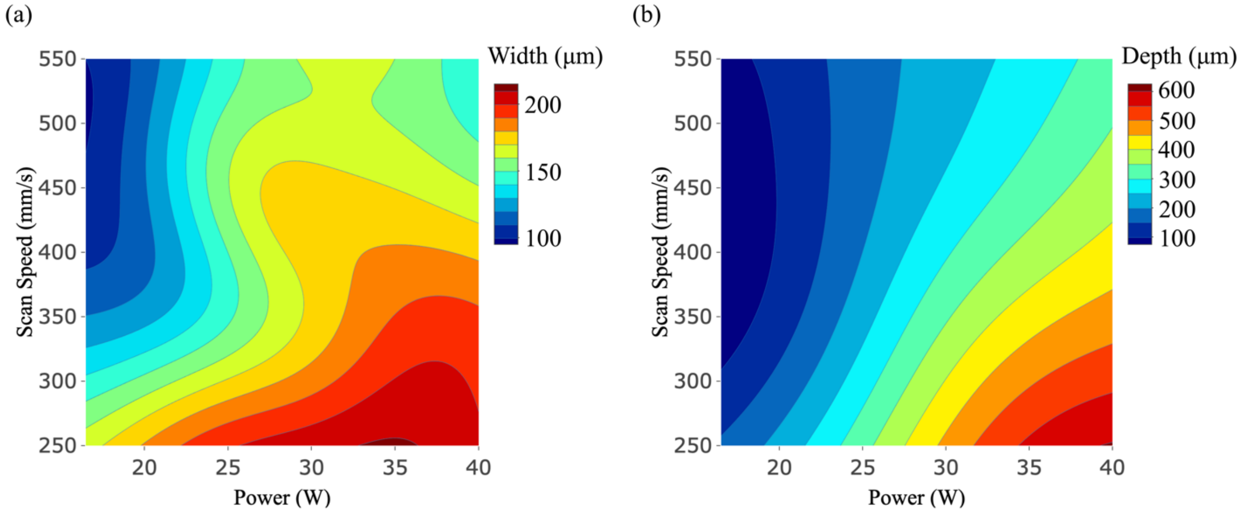

Figure 2-7. *ML-predicted melt pool (**a**) width and (**b**) depth maps for n-type bismuth telluride ($Bi_2Te_{2.7}Se_{0.3}$).*

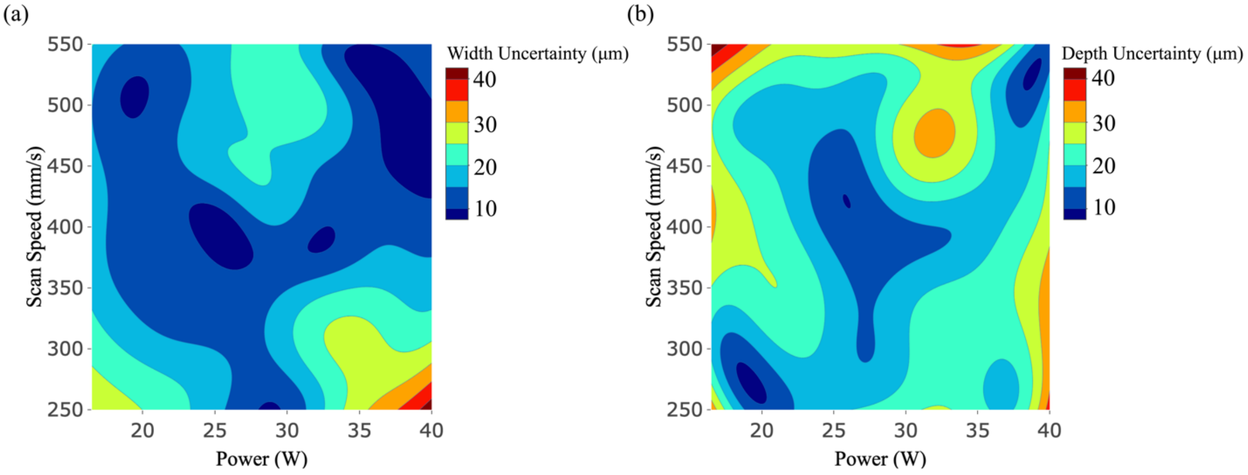

Figure 2-8. *Uncertainties in ML-predicted melt pool **(a)** width and **(b)** depth maps for n-type bismuth telluride ($Bi_2Te_{2.7}Se_{0.3}$).*

Several trends were observed from these melt pool dimension prediction maps. First, as the input energy density (IED) is increased by either increasing the laser power (*p*) or decreasing the laser scanning speed (*v*), the melt pool dimensions become larger. This matches expectations well for laser-based AM processes [63–66]. Additionally, for the melt pool depth prediction map shown in **Figure 2-7b**, the contour lines become shallower and more horizontal for higher IED processing parameters (high *p*, low *v*), so the laser scanning speed (*v*) has a greater impact on the melt pool depth in this region. In contrast, the slope increases and becomes more vertical in the lower IED processing region (low *p*, high *v*), which indicates the laser power (*p*) has a greater impact on the melt pool depth for these laser parameters.

For the melt pool width prediction map shown in **Figure 2-7a**, trends in the slope are less clear. However, as the laser power and scanning speed both increase (upper right corner), the growth in melt pool width diminishes until a region is reached where the change in melt pool width is less pronounced despite variations in the laser parameters. Once again, evidence of these stagnant melt pool widths at high laser powers and scanning speeds has been observed in literature [63,67]. The observation of these trends is valuable when attempting to tune the desired shape of the melt pool by preferentially adjusting the laser power or scan speed to intentionally manipulate the melt pool dimensions.

The uncertainty values shown in **Figure 2-8** have multiple contributing factors, including sampling, model, and experimental errors. It is common to classify uncertainties from ML into two types: Type A (*aleatoric* or statistical) and Type B (*epistemic* or systematic) [68,69]. While the Type A uncertainty can be reduced by sampling data points in the LPBF processing space where the ML model is ignorant, it is not straightforward to reduce the contribution from the aleatoric uncertainty. In this work, one of the key contributors to these uncertainties were experimental sample-to-sample variations.

The presence of defects (*e.g.*, pores, cracks) was also recorded for various laser parameter combinations. Pore frequency and volume tended to be greater for line scans run using higher IED values. This is consistent with well-established knowledge in LPBF: higher energy density line scans tend to cause keyholing and the formation of vapor depression zones that leave behind gas pores when solidified [63,70]. Cracking was not observed in the line scan melt pools.

2.4 AM of Three-Dimensional Builds

2.4.1 Determination of Build Parameters

Following single track laser scans and characterization of melt pool geometries, it is possible to use the predictive maps shown in **Figure 2-7** to determine the parameter combinations that could minimize defect concentration in three-dimensional parts of n-type bismuth telluride ($Bi_2Te_{2.7}Se_{0.3}$). For these bulk builds, the four process parameters that need to be defined are the laser power (p), scanning speed (v), layer thickness (t), and hatch spacing (h) (**Figure 1-2**).

Using the melt pool width and depth prediction maps (**Figure 2-7**), parameter combinations were chosen that yielded melt pools with a low uncertainty in melt pool geometries and a moderate depth to width ratio to minimize potential porosity. Larger uncertainties in the final ML predictions were assumed to be indicative of an increased inconsistency in the melt pool sizes. Relative uncertainty values, shown in **Table 2-1**, were calculated by dividing the ML prediction uncertainties in width or depth by their associated width or depth predicted values, respectively. A maximum relative uncertainty of 0.2 was established to ensure consistency between the laser scans of the LPBF build.

Within laser-based AM, when the melt pool depth to width ratio is large, keyhole porosity is often generated due to the instability of the vapor depression region [38,63]. A maximum depth to width ratio of 1.5 was established for this study. On the other hand, shallow melt pools can increase the risk for lack of fusion porosity due to incomplete melting. Optimized laser parameter combinations are chosen to generate melt pools between these two extremes and in a defect-free regime to build highly dense parts [71]. A diagram of a generic AM processing map containing these three processing regimes can be found in **Figure 2-9**. It is noted that at sufficiently high laser power and scan speed values, balling can occur beyond the defect-free processing regime and should also be avoided [72].

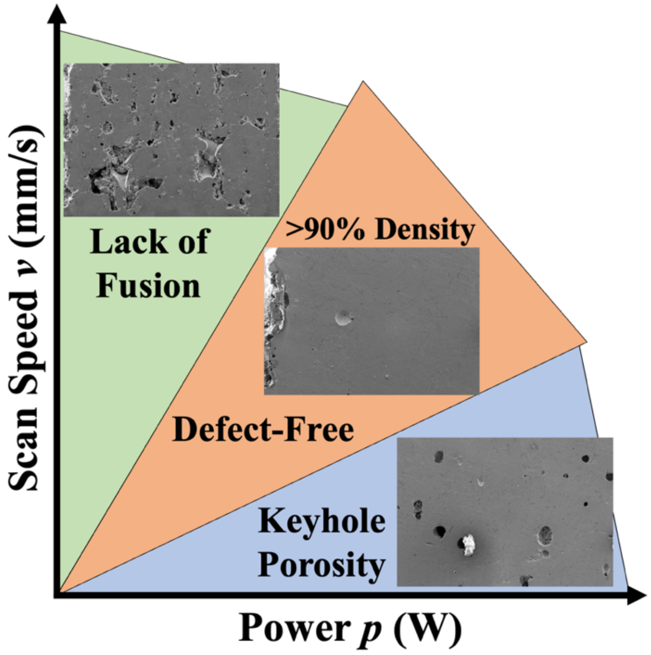

Figure 2-9. *General AM processing map that demonstrates the three distinct processing regimes: lack of fusion, defect-free, and keyholing mode zones.*

Following this process, the final build parameter combinations were determined: 1) $p = 20$ W, $v = 350$ mm/s, $h = 56$ µm; 2) $p = 25$ W, $v = 400$ mm/s, $h = 40$ µm; 3) $p = 20$ W, $v = 450$ mm/s, $h = 48$ µm; and 4) $p = 20$ W, $v = 350$ mm/s, $h = 70$ µm. A layer thickness (t) of 35 µm was used when building all four samples. Sample 4 uses the same laser parameters as sample 1, except with a larger hatch distance. These chosen laser parameter combinations and associated melt pool width and depth information are italicized in **Table 2-1**.

2.4.2 Sample Fabrication and Characterization

$Bi_2Te_{2.7}Se_{0.3}$ rectangular bars were then fabricated, and representative SEM micrographs of their cross-sections are shown in **Figure 2-10**. While a few cracks were observed in the substrate, no cracks were present in samples 1-3. In contrast, sample 4 did show signs of cracking, particularly near its top surface.

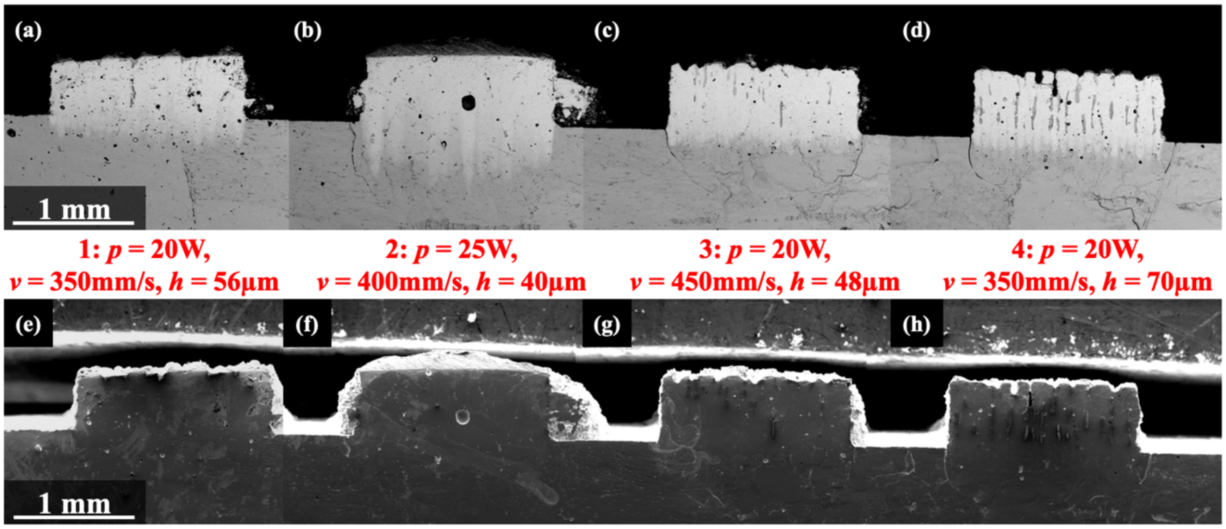

Figure 2-10. *Representative SEM micrographs of the cross-sections of LPBF-built $Bi_2Te_{2.7}Se_{0.3}$ parts. Backscattered electron micrographs shown on top (**a**, **b**, **c**, & **d**) and secondary electron micrographs shown on bottom (**e**, **f**, **g**, & **h**). Build parameter combinations used are: (1: **a** & **e**) p = 20 W, v = 350 mm/s, h = 56 µm; (2: **b** & **f**) p = 25 W, v = 400 mm/s, h = 40 µm; (3: **c** & **g**) p = 20 W, v = 450 mm/s, h = 48 µm; and (4: **d** & **h**) p = 20 W, v = 350 mm/s, h = 70 µm. A layer thickness (t) of 35 µm was used when building all four samples.*

Three cross-sectional images for each sample were used to measure the average sample porosities using the process shown in **Figure 2-5**. Ultimately, it was found that the average porosities (± standard deviation) of these samples were 1: 1.4 % (± 0.5 %), 2: 0.9 % (± 0.9 %), 3: 3.8 % (± 0.4 %), and 4: 8.2 % (± 1.3 %). To our knowledge, this is the lowest porosity and highest relative density that has been reported through the LPBF AM of bismuth telluride. Since bismuth telluride is a brittle and often difficult to process material with no room temperature ductility [43], successful fabrication of crack-free and highly dense samples demonstrates the ability of this newly developed protocol to find process parameters that can successfully build high quality parts out of a new AM material.

2.5 Fabrication of Enhanced Geometry Parts

2.5.1 Additively Manufactured Thermoelectric Parts with Nonstandard Geometries

In order to test the predictive capabilities of this augmented ML process, we utilized it to search for optimized parameters for a significantly larger layer thickness (*t*). The initial builds shown in **Figure 2-10** were conducted with a layer thickness of 35 μm, which is in the lower range of parameters commonly used by both researchers and industry. Building with larger layer thicknesses is typically preferable to reduce the total build time, but it is often challenging due to large melt pool size requirements and increased risk for lack of fusion or keyhole porosity. Here, we choose a layer thickness of $t = 75$ μm, which would reduce building time by more than 50 % when compared to a 35 μm layer thickness.

Based upon the results of bar sample 2 (**Figure 2-10**), the laser parameter combination of $p = 25$ W and $v = 400$ mm/s was selected for creating $Bi_2Te_{2.7}Se_{0.3}$ parts with enhanced, nonstandard geometries. This was because bar sample 2 was both entirely devoid of cracks and had a very low porosity fraction of 0.9 % (± 0.9 %). Additionally, ML predicted that the melt pool depth for $p = 25$ W and $v = 400$ mm/s was 201 μm (**Table 2-1**), which meant that this laser parameter combination would be an acceptable choice at over double the depth of this new layer thickness. Following the method discussed in *Section 2.2.2* and shown in **Figure 2-4c**, the new hatch spacing was calculated to be 80 μm. The final processing parameters were selected as: $p = 25$ W, $v = 400$ mm/s, $h = 80$ μm, and $t = 75$ μm.

The LPBF-built complex geometries were chosen based on the prior modeling work (shown in **Figure 2-1**) that predicted these geometries could increase the TE efficiency of $Bi_2Te_{2.7}Se_{0.3}$ parts [25,41]. These three geometries were the rectangular prism, hollow rectangle, and trapezoid. The rectangular prism was chosen as a control sample with dimensions of 4 mm x

4 mm x 10 mm, comparable to traditionally manufactured TE legs. The hollow rectangle also had outer dimensions of 4 mm x 4 mm x 10 mm, with a wall thickness of 0.75 mm. The trapezoid had a length of 10 mm, a 4 mm x 4 mm large base, and a 1 mm x 1 mm small face.

Using the new processing parameters and scan strategy, $Bi_2Te_{2.7}Se_{0.3}$ parts were successfully constructed in the rectangular prism, hollow rectangle, and trapezoid geometries (**Figure 2-11**). The parts show no visible cracks and are mechanically sound after removal from the substrate. Further, these parts were measured to have a relative density of 98.6 % (± 1 %) using the Archimedes method. The incorporation of ML modeling removed the need for additional experiments and allowed for the selection of new processing parameters for an increased layer thickness to successfully build high quality parts faster.

Figure 2-11. *LPBF-built $Bi_2Te_{2.7}Se_{0.3}$ parts with nonstandard geometries ($p = 25$ W, $v = 400$ mm/s, $h = 80$ µm, and $t = 75$ µm). Prior to part removal, the substrate was mounted in a polymer epoxy to prevent cracks within the substrate from propagating into and breaking the $Bi_2Te_{2.7}Se_{0.3}$ parts.*

2.6 Conclusions

An iterative system of ML predictive modeling and experimental validation was designed and allowed for the rapid discovery of LPBF processing parameters (p = 25 W, v = 400 mm/s, h = 80 μm, and t = 75 μm) capable of building highly dense, crack-free $Bi_2Te_{2.7}Se_{0.3}$ parts with enhanced geometries. Through this iterative process, prediction maps of the entire processing parameter space were quickly and efficiently derived for n-type bismuth telluride ($Bi_2Te_{2.7}Se_{0.3}$) [73].

The integration of ML techniques meant that a visualization and understanding of changing melt pool dimensions in response to varied laser parameters were quickly achieved. Optimized parameter combinations were then intentionally chosen and used to LPBF complex $Bi_2TE_{2.7}Se_{0.3}$ parts with a high build quality. The existing prediction model could also be used to rapidly identify processing parameters for larger layer thicknesses and faster builds without additional experimental effort. These results are not only significant to the field of TE, but this new augmented ML approach can be more broadly applied when developing a processing strategy for any new AM material.

2.7 Recommendations for Future Work

This work demonstrates the successful LPBF of high-quality, bismuth telluride parts in nonstandard geometries. However, it remains interesting to evaluate the impact of these enhanced geometries on TE properties to validate the modeling work shown in **Figure 2-1**. The question currently remains whether or not these more complex geometries can practically enhance the bulk TE properties and efficiency of these LPBF-built bismuth telluride parts as predicted [7,25,41].

2.8 Appendix

The full line scan melt pool raw data used to iteratively train the ML model and produce the melt pool prediction maps (**Figure 2-7** and **Figure 2-8**) are included below in **Table 2-2**. Breaks in the table represent separate rounds of experimental validation work.

Table 2-2. *The full 93 experimental line scan data points used to generate the predicted melting behavior maps (**Figure 2-**7 and **Figure 2-8**) from ML. We estimate the uncertainty for the experimentally measured dimensions to be ± 5 % (1 sigma).*

Line Scan Parameters		**Experimental Dimensions**	
Power *p* (W)	**Scan Speed *v* (mm/s)**	**Power *p* (W)**	**Scan Speed *v* (mm/s)**
25	400	122.50	206.50
25	400	128.00	215.00
10	550	0.00	0.00
20	350	113.50	115.00
30	500	117.50	275.00
40	250	159.00	659.00
25	400	135.00	207.00
25	400	128.33	215.33
10	550	0.00	0.00
20	350	125.00	116.67
30	500	123.67	267.00
40	250	171.67	626.00
25	350	133.33	237.33
25	350	136.00	239.33
20	550	99.00	75.00
20	450	109.67	86.50
30	300	151.33	411.67
10	300	0.00	0.00
10	400	0.00	0.00
17	300	134.00	87.00
17	300	144.00	97.50
17	500	95.00	71.00
17	500	95.50	68.00
20	250	191.67	226.33
20	250	195.00	256.67
25	550	115.00	241.50

25	550	144.00	191.00
30	400	150.33	345.00
30	400	187.33	246.00
35	400	148.50	437.00
35	400	191.33	304.00
35	550	153.00	215.00
35	550	168.33	162.33
40	550	158.67	311.00
40	550	130.00	348.00
25	250	214.00	317.50
25	250	199.00	305.50
30	250	204.00	494.00
30	250	208.00	510.50
30	350	184.00	375.00
30	350	174.00	400.00
35	250	251.00	598.00
35	250	252.50	546.00
35	375	216.50	353.50
35	375	212.50	325.00
35	475	163.00	314.50
35	475	172.00	314.00
40	350	196.00	444.00
40	350	199.50	462.50
40	450	156.50	373.50
40	450	169.00	376.00
25	400	182.00	162.00
25	400	202.00	140.00
27	450	214.50	136.00
27	450	200.50	139.50
30	550	205.00	150.00
30	550	161.50	183.50
27	300	172.50	353.50
27	300	202.00	260.50
30	400	180.00	225.50
30	400	165.50	347.50
38	475	168.00	348.00
38	475	139.00	358.50
20	500	122.00	134.00
20	500	124.00	108.67
25	400	180.67	195.67

25	400	183.67	208.67
25	450	154.33	194.00
25	450	155.33	233.00
25	500	150.33	190.33
25	500	167.67	210.50
27	450	181.67	144.67
27	450	238.00	93.00
30	450	208.67	136.67
30	450	182.33	228.67
33	425	197.00	195.67
33	425	175.33	253.67
33	500	120.67	311.00
33	500	110.67	329.33
17	300	139.00	102.90
17	300	133.67	97.37
18	350	124.50	121.50
18	350	141.67	127.00
20	300	170.00	221.00
20	300	167.00	186.67
25	300	162.00	404.67
25	300	216.33	273.00
37	400	213.67	239.67
37	400	141.00	442.67
38	500	141.33	320.67
38	500	132.00	324.00
40	450	146.33	362.67
40	450	132.00	429.67

Chapter 3. Point Defect and Grain Manipulation via Post-Process Heat Treatment of LPBF-Built TE Parts

3.1 Introduction

3.1.1 Intrinsic Point Defects in V_2VI_3 Compounds

Existing research has emphasized the role of intrinsic point defects to influence the charge carrier concentration of TE V_2VI_3 materials. The primary focus of these works has been to identify and explain the multiple methods that can control the formation of antisite and vacancy point defects. These studies are motivated by the fact that these intrinsic point defects can act as electron donors or acceptors to increase the charge carrier concentration and facilitate either n-type or p-type character, respectively [26,27,74,75].

For simplicity, the following discussion of intrinsic point defects will be carried out using Bi_2Te_3. However, these relationships remain true for all combinations of V_2VI_3 compounds (V = Group V elements Sb and Bi; VI = Group VI elements S, Se, and Te). In Bi_2Te_3 compounds, the possible intrinsic point defects are Bi_{Te}', $Te_{Bi}^{\cdot}$, V_{Bi}''', or $V_{Te}^{\cdot\cdot}$ [27]. Bi_{Te}' are cationic antisite defects that involve a Bi atom (five outer shell electrons) sitting on a Te site (six outer shell electrons). As a result, Bi_{Te}' defects act as electron acceptors and create one hole carrier due to a +3 charged cation sitting on a -2 anionic lattice site. $Te_{Bi}^{\cdot}$ are anionic antisite defects that each donate one electron to charge balance the presence of a -2 charged anion on a +3 charged cationic lattice site. V_{Bi}''' are cationic vacancies that act as electron acceptors, each creating three hole carriers to charge balance the missing cationic bismuth. Finally, $V_{Te}^{\cdot\cdot}$ are anionic vacancies that each donate two free electrons to charge balance the missing anionic telluride. A summary of these intrinsic point defects and their charge carrier contributions is provided in **Table 3-1**. Additionally, a simplified depiction of these vacancy and antisite point defects is shown in **Figure 3-1** for a representative bismuth telluride system.

Table 3-1. *The intrinsic point defects for a Bi_2Te_3 material and their charge carrier contributions. These cationic and anionic point defects are representative of all those possible in V_2VI_3 compounds.*

Intrinsic Point Defect	Bi'_{Te}	V'''_{Bi}	$Te^{\cdot}_{Bi}$	$V^{\cdot\cdot}_{Te}$
Charge Carrier Contribution	1 h^+	3 h^+	1 e^-	2 e^-

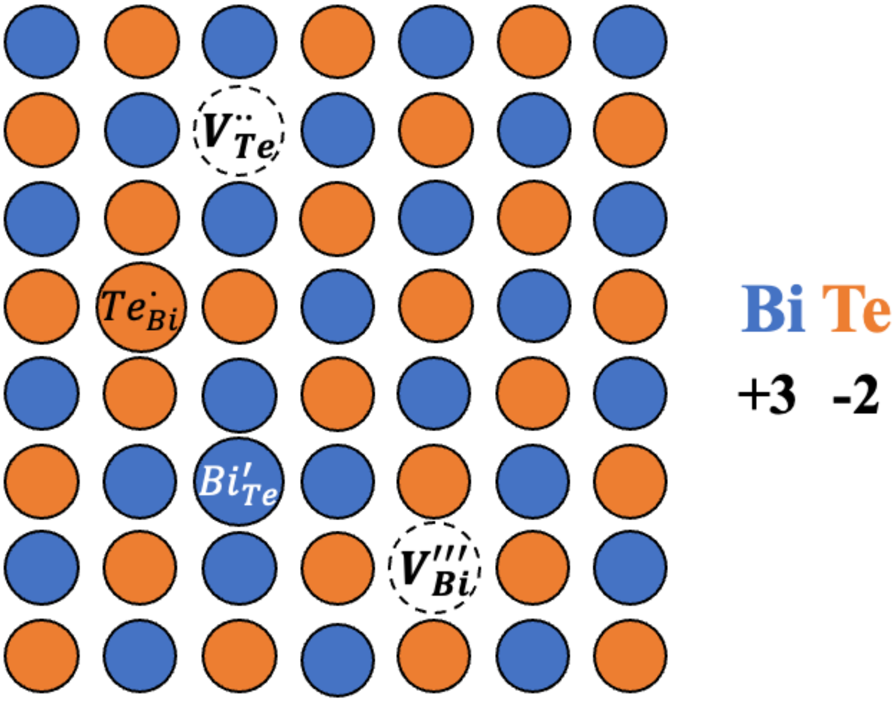

Figure 3-1. *Simplified representation of the Bi'_{Te}, $Te^{\cdot}_{Bi}$, V'''_{Bi}, or $V^{\cdot\cdot}_{Te}$ point defects possible in a bismuth telluride material. The bismuth (Bi) atoms are shown in blue, and the tellurium (Te) atoms are shown in orange. The structure shown is not representative of the actual crystal structure for V_2VI_3 compounds, which is trigonal with the space group R-3m.*

While the formation of each of these four intrinsic point defects is possible and observed in Bi_2Te_3 compounds, the preferential formation of specific point defects can be controlled through alterations to their formation energies via compositional changes. This topic is discussed and explored more fully in Chapter 5.

3.1.2 Impact of Annealing on Point Defect Concentration

It is well-established that the equilibrium concentration of a point defects in a material can be estimated by $n^* = N \cdot exp\left(-\frac{E_d}{k_B T}\right)$, where N is the total number of crystal lattice sites, $E_d$is the defect formation energy, k_B is the Boltzmann constant, and T is the temperature [76–78]. According to this Arrhenius relationship, the defect concentration will increase rapidly with temperature and the point defects with lower formation energies will form in greater numbers. This is true within a reasonable temperature range extending up to the melting temperature. However, the point defect concentration of a material can often be supersaturated above its equilibrium value through rapid cooling, where the quick removal of thermal energy does not provide the point defects with enough time to diffuse through the crystal lattice and annihilate [78]. Experimentally, this relationship has been studied by Kansey *et al.* [79] using positron annihilation lifetime spectroscopy (PALS) on FeAl alloys, where rapid cooling yielded an order of magnitude increase in the vacancy concentration for quenched vs. slow, furnace cooled samples.

Annealing can also be used as a post-processing technique to reduce supersaturated point defect density and achieve equilibrium defect concentrations by providing the energy necessary for atomic diffusion and excess point defect annihilation. This phenomenon has been separately demonstrated for both bismuth telluride samples and LBPF-built parts. These studies also utilized PALS techniques to directly measure the change in vacancy concentrations after annealing. An explanation of the mechanisms behind positron annihilation experiments and interpretation of their results is carried out in *Section 3.2.3*. First, He *et al.* [80] determined that the vacancy concentration of spark plasma sintered (SPS) Bi_2Te_3 nanocrystals can be intentionally lowered through increases in the annealing temperature. This was demonstrated by a maximum decrease in the average positron lifetime from 301 picoseconds to 273 picoseconds after annealing at 500 ºC for three hours. Yao *et al.* [81] demonstrated that the vacancy concentration of LPBF-built stainless steel 316 parts could also be reduced through annealing. In their work, the positron lifetimes of these LPBF-built samples were reduced from roughly 130 picoseconds to 40 picoseconds after annealing at 500 ºC for six hours. This provides evidence that a surplus of vacancy point defects is not only expected to form from the rapid heating and cooling LPBF process, but that they can then be removed through post-processing heat treatment.

Therefore, while separate studies have been conducted on the influence of annealing on point defect concentration in bismuth telluride and LPBF-built samples, this relationship has never been explicitly studied for LPBF-built bismuth telluride parts. This creates a notable knowledge gap where the impact of annealing on point defect concentration and the corresponding changes to charge carrier concentration and mobility in LPBF-built V_2VI_3 compounds have yet to be investigated. This work provides both experimental data and proposed mechanisms by which post-process heat treatments can be used to alter and enhance the TE properties of LPBF-built $Bi_2Te_{2.5}Se_{0.5}$ parts via point defect and charge carrier manipulation.

3.1.3 Thermal Conductivity Minimization via Grain Boundary Engineering

The efficiency of a TE material is typically quantified by the TE figure of merit, $ZT = \frac{\sigma S^2}{\kappa} T$. From this relation, the TE efficiency can be improved by increasing the electrical conductivity (σ) and/or decreasing the thermal conductivity (κ). However, it is known that the overall κ has both a lattice (κ_L) and electronic (κ_E) component, a relationship that is described by $\kappa = \kappa_L + \kappa_E$ [82]. As a result, one of the primary challenges when it comes to improving TE performance is the simultaneous achievement of both reduced thermal transport and enhanced charge carrier transport. Recent work has emphasized the role of grain boundaries as a potential method to de-couple the electron and thermal mobilities while simultaneously achieving a reduced thermal conductivity through targeted improvements to phonon scattering.

Phonons are quantized quasiparticles that describe lattice vibration waves and transport thermal energy in the direction of their motion [77]. As a result, any disruptions to the crystal lattice can disrupt and limit phonon transport. κ_L is a measurement of the phonon contribution to thermal transport and can be reduced through an increase in phonon scattering sites. There are many possible phonon scattering mechanisms in semiconductor materials and when they operate independently from each other, their collective impact is often summarized using Matthiessen's rule [83]:

$$\frac{1}{\tau}=\frac{1}{\tau_U}+\frac{1}{\tau_A}+\frac{1}{\tau_D}+\frac{1}{\tau_e}+\frac{1}{\tau_B}+\cdots,$$

where τ is the phonon lifetime (or τ^{-1} is the scattering time) and refers to the average time between phonon collisions [84]. Matthiessen's rule allows one to approximate τ by separately considering and totaling the impacts of all relevant scattering mechanisms. These can include Umklapp (τ_U), phonon-alloy (or defect) (τ_A), phonon-dislocation (τ_D), phonon-electron (τ_e), and phonon-boundary (τ_B) scattering [83,85–87]. Umklapp scattering refers to the intrinsic, anharmonic phonon-phonon scattering that is present in all materials.

Heat carrying phonons, as descriptors of lattice vibration waves, cover a wide range of frequencies (ω) and the most effective κ_L reduction mechanisms are those that utilize a full-spectrum strategy to target and scatter as many phonons as possible and reduce thermal transport [88]. Point defects most effectively scatter high-frequency phonons with scattering times that relate to the phonon frequency by $\frac{1}{\tau_A} \sim \omega^4$. In contrast, grain boundaries target low-frequency phonons with a frequency-independent scattering time, $\frac{1}{\tau_B} \sim \omega^0$ [89]. However, few microstructural features naturally scatter phonons in the mid-frequency range. In their work with a $Bi_{0.5}Sb_{1.5}Te_3$ material, Kim *et al*. [89] found that the dense, periodic dislocation arrays that arise from low angle grain boundaries (LAGBs) can effectively target mid-frequency phonons with both $\frac{1}{\tau} \sim \omega$ and $\frac{1}{\tau} \sim \omega^3$. Additionally, these low-energy, semicoherent grain boundaries are expected to have a low energy barrier height that avoids scattering all but the lowest energy charge carriers [28,84,90].

Numerous prior works have also leveraged theoretical simulations to calculate the contributions of phonons with varied mean free paths to the accumulative thermal conductivity in bismuth telluride alloys [91–93]. In particular, Wang *et al*. [94] utilized time-domain normal-mode analyses (TD-NMA) and found that 80 % of the total κ_L came from phonons with mean free paths between 1 nm and 10 nm in binary Bi_2Te_3. Therefore, it was argued that nanostructures are needed to significantly reduce κ_L for an enhanced TE efficiency. In their work, Kim *et al*. [89] demonstrated the capability of liquid-phase compaction to create $Bi_{0.5}Sb_{1.5}Te_3$ TE parts with LAGBs. These dense dislocation arrays were found to have misfit spacings of roughly 2.5 nm and accompanying misorientation angles of approximately 5 º, as confirmed using fast Fourier transform (FFT) imaging. Ultimately, it was shown that these low-energy LAGBs were capable of not only dramatically reducing the phonon transport and thermal conductivities of their $Bi_{0.5}Sb_{1.5}Te_3$ samples, but that this could be accomplished without substantially reducing their carrier mobilities or electrical conductivities.

In summary, LAGB formation has been demonstrated as a viable method for enhancing TE efficiency in bismuth telluride materials by not only reducing the κ_L, but also de-coupling phonon and electron transport. Additionally, prior work has found that the high thermal gradients associated with LPBF can yield a preferential formation LAGBs in stainless steel alloys [95,96].

Therefore, LPBF presents a possible, alternative manufacturing strategy to build bismuth telluride parts with enhanced TE performance through LAGB development. However, the creation of LAGBs in LPBF-built bismuth telluride parts and their impact on the TE properties have not yet been studied.

3.2 Methods

3.2.1 Sample Fabrication and Starting Powder

Gas atomization was employed to create the starting powder used during the LPBF fabrication of the following samples. The composition of the initial powder supply was $Bi_2Te_{2.5}Se_{0.5}$ and this stoichiometry was confirmed using a combination of both X-ray fluorescence (XRF, **Table 3-2**) spectrometry and X-ray diffraction (XRD, **Figure 3-2**) techniques.

Table 3-2. *XRF composition results for the Bi2Te2.5Se0.5 starting powder. The data is provided in atomic percent (%).*

X-Ray Fluorescence (XRF)	**Bismuth**	**Tellurium**	**Selenium**
Atomic Percent (%)	40.7	50.4	8.9

In total, five $Bi_2Te_{2.5}Se_{0.5}$ parts were built for this investigation. They were all constructed using the same processing parameters and scan strategy as the nonstandard geometry, three-dimensional parts discussed in *Section 2.5.1* and shown in **Figure 2-11**. These processing parameters are p = 25 W, v = 400 mm/s, h = 80 μm, and t = 75 μm. Three of the samples were constructed as rectangular prisms with dimensions of 4 mm x 4 mm x 5 mm for the purposes of TE property measurements. The remaining two $Bi_2Te_{2.5}Se_{0.5}$ samples were constructed as rectangular prisms with dimensions of 9 mm x 3 mm x 2 mm for positron annihilation spectroscopy

(PAS) and Hall measurements. The dimensions of these samples were determined based upon the required geometries for the relevant analysis technique.

For the TE property and Hall measurements, data was acquired through the bulk samples along the long axis (5 mm and 9 mm, respectively). The long axis for both samples aligned with the transverse direction, which is perpendicular to the build and scan directions for LPBF-built parts (**Figure 1-2**). The PAS data was collected at the center of the larger, finely polished 9 mm x 3 mm faces of those samples. TE property, PAS, and Hall measurements were collected for these samples both before and after heat treating to compare the impact of annealing on LPBF-built bismuth telluride samples.

Heat treatment conditions of 350 ºC for 24 hours were selected to provide the necessary thermal energy and time for enhanced atomic diffusion, point defect annihilation, and dislocation recovery [77] without the crystallographic texture loss and defect-free grain nucleation associated with recrystallization, which has previously been observed in bulk bismuth telluride materials at 450 ºC [97,98]. Additionally, prior work by Hu *et al*. [99] on the LPBF fabrication of a similar $Bi_2Te_{2.7}Se_{0.3}$ material found that their strong, LPBF-produced texture was maintained after annealing at 350 ºC for 24 hours, indicating that recrystallization had not occurred. However, comparisons of the TE properties before and after annealing were not carried out during their study.

All five samples were sealed inside of argon-filled, fused quartz tubes during annealing. Finally, XRD was also used to confirm that the $Bi_2Te_{2.5}Se_{0.5}$ crystal structure was maintained from the starting powder after both the LPBF and annealing processes without the formation of any new phases (**Figure 3-2**).

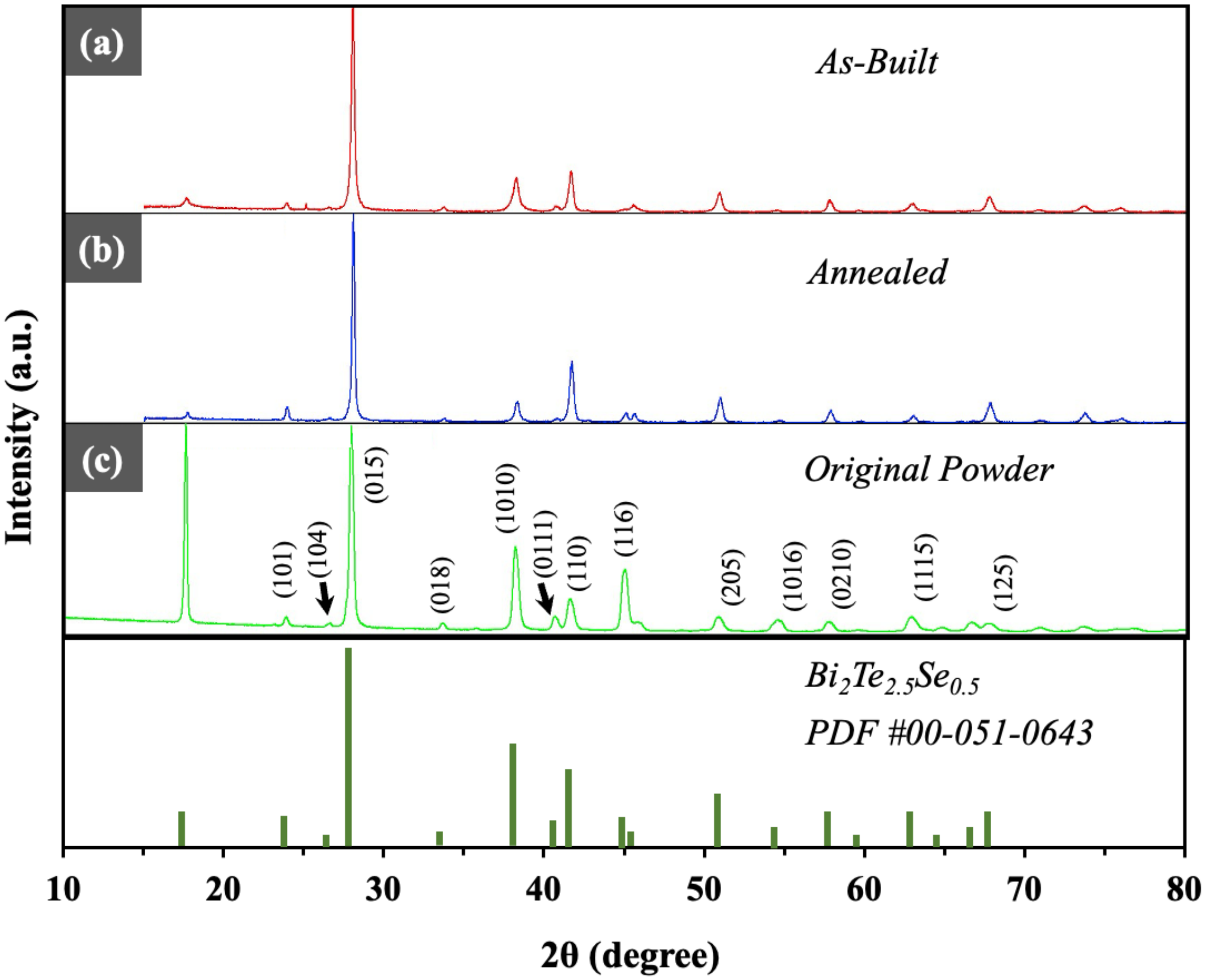

Figure 3-2. *XRD patterns for the (**a**) as-built LPBF-built $Bi_2Te_{2.5}Se_{0.5}$ sample, (**b**) the annealed LPBF-built Bi2Te2.5Se0.5 sample, and (**c**) original $Bi_2Te_{2.5}Se_{0.5}$ starting powder. The LPBF-built parts were constructed using the same original $Bi_2Te_{2.5}Se_{0.5}$ starting powder. The patterns are well-matched in position to one another and to the database values for $Bi_2Te_{2.5}Se_{0.5}$ (PDF#00-051-0643).*

3.2.2 TE Property Measurements

The TE properties measured for this study were the thermal conductivity (κ), electrical conductivity (σ), and Seebeck coefficient (S). The κ was calculated using the equation: $\kappa = dDC_p$, in which d is the thermal diffusivity [cm^2/s], D is the density [g/cm^3], and C_p is the specific heat

[J/(g*K)] [100,101]. The d was measured using a laser flash analysis (LFA) technique that involved a YAG laser, InSb detector, and ASTM 1461 system inside of an Anter FL5000 graphite furnace used to control the environment temperature [102]. In LFA, one face of a sample is heated with a light pulse and the corresponding temperature increase on the plane-parallel opposite face is measured as a function of time to calculate the d of a specimen. The C_p was measured using a differential scanning calorimetry (DSC) process in a Netzsch DSC 404C system. This DSC method involves the measurement of energy required to raise a sample's temperature in comparison to a reference [103]. Ultimately, these two techniques are used to measure the thermal diffusivity and specific heat values necessary to calculate the total thermal conductivity, κ.

S and σ measurements were both conducted using an ULVAC system, Model ZEM-3 M8 (**Figure 3-3**). These measurements are similarly conducted inside of a furnace to set the environmental temperature and collect temperature-dependent (TD) data. For the S, a sample is set vertically between two blocks, one of which contains a heating element. Once the furnace reaches the desired temperature, the heating element is used to generate a thermal gradient and the temperature difference is measured by two laterally contacting thermocouples ($\Delta T = T_2 - T_1$). The corresponding thermovoltage (V_{th}), or thermal electromotive force (dE), is measured using the same thermocouple electrode contacts to calculate the Seebeck coefficient by $S = \frac{-V_{th}}{\Delta T}$. The σ is measured using a DC four-terminal method that suppresses parasitic influences from the contact or wire resistances for increased measurement accuracy. Inside the same system, but in the absence of a temperature gradient ($\Delta T = 0$), a constant current (I) is applied through the sample and the corresponding voltage drop (V) is measured using the same thermocouple wires separated by a known length (L). Finally, the σ is calculated by $\sigma = \frac{I}{V} \cdot \frac{L}{A}$, where A is the sample's cross-sectional area.

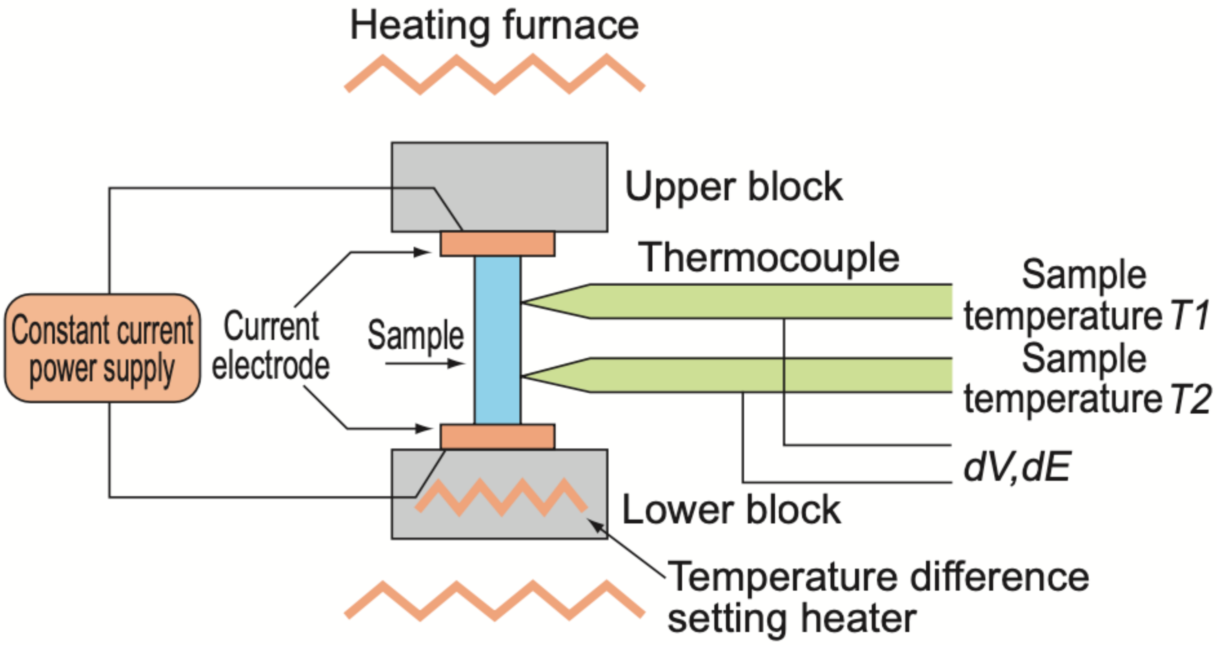

Figure 3-3. *Diagram of the ULVAC, Model ZEM-3 M8 system used for Seebeck coefficient (S) and electrical conductivity measurements (σ).*

In the end, the κ, σ, and S values were used to calculate the TE figure of merit by $ZT = \frac{\sigma S^2}{\kappa}T$. Critically, all TE property measurements were carried out as bulk measurements along the long, 5mm axis of the LPBF-built samples at temperature ranges of roughly 185 ºC to 340 ºC prior to annealing and ranges of approximately 260 ºC to 340 ºC after annealing. Three LPBF-built, $Bi_2Te_{2.5}Se_{0.5}$ samples were measured and used to calculate the average room temperature (RT) TE properties and standard deviations provided in **Table 3-3**.

3.2.3 Positron Annihilation Spectroscopy (PAS)

PAS was used to compare the change in vacancy defect concentration before and after annealing the LPBF-built $Bi_2Te_{2.5}Se_{0.5}$ samples. Positron annihilation is a technique that involves the injection of high-energy positrons into a sample of interest. Those positrons will then rapidly lose kinetic energy and thermally diffuse before annihilating with their anti-particle, electrons.

This mutual annihilation event then generates gamma rays that can be detected. There are two main forms of PAS: positron annihilation lifetime spectroscopy (PALS) and Doppler broadening spectroscopy (DBS) [104]. In either case, the local environment of the encountered electron impacts the characteristics of the emitted gamma ray and allows for the determination of the vacancy defect concentration.

The electron density inside of vacancies is reduced compared to the bulk free state. As a result, positrons that find their way into vacancies can become entrapped, which increases their lifetimes prior to annihilation and gamma ray emittance as measured by PALS. In contrast, positron annihilation occurs much faster in the dense bulk material and positron lifetime is reduced. By comparing average positron lifetimes between samples, increased positron lifetimes can be used as an indicator of increased vacancy concentration [104–106]. Once again, PALS has been previously used to study the vacancy concentration in Bi_2Te_3 nanocrystals and LPBF-built stainless steel parts by He *et al*. [80] and Yao *et al*. [81], respectively.

For this study, the employed PAS technique is DBS. For DBS, the doppler shift and associated broadening of the 511 keV characteristic annihilation gamma rays are used to determine the vacancy concentration from the shape of the detected 511 keV peak, which is evaluated using *S*- and *W*-parameters. The *S*-parameter quantifies the relative count intensity near the central peak of the detected energy curve. In contrast, the *W*-parameter measures the relative contributions from the wings on either side of the peak. Representative figures demonstrating calculations of the *S*- and *W*-parameters from detected gamma rays for DBS are shown in **Figure 3-4**.

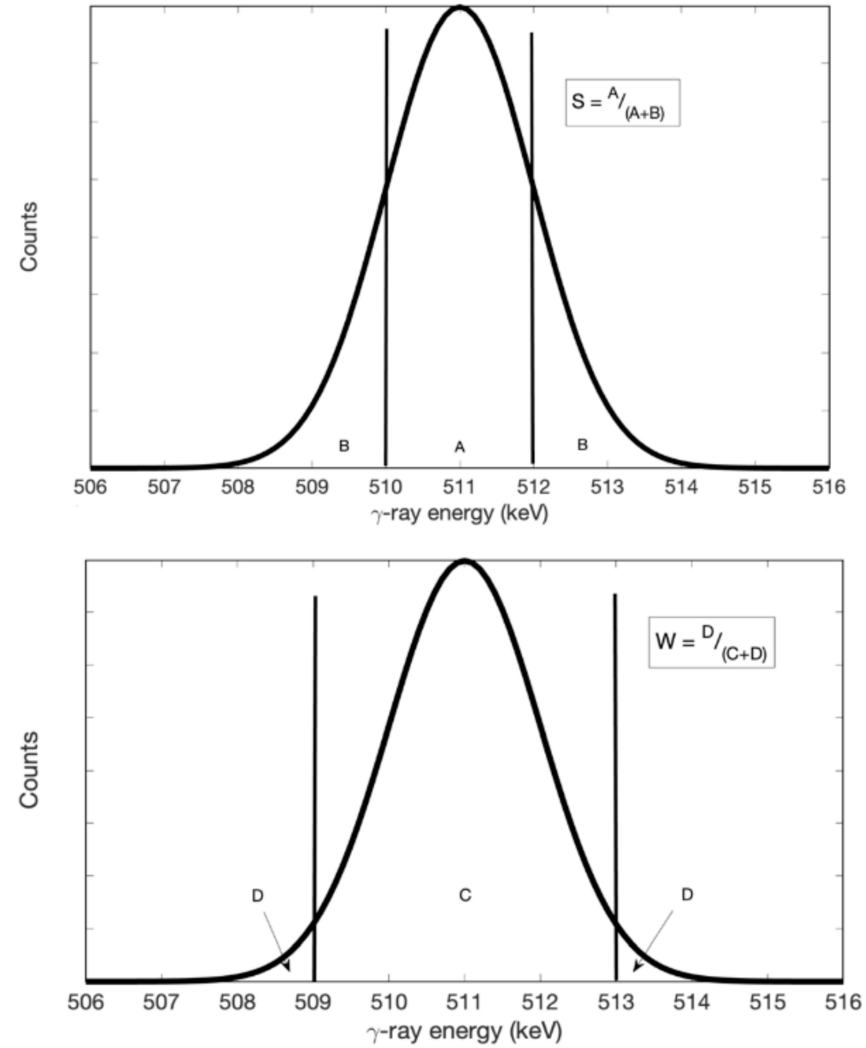

Figure 3-4. *Representative figure demonstrating the calculation of the S- and W-parameters from the detection of 511 keV characteristic gamma rays for Doppler broadening spectroscopy (DBS)* [104].

Positron annihilation events that occur in the bulk take place with higher momentum core electrons, resulting in a greater Doppler shift and more peak broadening (increased *W*-parameter). In contrast, the annihilated electrons in vacancies are lower momentum valence and conduction electrons that contribute less to Doppler shift and peak broadening (increased *S*-parameter) [104]. As such, positron annihilation with the lower momentum electrons in vacancies results in an increased *S*-parameter. Meanwhile, positron annihilation with the higher momentum electrons in the bulk results in an increased *W*-parameter. Therefore, when comparing DBS data between two samples, a higher number of vacancies would be indicated by a relative increase in the S-parameter and/or a decrease in the W-parameter for similar materials [104].

Additionally, DBS techniques also allow for depth-dependent vacancy concentration measurements. The penetration depth of the injected positrons can be modulated through changes to their initial kinetic energy. This is valuable because the bulk and surface level measurements can be separated, where vacancy measurements at the surface may be misleading due to polishing-induced or other surface damage. These DBS measurements were carried out at Washington State University using a ^{22}Na positron emitting isotope as the positron source. The positron data is analyzed and fit to defect depth profiles using the custom software, VepFit (variable energy positron fitting), created by A. van Heen and H. Schut [107].

It is crucial to note that the positively charged positrons only interact with neutral and negatively charged vacancy sites. Therefore, the DBS technique employed in this study is only capable of directly measuring the cationic bismuth vacancies (V_{Bi}''') in a $Bi_2Te_{2.5}Se_{0.5}$ material. However, it is reasonably assumed that changes to the cationic vacancy concentration via heat treating can be considered as representative of changes to all the present point defects in a V_2VI_3 material.

3.2.4 Hall Measurements

Hall measurements were carried out to determine the dominant charge carrier and change in carrier concentration before and after annealing the LPBF-built samples. A four-probe system was utilized with each of the four electrical contacts being placed around the perimeter of the sample to measure the current and voltage through it in perpendicular directions [108–110]. Measurements were conducted from 300 K to 5 K using a custom measurement sequence and a nitrogen-jacketed helium PPMS (Quantum Design, Inc.) with the Alternating Current Transport (ACT) option. By applying a known current through two opposite probes in the presence of a known magnetic field (B), the resulting Hall resistance (R_H) could be calculated [77]. The R_H was measured as a function of multiple positive and negative magnetic fields (-2.5 T < B < 2.5 T) to mitigate voltage probe misalignment effects and thermal instabilities. R_H values for matching ± B were averaged using multiple zero field measurements.

The carrier concentration was calculated from the equation: $n = \frac{1}{\frac{R_H}{B}(eh)}$, where $\frac{R_H}{B}$ is the unconstrained-intercept fitted slope for the collection of R_H and B values, n is the carrier concentration, e is the charge per carrier, and h is the sample thickness [111]. The measurement uncertainty is ± 5 % (expanded uncertainty with $k = 2$). Lastly, a negative n value indicated that the dominant charge carriers were electrons (n-type), while a positive n value indicated that holes were the dominant charge carrier (p-type).

3.2.5 Electron Backscatter Diffraction (EBSD)

Electron backscatter diffraction (EBSD) is a characterization technique that allows for microstructural characterization by providing crystallographic and grain information for a sample of interest. EBSD typically utilizes the electron beam in an SEM to generate Kikuchi patterns from the diffracted electrons. These Kikuchi patterns are specific to the crystal structure and orientation at the incident point of the electron interaction. Therefore, this EBSD method can be used to gather a range of crystallographic information such as phase identification, crystallographic texture, and grain boundary discrimination.

EBSD was specifically used in this study to investigate the impact of the annealing process on the grain size and grain boundary misorientation angles. Ultimately, EBSD was carried out on the 4 mm x 4 mm x 5 mm rectangular prism, $Bi_2Te_{2.5}Se_{0.5}$ samples before and after annealing for comparison. The examined cross-sections were taken perpendicular to the scan direction and an Oxford Instruments EBSD detector within an FEI Helios UC G4 DualBeam FIB-SEM was utilized for data collection. For these measurements, an accelerating voltage of 20.0 kV, a current of 3.2 nA, a spot size of 4.3 nm, a specimen tilt angle of 70.0 °, and a step size of 0.8 μm were used.

3.3 Results and Discussion

After annealing at 350 ºC for 24 hours, it was found that all the TE properties changed in desirable ways to increase TE performance. The Seebeck coefficient (S) increased by about 212 % in magnitude and developed an even stronger n-type character. The thermal conductivity (κ) decreased by roughly 18.4 %, and the electrical conductivity (σ) increased by roughly 17.5 %. Finally, the thermoelectric figure of merit ($ZT = \frac{\sigma S^2}{\kappa}T$) increased substantially by about 1300 % after annealing the LPBF-built $Bi_2Te_{2.5}Se_{0.5}$ samples. The room temperature (RT) S, κ, σ, and ZT values both before and after annealing are provided in **Table 3-3**, along with their percent change values. These annealed TE property values are also comparable to those previously reported by Qiujun et al. [99] for their annealed, LPBF-built $Bi_2Te_{2.7}Se_{0.3}$ parts.

Table 3-3. *Room temperature (RT) TE property measurements conducted for LPBF-built* $Bi_2Te_{2.5}Se_{0.5}$ *samples both with and without annealing at 350 ºC for 24 hours. TE property measurements were collected for three samples in both the as-built and annealed cases with the data provided as the average ± standard deviation. The TE property data was gathered as bulk measurements along the transverse directions of the rectangular prism parts.*

RT Measurements (As-Built vs. Annealed)	S (µV/K)	κ (W/m*K)	σ (S/cm)	ZT
As-Built Transverse	-63.8 ± 3.4	1.62 ± 0.03	416 ± 8.6	0.031 ± 0.003
Annealed Transverse	-199 ± 4.0	1.32 ± 0.04	489 ± 23	0.431 ± 0.039
Percent Change (%)	212	-18.4	17.5	1300

It is clear from this data that the TE efficiency has been increased by the annealing process through improvements to each of the TE properties. However, it now becomes necessary to investigate the material changes that have taken place so that future alterations can be made with intentionality and possibly to even greater effect. In order to best understand and discuss the mechanisms by which annealing has impacted these TE properties, it is most efficient to discuss each separately.

However, it should first be noted that even after annealing, a RT ZT of only 0.431 was reached. This is markedly lower than the benchmark ZT of 1 that is typically achieved in traditionally manufactured TE V_2VI_3 materials. The low ZT value of the annealed, LPBF-built samples is attributed to the fact that the σ is lower and the κ is greater when compared to the TE properties of traditionally manufactured bismuth telluride parts [89,112]. The hope is that by combining this post-process annealing procedure with the enhanced geometries achieved in Chapter 2, LPBF can produce bismuth telluride parts that not only reach but even exceed the TE efficiencies currently being produced through traditional manufacturing methods.

3.3.1 Electrical Conductivity (σ)

The RT electrical conductivity (σ) the LPBF-built $Bi_2Te_{2.5}Se_{0.5}$ parts was found to have increased by about 17.5 % after annealing at 350 ºC for 24 hours. To determine the potential mechanisms, the impact of heat treatment on the point defect concentration, charge carriers, and final σ was investigated.

It is known that the σ of a typical semiconductor depends upon both the charge carrier concentrations and carrier mobilities, as described by $\sigma = en\mu_e + ep\mu_h$, where e is the elementary charge, n is the free electron concentration, p is the hole concentration, and μ_e and μ_h are the carrier mobilities of the free electrons and holes, respectively [77,113]. For n-type semiconductors where the density of free electrons is significantly greater than the hole density, this equation can be simplified to $\sigma = en\mu_e$. However, it is also well-established that the carrier concentration (n) and mobility (μ) of V_2VI_3 semiconductors can be inversely related to one another due to the dual role of charged point defects as both charge carrier contributors and electron scattering centers [114–116]. Additionally, it is generally known for bismuth telluride, semiconducting materials that an increased n can reduce the μ through enhanced electron-electron scattering as well [117–119]. It then follows that a decrease in the number of carrier contributing point defects may have competing effects on the σ for a $Bi_2Te_{2.5}Se_{0.5}$ material.

After annealing, the expected decrease in charge carrier contributing point defects and corresponding decrease in the total charge carrier concentration (both holes and electrons) could result in a reduction of the σ according to $\sigma = en\mu$ [27]. On the other hand, the annihilation of both majority and minority point defects may be beneficial to an increased σ through an increased μ, facilitated by decreases in the charge carrier concentrations and number of point defect scattering sites [31]. To understand the competing impacts of altered charge carrier concentration and mobility on the observed increase in σ after annealing, temperature-dependent (TD) σ measurements were conducted on both annealed and unannealed $Bi_2Te_{2.5}Se_{0.5}$ LPBF-built samples, shown in **Figure 3-5**.

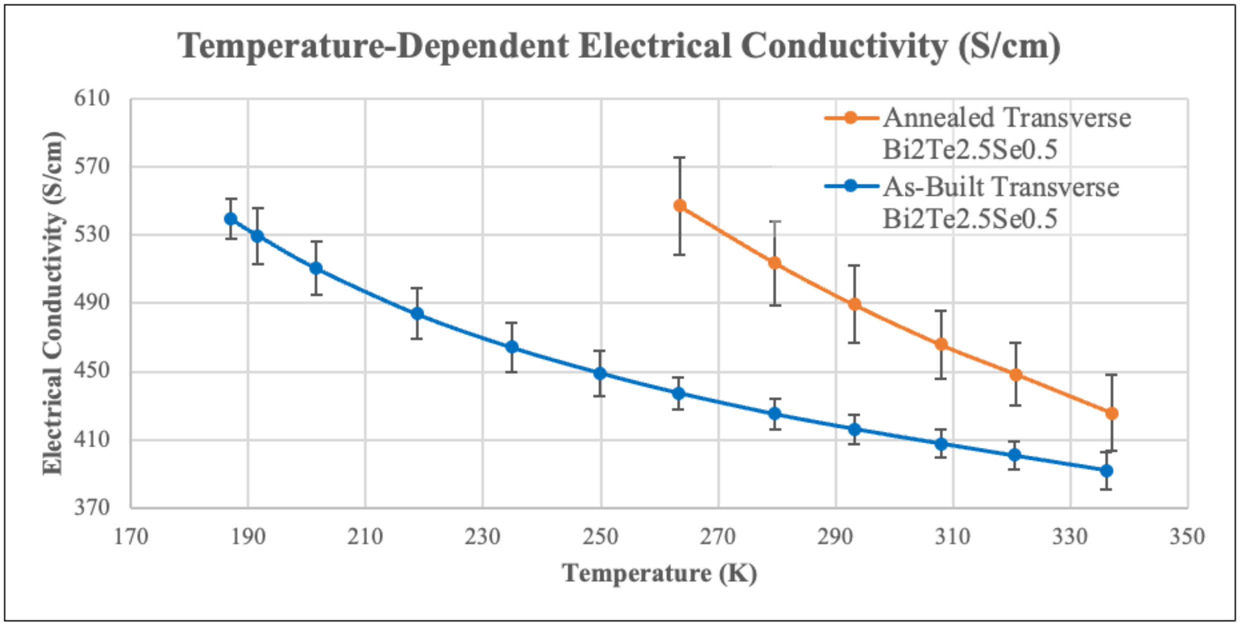

Figure 3-5. *Temperature-dependent (TD) electrical conductivity (σ) measurements for annealed and as-built transverse samples of LPBF-built $Bi_2Te_{2.5}Se_{0.5}$.*

It is observed that the σ decreases with rising temperature for these LPBF-built $Bi_2Te_{2.5}Se_{0.5}$ samples. This is an indication of metal-like behavior and semiconductor degeneracy, a phenomenon that has been frequently observed in bismuth telluride samples that have been intentionally doped and/or rapidly solidified, thus increasing their point defect and charge carrier concentrations [24,74,99,120,121]. Degenerate semiconductors are produced when the charge carrier donor concentration is so high that a narrow energy band is formed that overlaps with the conduction band (n-type) or the valence band (p-type), reminiscent of the overlapping energy bands in metals [113]. With respect to the TD σ results shown in **Figure 3-5**, it is evident that the thermal generation of additional free charge carriers and increased n is not yielding an increase in σ. Instead, the decreased μ caused by increasing temperature and increased electron-phonon scattering is driving a reduction in the σ, similar to the effect observed in metals [77,121].

For LPBF-built TE materials, an annealing-induced decrease in the point defect and charge carrier concentrations and the resulting increase in μ may contribute to the observed increase in σ. The identification of these LPBF-built $Bi_2Te_{2.5}Se_{0.5}$ samples as degenerate semiconductors indicates that a supersaturation of point defects and charge carriers are likely present due to the rapid solidification LPBF process. It is also observed that this semiconductor degeneracy and metal-like behavior is preserved after annealing. To further and directly study the impact that the post-LPBF annealing process has had on point defect and charge carrier concentrations, both positron annihilation and Hall measurements were performed.

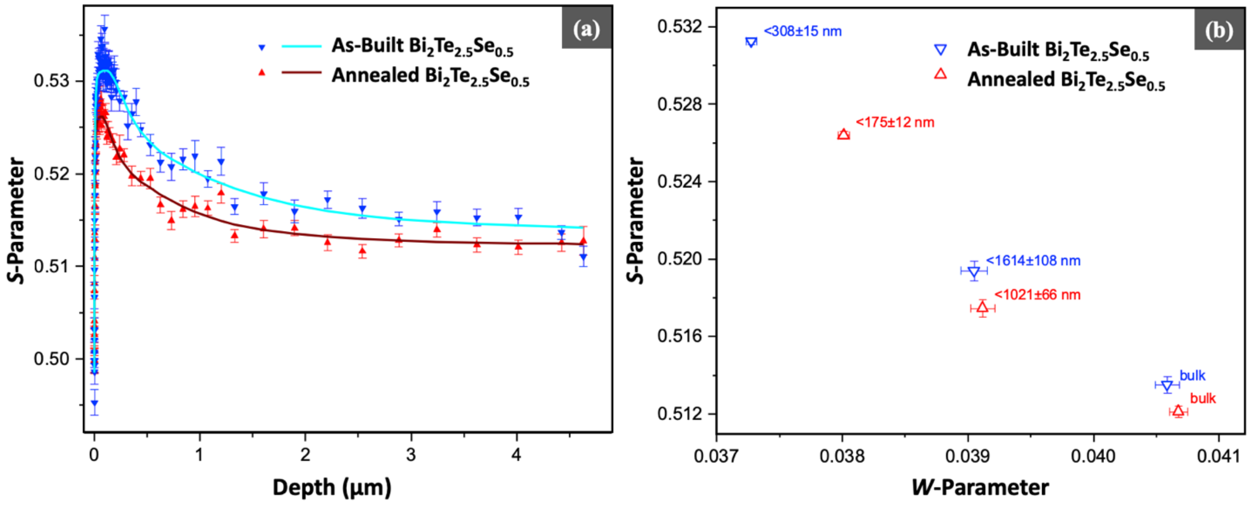

Figure 3-6. *Doppler broadening spectroscopy (DBS) results for as-built and annealed transverse samples of LPBF-built $Bi_2Te_{2.5}Se_{0.5}$. (**a**) shows the S-parameter values for both samples as a function of positron penetration depth and (**b**) compares the S- and W-parameter values for both samples across three subsurface layers.*

DBS was performed on LPBF-built $Bi_2Te_{2.5}Se_{0.5}$ samples both before and after annealing at 350 ºC for 24 hours, and the results are shown in **Figure 3-6**. Recalling the previous discussion on positron annihilation DBS data, an increased *S*-parameter and/or a decreased *W*-parameter indicate a greater number of vacancy point defects [104]. **Figure 3-6a** clearly shows that the annealed sample consistently has a lower vacancy concentration than the as-built sample across all the measured depths up to the maximum 4.5 μm of positron penetration. **Figure 3-6a** also shows that the vacancy concentration is greatest near the surface and then gradually decreases into the bulk for both samples. It should be noted that exact vacancy concentrations cannot be produced without calibration from a sample with a known vacancy concentration value. However, relative vacancy numbers are still produced and can be reliably used for the as-built and annealed comparisons necessary for this study.

The collected positron annihilation data was used to generate depth fit profiles for both samples and it was found that the greatest fits were achieved when separated into three subsurface layers: near-surface, mid-depth, and bulk. **Figure 3-6b** shows these three subsurface layers and compares the *S*- and *W*-parameters for both samples. Across all three layers, the annealed $Bi_2Te_{2.5}Se_{0.5}$ sample consistently shows both a lower *S*-parameter and a higher *W*-parameter. Additionally, comparing the three subsurface levels to one another agrees with the result from **Figure 3-6a** for both samples, that the vacancy concentration decreases with increasing depth across the measured range. Altogether, the positron annihilation DBS data provides significant evidence for a reduction in the vacancy concentration after the 350 ºC, 24 hour anneal. It is re-emphasized that these DBS measurements can only directly measure changes to the cationic bismuth vacancy concentrations. Even still, these changes are considered representative of the annealing effects to total point defect concentration.

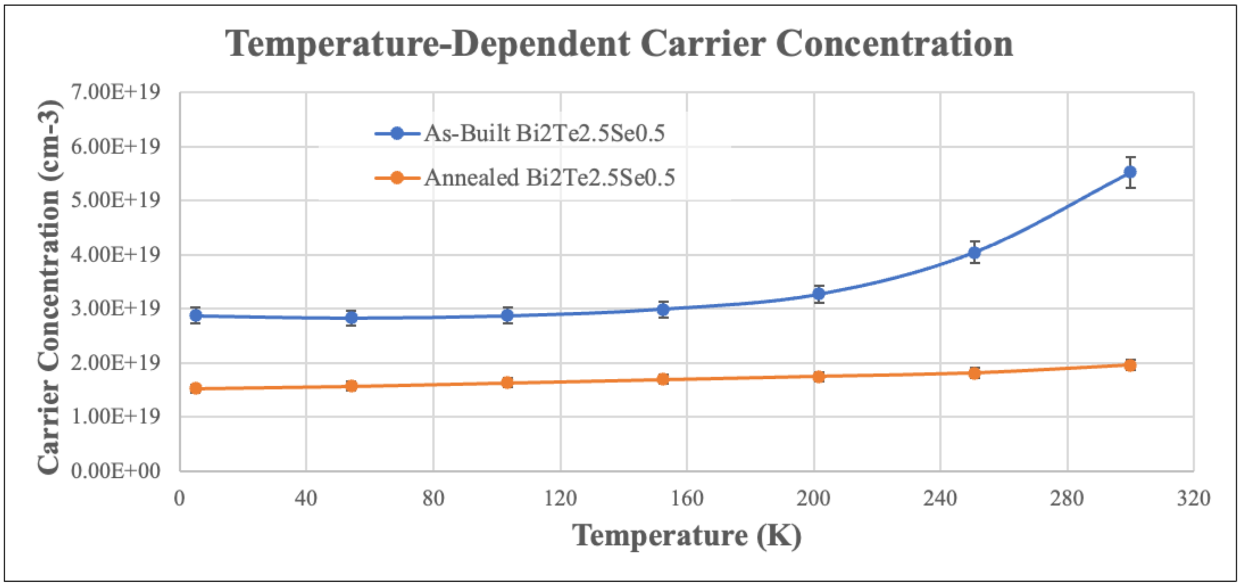

Figure 3-7. *Temperature-dependent (TD) carrier concentration (n) Hall measurements for as-built and annealed transverse samples of LPBF-built* $Bi_2Te_{2.5}Se_{0.5}$*. The measurement uncertainty is ± 5 % (expanded uncertainty with k = 2).*

To correlate the observed decrease in point defect concentration after annealing to the TE properties, the change in carrier concentration was directly measured using Hall measurements. These measurements were carried out for two as-built and two annealed LPBF-built $Bi_2Te_{2.5}Se_{0.5}$ samples. The averages for these TD Hall measurement results are shown in **Figure 3-7**. First, the carrier concentration increases with temperature for both the as-built and annealed samples, although this change is more modest in the annealed sample. This matches expectations as thermal energy elevates valence band electrons into the conduction band to become mobile charge carriers [77]. Second, the carrier concentration is consistently lower for the annealed $Bi_2Te_{2.5}Se_{0.5}$ samples. Once again, this aligns with the results from the positron annihilation experiments, where a reduction in the charge carrier contributing point defects was observed after annealing. The Hall measurement results also identified electrons as the dominant charge carrier for both the as-built and annealed samples, as expected for an n-type $Bi_2Te_{2.5}Se_{0.5}$ material and in agreement with the negative Seebeck coefficients measured and provided in **Table 3-3**.

Additionally, these carrier concentration measurements can also be used to calculate the RT carrier mobilities of the as-built and annealed $Bi_2Te_{2.5}Se_{0.5}$ samples using the relation: $\mu = \frac{\sigma}{en}$. At RT, the carrier concentrations for the as-built and annealed samples were measured to be 5.53 x 10^{19} cm^{-3} and 4.05 x 10^{19} cm^{-3}, respectively. Given that e = 1.602 x 10^{-19} C, the RT carrier mobilities can be calculated as 47.0 $cm^2V^{-1}s^{-1}$ prior to annealing and 75.4 $cm^2V^{-1}s^{-1}$ after annealing. This marks a 60.5 % increase in the carrier mobility after annealing, compared to a 26.8 % decrease in the carrier concentration.

Through a combination of TD σ measurements, positron annihilation DBS, and Hall measurements, three conclusions about these LPBF-built $Bi_2Te_{2.5}Se_{0.5}$ samples can be made. First, the LPBF process produced degenerate semiconductor $Bi_2Te_{2.5}Se_{0.5}$ parts and this degeneracy was maintained after annealing. Second, the cationic vacancy concentration was reduced by the annealing process. Third, the charge carrier concentration was decreased after annealing. When considered altogether, a mechanism can be proposed through which annealing has increased the σ for these LPBF-built parts. It is posited that the rapid solidification process associated with LPBF produced as-built parts with a supersaturation of point defects that consequently contributed a correspondingly large number of charge carriers, resulting in semiconductor degeneracy. By annealing and providing the necessary thermal energy, atomic diffusion and point defect annihilation resulted in a measured reduction in the point defect concentration (**Figure 3-6**). Fewer carrier contributing point defects then yielded the measured reduction in charge carrier concentration (**Figure 3-7**). Ultimately, these effects reduced the number of electron scattering sites and produced an increased charge carrier mobility (+60.5 % at RT) that is responsible for the observed increase in σ for these annealed, LPBF-built $Bi_2Te_{2.5}Se_{0.5}$ parts. In short, annealing produced a pathway by which a reduction in point defect and carrier concentrations resulted in and was compensated by an increased carrier mobility that drove an overall increase in the σ for LPBF-built $Bi_2Te_{2.5}Se_{0.5}$ semiconductors.

It should be noted that other impacts of the annealing process may also have contributed to this increased carrier mobility in addition to the decreased point defect and charge carrier concentrations. Defects and disruptions to an otherwise ordered, uninterrupted crystal lattice can scatter charge carriers and interrupt electron transport [77]. While ionized point defects are one of the more impactful electron transport disruptors, dislocations and grain boundaries have also been identified as potential scattering sites in bismuth telluride [89] and other semiconductor materials [86,87,122]. In order to study the potential impact of grain boundaries on the charge carrier mobility, EBSD data was collected. EBSD crystallographic orientation maps for the as-built and annealed $Bi_2Te_{2.5}Se_{0.5}$ samples can be found in **Figure 3-8** and **Figure 3-9**, respectively.

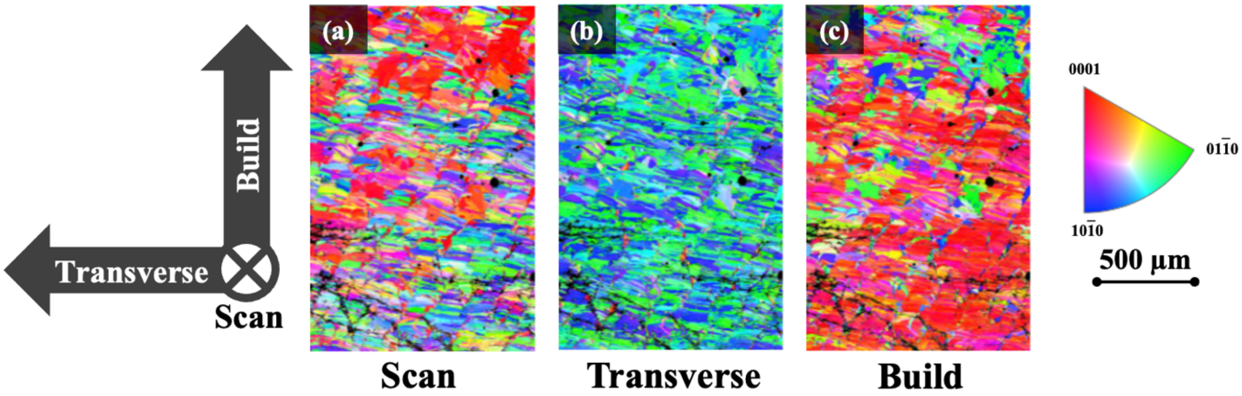

Figure 3-8. *EBSD crystallographic orientation map collected from a LPBF-built $Bi_2Te_{2.5}Se_{0.5}$ sample prior to annealing. (**a**) shows the scan direction, (**b**) shows the transverse direction, and (**c**) shows the build direction. With respect to the sample geometry, the build direction is vertical, the transverse direction is horizontal, and the scan direction is into the page.*

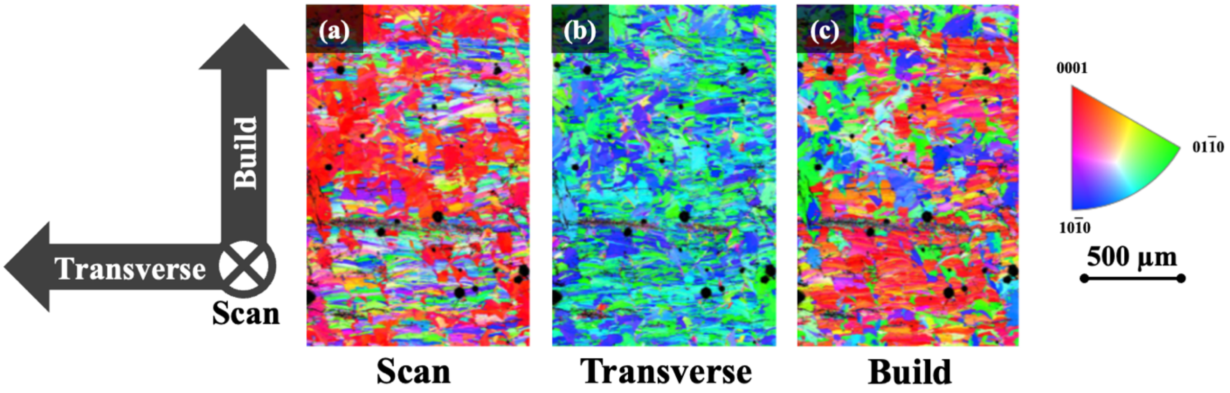

Figure 3-9. *EBSD crystallographic orientation map collected from a LPBF-built* $Bi_2Te_{2.5}Se_{0.5}$ *sample after annealing at 350 ºC for 24 hours. (**a**) shows the scan direction, (**b**) shows the transverse direction, and (**c**) shows the build direction. With respect to the sample geometry, the build direction is vertical, the transverse direction is horizontal, and the scan direction is into the page.*

Grain size analysis conducted from the EBSD data (using a threshold angle of 1.0 º) found that the average max Feret diameter of the as-built, $Bi_2Te_{2.5}Se_{0.5}$ sample was 14.0 µm with a standard deviation of 6.5 µm. After annealing, the max Feret diameter of the grains increased to an average of 15.0 μm^2 with a standard deviation of 8.4 μm^2. While overlap with the standard deviations is acknowledged, this data represents a slight 7.1 % increase in the average grain sizes after annealing at 350 ºC for 24 hours. The impact of this annealing-induced grain growth is that fewer grain boundaries are present in the sample, which reduces the density of electron scattering sites and may contribute to the calculated increase in carrier mobility. This is in addition to the reduced effects from electron-electron and point defect scattering previously discussed.

It has also been previously demonstrated that the rapid, nonequilibrium heating and cooling process of LPBF frequently produces materials with high dislocation densities [123–125]. However, prior work has also shown that annealing can be used as a viable technique to promote dislocation recovery [126] and reduce dislocation density in the bulk for bismuth telluride [127] and LPBF-built materials [95,96]. While not directly studied during this work, it can be reasonably assumed that the bulk dislocation density of these LPBF-built $Bi_2Te_{2.5}Se_{0.5}$ parts was reduced by annealing, as demonstrated in previous work. Additionally, the similar crystallographic textures and grain geometries before and after annealing indicate that while recovery may have occurred, recrystallization likely has not. Therefore, a reduced number of grain boundaries and bulk dislocations after annealing may have also contributed to the improved μ and measured overall increase in the σ.

3.3.2 Thermal Conductivity (κ)

The RT thermal conductivity (κ) of all the LPBF-built $Bi_2Te_{2.5}Se_{0.5}$ parts was found to have decreased by roughly 18.4 % on average after annealing at 350 ºC for 24 hours. TD κ were also collected and are shown in **Figure 3-10**.

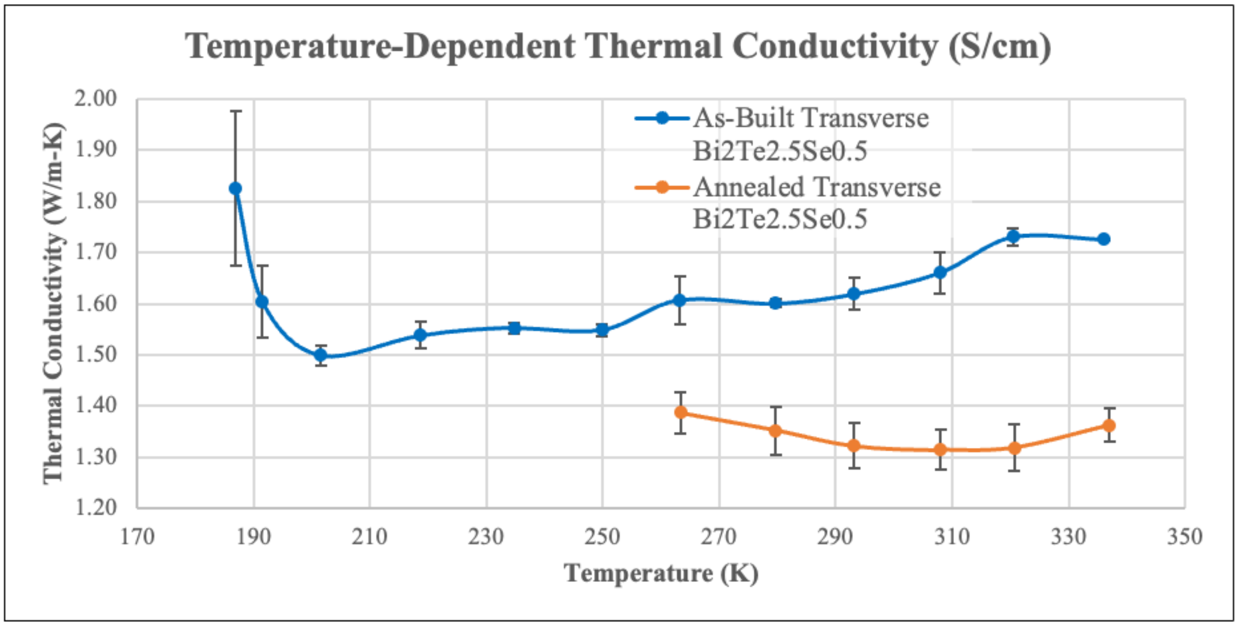

Figure 3-10. *Temperature-dependent (TD) thermal conductivity (κ) measurements for as-built and annealed transverse samples of LPBF-built $Bi_2Te_{2.5}Se_{0.5}$.*

As previously discussed in *Section 3.1.3*, the total thermal conductivity (κ) has both a lattice (κ_L) and electronic (κ_E) component, as described by $\kappa = \kappa_L + \kappa_E$ [82]. The κ_E quantifies the charge carrier contribution to thermal transport and can be calculated from the electrical conductivity using the Wiedemann-Franz Law: $\kappa_E = L\sigma T$, where L is the Lorenz number [80,86]. Acknowledging the annealing-induced increase in the RT σ (**Table 3-3)** and the corresponding increase in κ_E that this requires, it is argued that the measured decrease in κ must be the result of a proportionately larger reduction in the lattice thermal conductivity (κ_L). As a result, this section of the work will be focused specifically on the κ_L and proposes a possible mechanism for an annealing-induced reduction in phonon transport that explains the measured decrease in κ for these LPBF-built $Bi_2Te_{2.5}Se_{0.5}$ parts.

Typical expectations for the effects of annealing may be a reduction in phonon scattering sites and an increase in κ_L via increased phonon transport. The positron annihilation (**Figure 3-6**) and Hall measurement (**Figure 3-7**) results shown and discussed in *Section 3.3.1* provide significant evidence for a reduction in the charged point defect and free electron concentrations, respectively. Additionally, it was observed and expected that the density of grain boundaries and bulk dislocations has also been decreased by the annealing process. As mentioned in *Section 3.1.3* while discussing Matthiessen's rule, these disruptions to the crystal lattice typically act as phonon scattering sites and their removal should benefit phonon mobility and thermal transport [83,85–87,89].

However, prior work has also emphasized the role of grain boundaries as a filter to de-couple electron and phonon transport through alterations to the grain boundary misorientation angle. As previously discussed in *Section 3.1.3*, Kim *et al.* [89] dramatically reduced the phonon transport and thermal conductivities of their $Bi_{0.5}Sb_{1.5}Te_3$ TE parts through the formation of low-energy LAGBs by liquid-phase compaction. Further, this was accomplished without substantially reducing their electrical conductivity since electrons are minimally scattered by semicoherent LAGBs.

It is believed that similar LAGBs and κ results can be achieved in $Bi_2Te_{2.5}Se_{0.5}$ parts through LPBF, where high thermal gradients have been previously shown to preferentially form LAGBs in stainless steel alloys [95,96]. In order to investigate this further and study the effects of annealing on $Bi_2Te_{2.5}Se_{0.5}$ samples, the EBSD data shown in **Figure 3-8** and **Figure 3-9** was used to measure the distribution of grain boundary misorientation angles in the as-built and annealed $Bi_2Te_{2.5}Se_{0.5}$ samples. This data is provided in **Figure 3-11**.

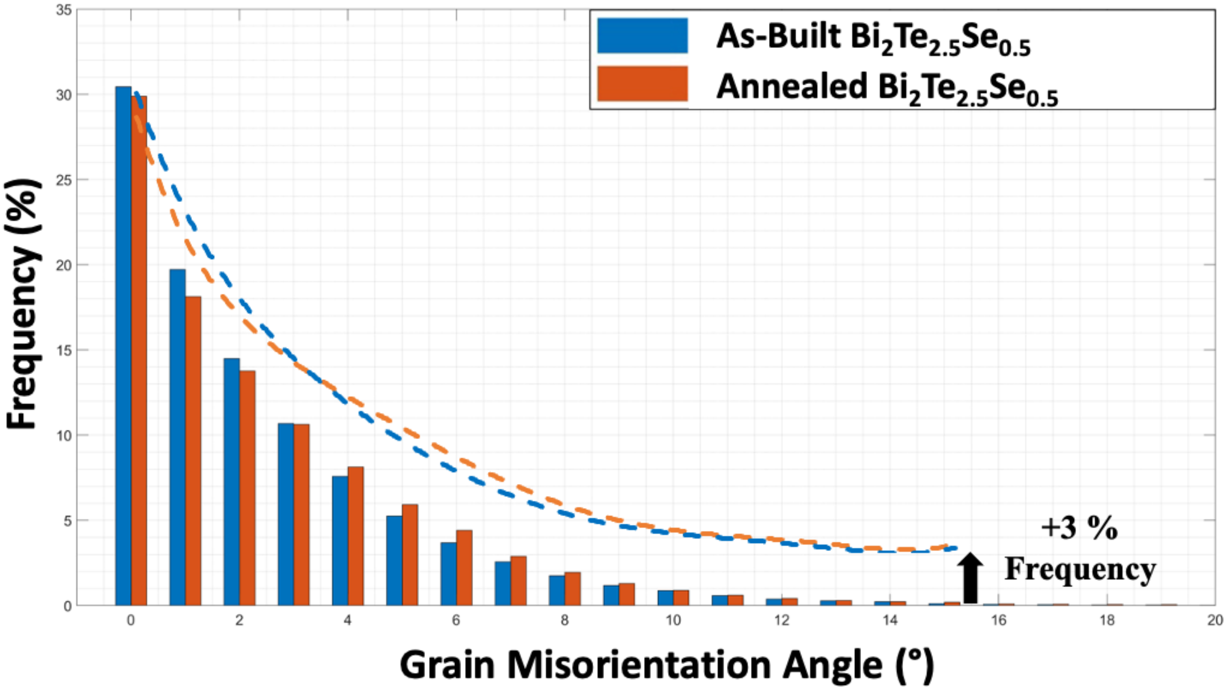

Figure 3-11. *Grain boundary misorientation angles for a LPBF-built $Bi_2Te_{2.5}Se_{0.5}$ sample before and after being annealed at 350 ºC for 24 hours. For visual clarity, the trend lines have been transposed up by +3 % frequency.*

First, this data shows that the LPBF process has produced $Bi_2Te_{2.5}Se_{0.5}$ parts that are almost entirely composed of LAGBs (less than 15 º [128]). Second, after annealing, the relative frequencies of higher misorientation angles (>3 %) have slightly increased. With respect to the data shown in **Figure 3-11**, the as-built samples have a greater relative frequency below a grain misorientation angle of 3 º. However, above a 3 º grain misorientation angle, a transition occurs where the annealed samples now have a greater frequency. This indicates that the distribution of grain misorientation angles has been shifted slightly higher after annealing. Additionally, the average grain boundary angles of the LAGBs were calculated to be 2.82 ° and 2.99 ° for the as-built and annealed $Bi_2Te_{2.5}Se_{0.5}$ samples, respectively. Therefore, this data provides evidence for a roughly 6.0 % increase in grain boundary misorientation angles after annealing and it is proposed that this observed increase in the grain boundary angles (while still maintaining LAGBs) is responsible for the annealing-induced reduction in κ_L due to an increase in grain boundary dislocation density. This observed change in grain boundary angles also makes physical sense, as the annealing-induced recovery and motion of the dislocations from the bulk to the grain boundaries is expected to result in an increased dislocation density and misorientation angles at the LAGBs.

In 1955, Klemens postulated that for LAGBs below 15 °, the phonon scattering probability will increase with increasing misorientation angle and accompanying decrease in dislocation spacing at the grain boundaries [129]. More recently, phonon transport across grain boundaries has been both simulated [128] and experimentally [130] demonstrated for two-dimensional graphene. Lee *et al*. [130] specifically found that the in-plane thermal conductivity of graphene was reduced by roughly 40 % as the misorientation angle between neighboring grains was increased from 0 ° to 4 °. The explanation for this observed relationship between misorientation angle and κ for LAGBs is that as the grain boundary angle increases, the corresponding increase in dislocation density will more effectively scatter midfrequency phonons [84,129]. This is particularly valuable for the periodic dislocation arrays present at semicoherent LAGBs, because even at slightly larger angles and greater dislocation densities they do not meaningfully contribute to electron scattering.

It is therefore argued that the measured decrease in κ is the result of an annealing-induced increase in the dislocation densities and misorientations angles at LAGBs that more effectively scatter phonons and decrease the κ_L. Additionally, maintaining a strong majority of LAGBs ensures that charge carrier scattering at grain boundaries remains low and that carrier mobility is not adversely affected. As a result, a de-coupling of phonon and electron transport can be achieved through LPBF-induced LAGB formation and enhanced through small, annealing-induced changes to their misorientation angles and dislocation densities. These are similar to the findings of Kim *et al*. [89], who successfully produced LAGBs in their $Bi_{0.5}Sb_{1.5}Te_3$ TE parts through liquid-phase compaction to improve midfrequency phonon scattering. While further increases to the grain boundary angles and formation of high angle grain boundaries (HAGBs) may improve phonon scattering and further reduce the κ_L and κ, such a change will also increase their energy barrier height and improve electron scattering [84]. As a result, this annealing-induced modification must also be balanced between thermal and electrical transport.

3.3.3 Seebeck Coefficient (S)

After annealing, it was observed that the magnitude of the RT *S* increased by roughly 212 %, becoming more negative and enhancing the n-type character of these LPBF-built $Bi_2Te_{2.5}Se_{0.5}$ samples. The TD *S* measurements are also provided for both the as-built and annealed samples in **Figure 3-12**.

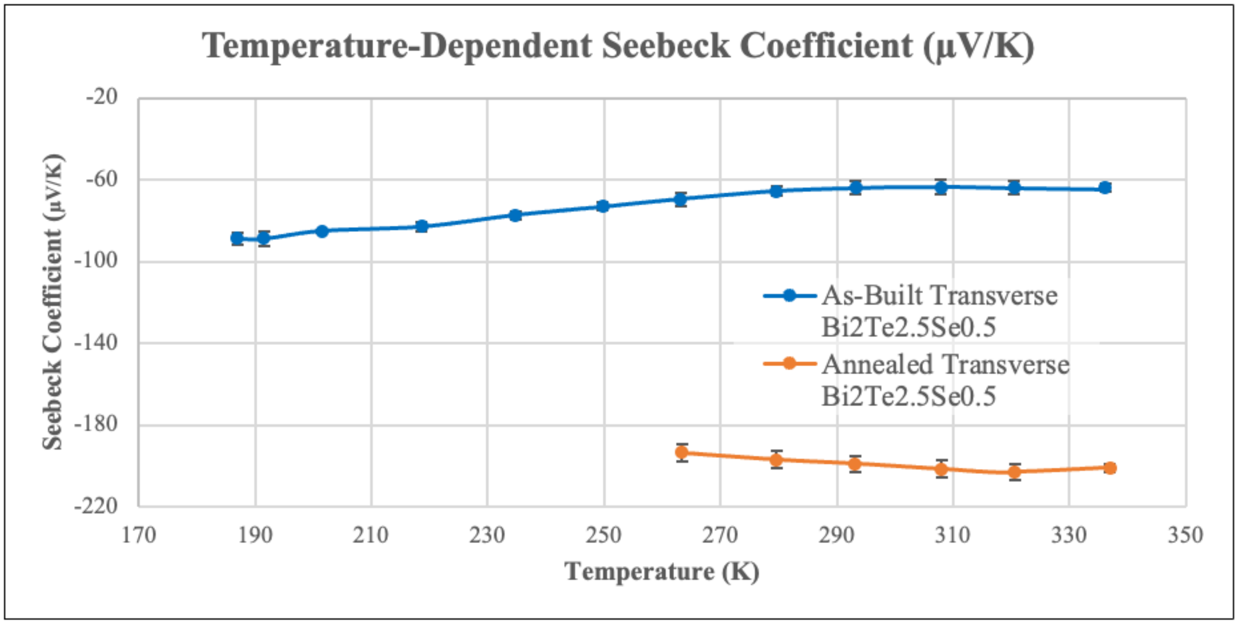

Figure 3-12. *Temperature-dependent (TD) Seebeck coefficient (S) measurements for as-built and annealed transverse samples of LPBF-built* $Bi_2Te_{2.5}Se_{0.5}$.

The S is a measurement of the voltage built up in response to a specific thermal gradient across a material, otherwise stated as $S = -\frac{\Delta V}{\Delta T}$ with units of [V/K]. Additionally, one can also determine the dominant charge carrier from the sign of S, where a negative value indicates an n-type character and a positive value indicates a p-type character [113]. For metals and degenerate semiconductors, it is known that the Seebeck coefficient (*S*) can be calculated using [86,131,132]:

$$S = \frac{8\pi^2 k_B^2 T}{3eh^2} m^* \left(\frac{\pi}{3n}\right)^{2/3},$$

where m^* is the effective mass and *n* is the charge carrier concentration. According to this equation, the Seebeck coefficient has an inverse relationship to the carrier concentration described by: $|S| \sim n^{-\frac{2}{3}}$. The Hall measurement data shown in **Figure 3-7** clearly show a reduction in the carrier concentration after annealing, which is therefore responsible for the observed increase in the magnitude of S. As with many aspects of TE properties and performance, a balancing act exists where reductions in the charge carrier concentration can beneficially improve the S value but may also result in a detrimental lowering of the σ for large alterations. Therefore, the annealing-induced reduction in point defect and carrier concentration can also be a viable strategy for increasing the material's Seebeck coefficient and TE efficiency (*ZT*), as long as the electrical conductivity is not too adversely affected and disproportionately lowered.

3.3.4 Thermoelectric Figure of Merit (ZT)

It was found that the RT *ZT* of the LPBF-built $Bi_2Te_{2.5}Se_{0.5}$ samples increased by 1300 % after annealing at 350 ºC for 24 hours. The TD *ZT* measurements were also collected both before and after annealing and these results are provided in **Figure 3-13**. It is observed that after annealing, the peak *ZT* value is achieved near RT, similar to traditionally manufactured bismuth telluride TE materials.

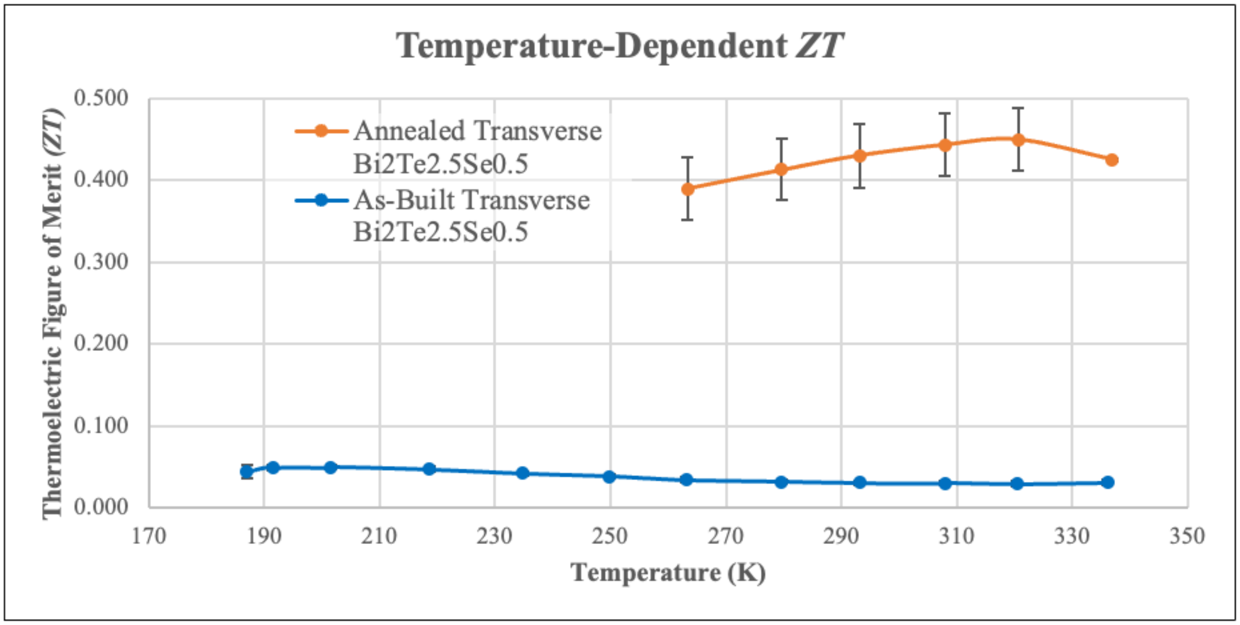

Figure 3-13. *Temperature-dependent (TD) thermoelectric figure of merit (ZT) measurements for annealed and as-built transverse samples of LPBF-built* $Bi_2Te_{2.5}Se_{0.5}$.

Rationalizing the increased *ZT* and TE performance is reasonably straightforward. As demonstrated by the equation $ZT = \frac{\sigma S^2}{\kappa}T$, it is known that the TE efficiency can be improved through increases to the electrical conductivity (σ), increases to the Seebeck coefficient (S), and/or decreases to the thermal conductivity (κ). High performing TE materials rely on their ability to maintain a strong thermal gradient through a low thermal conductivity, while also maintaining sufficient charge carrier transport through a high electrical conductivity. Further, given that the Seebeck coefficient is a direct measure of the voltage built up in a material as a response to a temperature difference, an enhanced Seebeck coefficient will also benefit overall TE performance. Therefore, it not only quantitatively makes sense that the TE figure of merit has increased, but it also logically follows that the annealing-induced changes to the TE properties (**Table 3-3**) have a positive impact on the TE efficiency of these LPBF-built $Bi_2Te_{2.5}Se_{0.5}$ parts.

3.4 Conclusions

After annealing at 350 ºC for 24 hours, it was found that the TE properties and efficiency of LPBF-built $Bi_2Te_{2.5}Se_{0.5}$ parts were improved. First, the RT electrical conductivity (σ) was increased by about 17.5 %. It is argued that this annealing-induced increase in σ is driven by an enhanced carrier mobility (μ) resulting from the removal of electron scattering, charged point defects and a reduced carrier concentration (n). Second, the RT Seebeck coefficient (S) experienced a roughly 212 % increase due to the annealing-induced reduction in carrier concentration caused by the annihilation of supersaturated, carrier contributing point defects. Third, the RT thermal conductivity (κ) decreased by roughly 18.4 %. This change is explained by an increase in the misorientation angles and dislocation densities at the LAGBs that more effectively scatter phonons without adversely impacting the charge carrier transport. Finally, it was found that the RT ZT was improved by about 1300 % after annealing at 350 ºC for 24 hours. When considered altogether, this post-process annealing procedure provides a viable pathway by which a simultaneous improvement in electrical conductivity and reduction in thermal conductivity can be achieved to increase the TE performance of LPBF-built, n-type $Bi_2Te_{2.5}Se_{0.5}$ parts.

3.5 Recommendations for Future Work

Several competing effects result from the annealing of LPBF-built $Bi_2Te_{2.5}Se_{0.5}$ parts. A reduction in the number of carrier contributing point defects has the demonstrated benefit of increasing carrier mobility in the form of diminished electron scattering events. However, point defects can also act as effective phonon scattering sites that beneficially reduce thermal conductivity. Additionally, grain size and grain boundary misorientation angles also must be balanced to minimize phonon transport without greatly diminishing electron transport, or vice-versa.

The result is that while these annealing conditions (350 ºC for 24 hours) did improve TE efficiency, it is likely that TE performance can be further improved through the exploration of additional heat treatments. One of the major challenges to TE improvement has always been the balancing of thermal conductivity minimization and electrical conductivity maximization. While post-process annealing of LPBF-built parts does provide a potential avenue for achieving greater TE conversion efficiency, more work must be done involving the exploration of new annealing conditions to produce the best TE devices possible.

Another possible course of future study would be to explore the impact of additional processing parameters and build strategies on the TE properties of these LPBF-built parts. It is known that altering the laser scan parameters (power, speed, hatch spacing) can be used as a viable method to control temperature gradients and solidification rates in LPBF [34–36]. If these relationships can be better understood for a bismuth telluride material, then alterations to the point defect concentration and grain boundary angles could be intentionally manipulated during the LPBF process and the need for a post-processing anneal may be reduced or even eliminated. However, a high build quality and part relative density would need to be maintained for any new build strategies to be considered practical.

Additionally, a more focused study on the state and role of dislocations in both as-built and annealed LPBF samples could be advantageous. It is known that dislocations disrupt the crystal lattice and scatter both electrons and phonons to varying degrees [27,87,89,122]. It is also known that LPBF can imbue a material with a high number of dislocations and that annealing can be used to remove dislocations [95,96,123–125,127]. However, the exact formation and annealing-induced motion of dislocations both in the bulk and at the grain boundaries has not yet been investigated for LPBF-built bismuth telluride parts. A more rigorous study on the density and locations of dislocations before and after annealing LPBF-built bismuth telluride materials could provide an additional avenue for tuning the thermal and electrical conductivities for improved TE devices.

Chapter 4. Directionally Dependent TE Properties through LPBF Controlled Crystallographic Orientations

4.1 Introduction

4.1.1 Anisotropy of TE Transport Properties in V_2VI_3 Compounds

Bi_2Te_3 (and all other V_2VI_3 compounds) is a member of the tetradymite family and has a rhombohedral/trigonal crystal structure with the space group $R\overline{3}m$. It also consists of stacked layers of $Te^{(1)}$-Bi-$Te^{(2)}$-Bi-$Te^{(1)}$ along the *c*-axis (the [0001] direction) where the $Te^{(1)}$-$Te^{(1)}$ bonds between the repeated layers are weakly bound through van der Waals forces, while the other bonds have both ionic and covalent character [27,133]. As a result of their crystal structure and nearly two-dimensional nature, V_2VI_3 materials typically have strongly anisotropic TE properties. Shen *et al.* [134] previously demonstrated this anisotropy in textured samples of bismuth telluride based polycrystalline alloys, where both the thermal conductivity (κ) and electrical conductivity (σ) were greater when measured in the basal plane (perpendicular to the *c*-axis), as opposed to measurements made in the lateral plane (parallel to the *c*-axis). This anisotropic transport behavior is typically attributed to the complex valence band structure and directionally-dependent differences in the effective masses and acoustic phonon scattering across planes of like and unalike atoms [135,136].

For single crystal Bi_2Te_3 alloys, the changes in σ and κ are not 1:1. Instead, the σ has been measured as roughly 3-4 times larger and the κ around 2 times larger in the basal plane [134,136]. In polycrystalline samples with weaker texture, these increases can diminish to about 1.5-2.5 and 1.4 times larger for the σ and κ, respectively [135]. The result is that while the *ZT* is occasionally found to be isotropic in some polycrystalline materials [134], it is also common for highly textured V_2VI_3 materials to produce an anisotropic ZT attributed to the larger σ anisotropy compared to κ [137]. In these cases, the TE efficiency is also enhanced in the basal plane as expected from the $ZT = \frac{\sigma S^2}{\kappa} T$ expression. Similar trends have been observed in both nanocrystalline thin films [138,139] and single crystals [136] for bismuth telluride compounds.

On the other hand, the Seebeck coefficient (S) has been found to be nearly isotropic for both n- and p-type V_2VI_3 materials as it largely originates from the isotropic density-of-states. However, the S can become anisotropic when affected by bipolar conduction, which typically occurs at elevated temperatures for narrow band gap semiconductors when the charge carrier concentration (and particularly the minority charge carrier concentration) becomes high enough that both holes and electrons participate in energy transport and two-carrier conduction occurs [140]. The result is a reduction in the effective S as it becomes the sum of the two oppositely signed S for the two charge carriers. Further, it is the anisotropic mobility of the conduction and valence bands that causes the S to become anisotropic [137].

A common method of describing the texture of hexagonal materials is to use the Kearns texture factor, F, which quantifies the volume fraction of crystallites with basal poles (c-axis) aligned towards a particular sample direction [141]. A maximum $F = 1$ value indicates that the material is completely oriented with the c-axis in that direction and a high degree of anisotropy, while an F value of 0 indicates a total lack of orientation to the c-axis in that sample direction. Additionally, for three mutually orthogonal sample directions, the F values for the three directions must sum to one. As a result, the Kearns texture factor can be used to numerically quantify and compare the strength of the [0001] texture along various directions for a V_2VI_3 material.

The anisotropy of κ and σ in V_2VI_3 materials present a unique opportunity to intentionally manufacture parts that have directionally enhanced transport properties. Further, this can be accomplished without diminished TE performance and even has the potential to improve the TE efficiency in the same direction as the increased transport properties. One possible application for these materials could be the integration of TE devices into heat exchangers [142]. If the textures of TE parts can be well controlled, then it may be possible to craft devices that have increased κ values in desired directions for enhanced heat extraction without sacrificing TE efficiency. Even in traditionally manufactured TE modules (TEGs and TECs), it is often preferable to utilize TE legs with increased σ along the thermal gradient and in series with the electrically conductive shunts (**Figure 1-1**).

4.1.2 AM-Facilitated Crystallographic Orientation Control

AM-facilitated control over the preferred crystallographic orientation has been repeatedly demonstrated in several material systems. Perhaps the best-known example of site-specific crystallographic texture control has been carried out on Inconel 718 by DeHoff *et al.* [34] who found that by modifying the electron beam scan strategy, they could manipulate the temperature gradients and cooling rates to intentionally vary the produced texture from primarily columnar [001] oriented to randomly oriented grains. Ultimately, they demonstrated this ability by creating the sample shown in **Figure 4-1**, where the letters “DOE” were “written” using a random texture while the rest of the sample maintained a strong <001> grain orientation.

Figure 4-1. *EBSD orientation map demonstrating site-specific crystallographic orientation control as produced by Dehoff et al. in Inconel 718 using electron beam powder bed fusion* [34].

Both intentional and unintentional textures in beam scanning AM processes (such as electron beam and LPBF) are frequently observed. Generally speaking, crystal growth along the most favorable growth direction (typically <001> in metals with cubic structures) will occur along the direction of the maximum thermal gradient, which occurs from the melt pool boundaries to their centerlines and tends to be parallel to the build and/or scan directions [37,99]. For single crystal V_2VI_3 materials, it has been shown that this preferential growth direction is aligned with the *c*-axis (<0001>) [32]. However, the preferred solidification morphology is heavily dependent upon both the temperature gradient (*G*, [K/m]) and the liquid/solid interface velocity (*R*, [m/s]). Through intentional manipulation of the beam scan parameters, alterations can be made to the melt pool size, melt pool shape, *G*, *R*, and the *G*/*R* ratio for control over the solidification morphologies and resulting crystallographic textures. A representative figure showing the shared impact of *G* and *R* on the solidification structure size and morphology is provided in **Figure 4-2** [32]. Through changes to their electron beam parameters, DeHoff *et al*. [34] were able to intentionally traverse the columnar and equiaxed solidification modes to impose spatial, three-dimensional crystallographic grain orientation patterns across multiple layers, as discussed and shown in **Figure 4-1**.

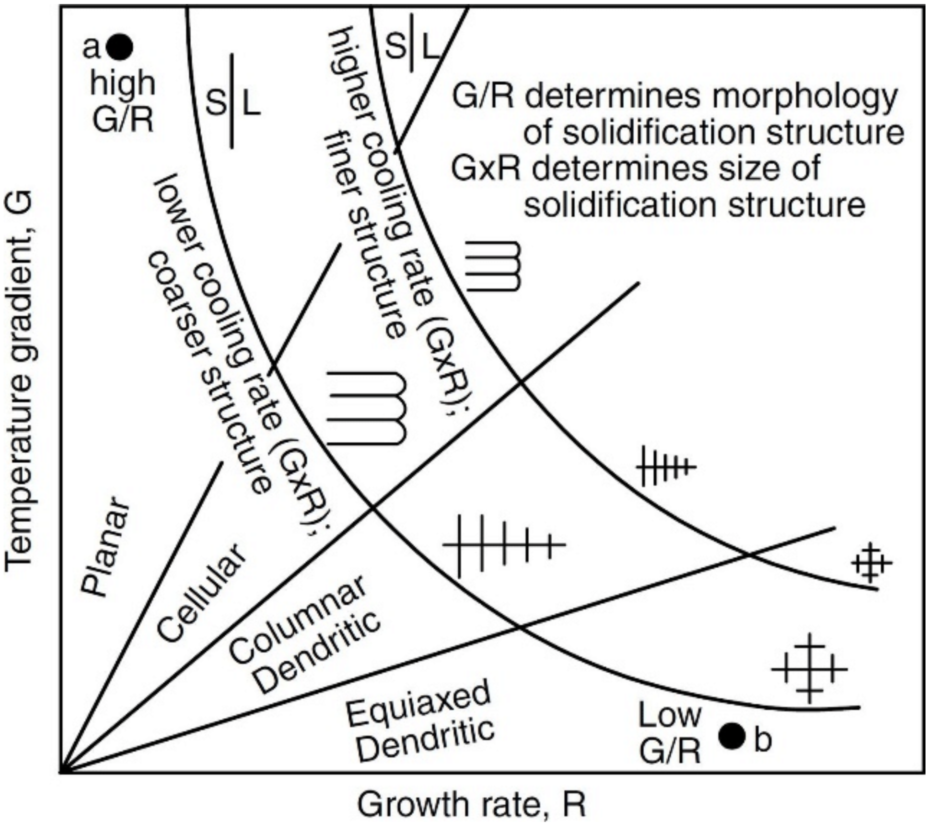

Figure 4-2. *Solidification morphology dependence on the temperature gradient (G, [K/m]) and growth rate (R, [m/s])* [32].

Crystallographic grain orientation control has also been achieved using LPBF for both 316L austenitic stainless steel [35] and chromium [36]. In these LPBF studies, it was found that both a single-crystal-like texture with {001} orientation or a mixed texture with {001} and {011} orientations in the build direction could be produced through laser parameter alterations. Similar LPBF-facilitated preferred crystallographic orientations in $Bi_2Te_{2.7}Se_{0.3}$ parts have been studied, where Welch *et al*. [28] found that an oriented microstructure was generated by LPBF with the basal plane perpendicular to the build direction. Recently, Oztan *et al*. [37] demonstrated through a combination of computational and experimental efforts that both equiaxed and columnar grain growth could be formed in Bi_2Te_3 samples via laser processing through intentional navigation of the *G*/*R* ratio. However, while LPBF-produced crystallographic texture has been observed in both bismuth telluride and other materials, the impact of and connections between this LPBF-induced texture and the anisotropy of their TE properties have not yet been investigated.

4.2 Methods

4.2.1 Sample Fabrication and Starting Powder

The results discussed in this chapter were collected from samples built using the same gas atomized $Bi_2Te_{2.5}Se_{0.5}$ starting powder, processing parameters, and build strategy as previously discussed in *Section 3.2.1*. These processing parameters were $p = 25$ W, $v = 400$ mm/s, $h = 80$ µm, and $t = 75$ µm. Additionally, the line scan vectors were rotated 33 degrees from layer to layer and were constrained to a 90 degree window centered around the designated "scan direction" of the samples. In total, five $Bi_2Te_{2.5}Se_{0.5}$ samples were constructed for this portion of the work. All five of the samples were constructed as rectangular prisms with dimensions of 4 mm x 4 mm x 5 mm. The only change between these samples was that three of them were built such that the long 5 mm axis was the transverse direction and two of them were built such that the long 5 mm axis was the build direction. This distinction was made because all the TE property (σ, κ, S, and ZT) measurements were carried out through the bulk samples and along the longer 5 mm axis based upon the constraints of the measurement techniques. In this way, TE property measurements could be collected along the transverse direction three times and the build direction two times for comparison.

In LPBF parts, there are three significant sample directions: scan, build, and transverse (see **Figure 1-2**). For these purposes, the scan direction refers to the center of the 90 degree line scan window (discussed in *Section 2.2.3*). The build direction refers to the direction normal to the surface of the substrate and is the positive direction of the layer-by-layer construction. Finally, the transverse direction is perpendicular to both the build and scan directions (orthogonal to the build-scan plane).

It should be noted that these three transverse direction $Bi_2Te_{2.5}Se_{0.5}$ samples are the same 4 mm x 4 mm x 5 mm samples as previously constructed and studied in Chapter 3. The average RT TE properties (σ, κ, S, and ZT) for these three samples are reported in **Table 3-3** and will be reproduced in this chapter alongside the measurements of the two build direction $Bi_2Te_{2.5}Se_{0.5}$ samples for comparison. Additionally, TE property measurements were carried out on all five samples both before and then after annealing. Once again, the annealing conditions were the same as those described in *Section 3.2.1* and discussed in Chapter 3. The samples were annealed for 24 hours at 350 ºC after being encapsulated in argon-filled, fused quartz tubes. XRD patterns comparing the as-built and annealed LPBF-built $Bi_2Te_{2.5}Se_{0.5}$ samples to the original starting powder can be found in **Figure 3-2**, which shows that no new phases were formed and that the crystal structure was maintained. The XRD patterns shown in **Figure 3-2a** & **b** were collected from the transverse direction samples and show no change in phase composition to those collected for the build direction samples.

4.2.2 Electron Backscatter Diffraction (EBSD)

As previously discussed in *Section 3.2.*5, EBSD is an analysis technique that utilizes the characteristic Kikuchi bands produced by diffracted electrons to collect crystallographic information for a sample. For this study, EBSD was used to characterize the crystallographic textures formed in $Bi_2Te_{2.5}Se_{0.5}$ samples by the LPBF process both before and after annealing. The crystallographic preferred orientations of these samples were visualized and interpreted using pole figures (PF) and inverse pole figures (IPF) created from the EBSD data. The Kearns texture factors (*F*) were also calculated using this data. These measurements were carried out on the 4 mm x 4 mm x 5 mm rectangular prism samples before and after annealing for comparison. The examined cross-sections were all taken perpendicular to the scan direction, which also collected data on the crystallographic textures in the transverse and build directions. An Oxford Instruments EBSD detector within an FEI Helios UC G4 DualBeam FIB-SEM was utilized for data collection with an accelerating voltage of 20.0 kV, a current of 3.2 nA, a spot size of 4.3 nm, a specimen tilt angle of 70.0 º, and a step size of 0.8 µm.

4.2.3 Thermoelectric (TE) Property Measurements

The thermal conductivity (κ), electrical conductivity (σ), and Seebeck coefficient (S) were measured using the same methods as previously discussed in *Section 3.2.2*. The κ was calculated using the equation: $\kappa = dDC_p$ [100,101]. The thermal diffusivity (d) was measured using a laser flash analysis (LFA) technique that involved a YAG laser, InSb detector, and ASTM 1461 system inside of an Anter FL5000 graphite furnace [102]. The specific heat (C_p) was measured using a differential scanning calorimetry (DSC) process in a Netzsch DSC 404C system. Together, these methods are used to determine the d and C_p values necessary to calculate the total thermal conductivity, κ.

S and σ measurements were both conducted using an ULVAC system, Model ZEM-3 M8 (**Figure 3-3**). Ultimately, the measured κ, σ, and S values were used to calculate the TE figure of merit by $ZT = \frac{\sigma S^2}{\kappa} T$. Again, all TE property measurements were carried out as bulk measurements along the long, 5mm axis of the LPBF-built, $Bi_2Te_{2.5}Se_{0.5}$ samples. Three transverse direction and two build direction samples were measured and used to calculate the average room temperature (RT) TE properties and standard deviations provided in **Table 4-1**, **Table 4-2**, and **Table 4-3**.

4.3 Results and Discussion

4.3.1 LPBF-Produced Crystallographic Texture in $Bi_2Te_{2.5}Se_{0.5}$

To investigate and determine the crystallographic orientations of the LPBF-built $Bi_2Te_{2.5}Se_{0.5}$ samples, EBSD data was collected. These EBSD crystallographic orientation maps are shown in **Figure 4-3** for the (**a**) build, (**b**) transverse, and (**c**) scan directions. With respect to the sample geometry, the horizontal direction is the transverse direction, the centerline of the positive scan vector is into the page, and the positive build direction is in the positive vertical direction, meaning the bottom of the EBSD maps is in the direction of the substrate and the top is in the direction of the sample top surface. PF and IPF generated from this EBSD data are shown in **Figure 4-4** and **Figure 4-5**, respectively.

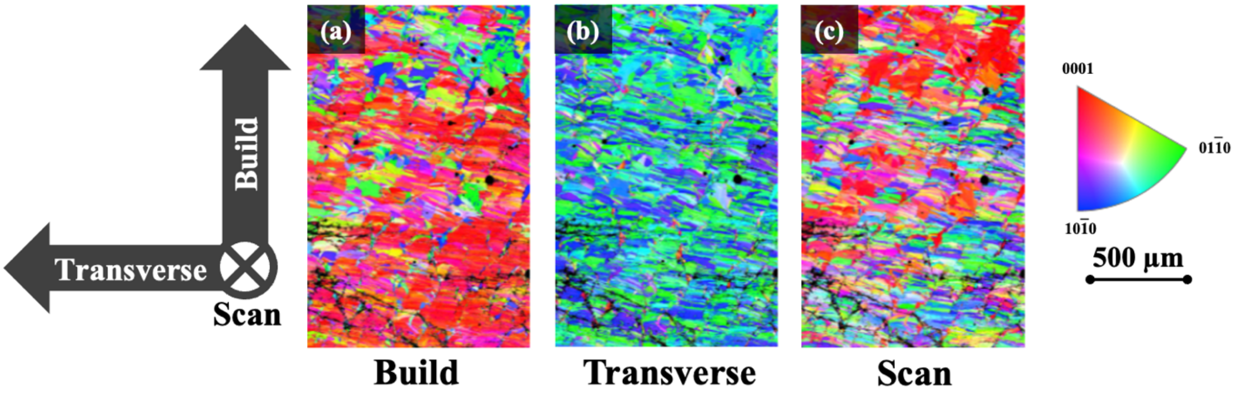

Figure 4-3. *EBSD crystallographic orientation map for a LPBF-built $Bi_2Te_{2.5}Se_{0.5}$ sample prior to annealing. (**a**) shows the build direction, (**b**) shows the transverse direction, and (**c**) shows the scan direction. With respect to the sample geometry, the build direction is vertical, the transverse direction is horizontal, and the scan direction is into the page.*

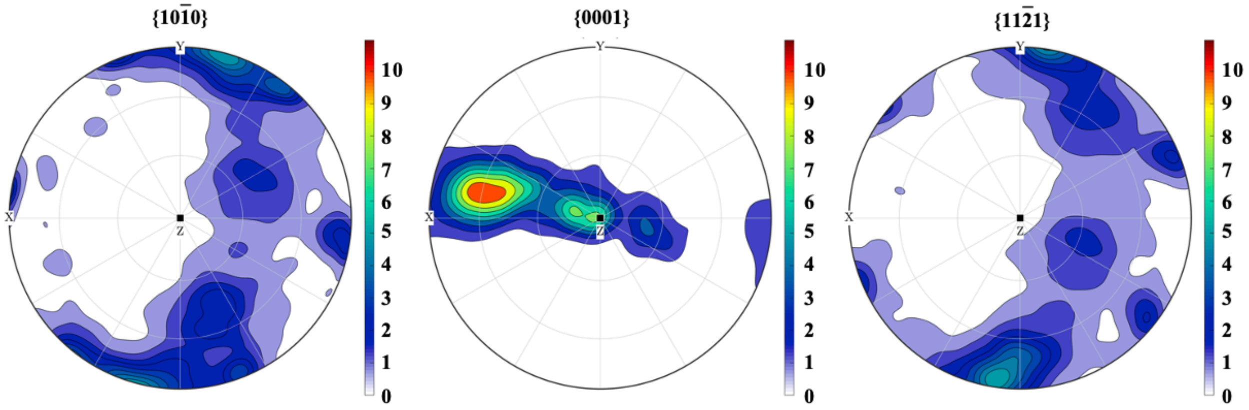

Figure 4-4. *Pole figures (PF) in the xy-plane for LPBF-built $Bi_2Te_{2.5}Se_{0.5}$ prior to annealing. The x-direction refers to the build direction, the y-direction refers to the transverse direction, and the z-direction refers to the scan direction.*

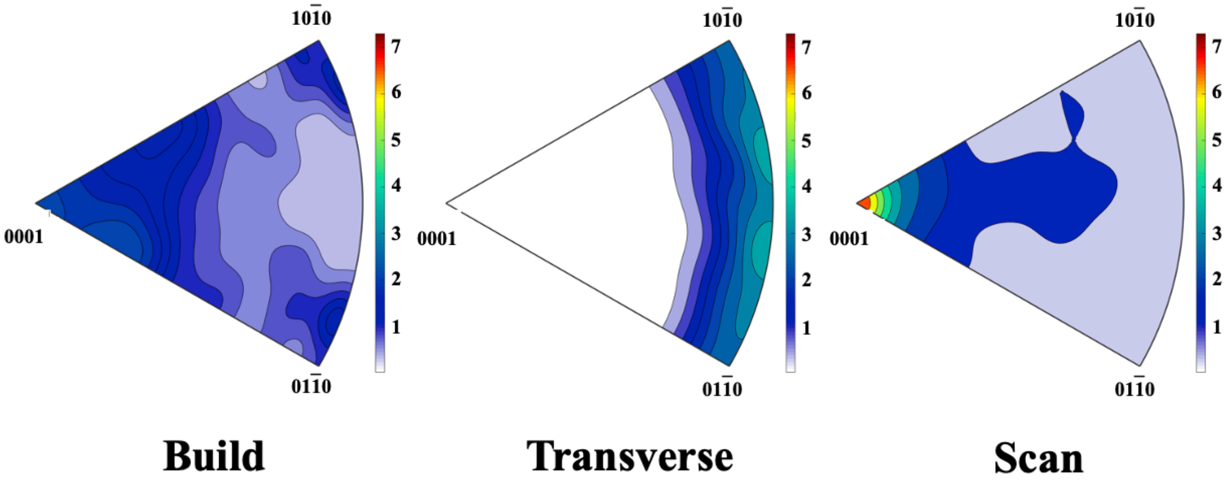

Figure 4-5. *Inverse pole figures (IPF) for LPBF-built $Bi_2Te_{2.5}Se_{0.5}$ prior to annealing.*

The strengths of the [0001] textures (alignment with the *c*-axis) were also quantified using the Kearns texture factor, where it was found that $F = 0.55$, 0.06, and 0.39 for the build, transverse, and scan directions, respectively. Based upon the EBSD data, the [0001] direction or *c*-axis is almost exclusively contained to the build and scan directions. This would indicate that the *c*-axis of the hexagonal $Bi_2Te_{2.5}Se_{0.5}$ crystal structure lies fixed in the plane formed by the build and scan directions resulting in a mixed texture for both. This reasonably agrees with prior literature on AM-built materials which found a strong alignment of the <0001> orientation for hexagonal materials along the maximum thermal gradient [143]. This also agrees with prior work on single crystal V_2VI_3 materials, where the c-axis is known to align parallel with the growth direction [136]. The EBSD crystallographic orientation maps in **Figure 4-3** also seem to indicate that the primary growth direction is initially in the build direction before eventually changing to the scan direction with increasing build layers and part height. However, further studies on this topic would need to be conducted to state so conclusively.

Perhaps most significantly though is that the $\{10\bar{1}0\}$ and $\{01\bar{1}0\}$ prismatic planes (perpendicular to the basal plane) are almost exclusively detected in the transverse direction with almost no c-axis alignment. As a result, the transverse direction lies almost entirely in the basal plane for these LPBF-built $Bi_2Te_{2.5}Se_{0.5}$ parts. Therefore, the expectation is that the transport properties (κ and σ) should be greater when measured in the transverse direction compared to the build and scan directions. To test this assertion, LPBF was used to fabricate several $Bi_2Te_{2.5}Se_{0.5}$ parts and their TE properties (S, κ, σ, and ZT) were then measured in both the transverse and build directions for comparison.

Another observation from the EBSD crystallographic orientation maps (**Figure 4-3**) is that the grains appear to be elongated in the transverse direction. As a result, phonons and electrons in the transverse direction are likely to encounter fewer grain boundaries than those traveling in the build direction. As discussed in Chapter 3, grain boundaries can act as scattering sites for both phonons and electrons, disrupting and reducing their mobilities [144–146]. As a result, this LPBF-produced grain structure may also further increase the anisotropy in transport properties between the build and transverse directions.

Lastly, it is believed that additional manipulation of the laser parameters could enhance the strength of the <0001> texture in the build direction, similar to previous studies on LPBF-built and bismuth telluride materials [28,35,36,99]. However, it is unlikely that this would meaningfully strengthen the almost completely prismatic plane texture observed in the transverse direction of these $Bi_2Te_{2.5}Se_{0.5}$ samples, where the enhanced and desired TE transport properties are expected. Therefore, further enhancement of the <0001> texture is left as a possibility for future work.

4.3.2 Transverse vs. Build Direction TE Properties

Following the RT TE property measurements, the expected differences in transport properties for the build and transverse directions were observed. Comparing the transverse direction to the build direction data in **Table 4-1**, the RT transport properties were enhanced by 24.9 % and 58.1 % for the κ and σ, respectively. Not only are these improvements aligned with expectations from prior works, but the fact that σ is more anisotropic and experienced a larger percent increase than κ also matches with previous experimental data [134–137].

Table 4-1. *RT TE property measurements conducted for the build and transverse direction LPBF-built* $Bi_2Te_{2.5}Se_{0.5}$ *samples prior to annealing. TE property measurement data is provided as the average ± standard deviation.*

RT Measurements (As-Built)	**S (µV/K)**	**κ (W/m*K)**	**σ (S/cm)**	**ZT**
As-Built Build	-75.1 ± 0.5	1.30 ± 0.02	263 ± 1.9	0.034 ± 0.001
As-Built Transverse	-63.8 ± 3.4	1.62 ± 0.03	416 ± 8.6	0.031 ± 0.003
Percent Change (%)	-15.0	24.9	58.1	-8.7

However, it is notable that the S does appear to be moderately anisotropic, having experienced a roughly 15.0 % decrease in the transverse direction compared to the build direction. The anisotropic S may be indicative of RT bipolar conduction effects resulting from the elevated point defect and charge carrier concentrations present in these as-built LPBF samples. As previously discussed and demonstrated in Chapter 3, the rapid solidification LPBF process generated a high, non-equilibrium concentration of charge carrier contributing point defects. Further, the positron annihilation data (**Figure 3-6**) identified a high concentration of cationic, bismuth vacancy defects (V_{Bi}''') that act as electron acceptors and each contribute three holes, the minority charge carrier for this n-type material. The resulting high carrier concentration was also experimentally proven using Hall measurements (**Figure 3-7**). Therefore, it is posited that the observed anisotropic S is a result of multicarrier effects caused by the high concentration of carrier contributing point defects in these as-built $Bi_2Te_{2.5}Se_{0.5}$ parts. The bipolar effects may also be responsible for the comparatively low S values achieved in these as-built LPBF $Bi_2Te_{2.5}Se_{0.5}$ samples. Comparisons to the annealed samples will be made to further validate these claims.

Meanwhile, the RT ZT was also found to be slightly anisotropic. A small 8.7 % reduction in the transverse direction was observed, which is attributed to the decrease in the magnitude of S, the squared term in the $ZT = \frac{\sigma S^2}{\kappa} T$ expression. This is nearly balanced by the disproportionately large increase in the transverse σ compared to the transverse κ, but ultimately a slight reduction in the transverse ZT is still observed. Overall, this data demonstrates that the LPBF process can produce $Bi_2Te_{2.5}Se_{0.5}$ parts with strong crystallographic textures that increase transport properties in the transverse direction and in the basal plane without a large sacrifice in TE efficiency.

4.3.3 Transverse vs. Build Direction TE Properties After Annealing

The impact of annealing on directionally dependent TE properties was also studied. First, transverse and build direction $Bi_2Te_{2.5}Se_{0.5}$ samples were annealed at 350 ºC for 24 hours and EBSD was once again used to study the resulting crystallographic orientations. These EBSD crystallographic orientation maps are shown in **Figure 4-6** and the EBSD data was used to produce the PF and IPF shown in **Figure 4-7** and **Figure 4-8**, respectively.

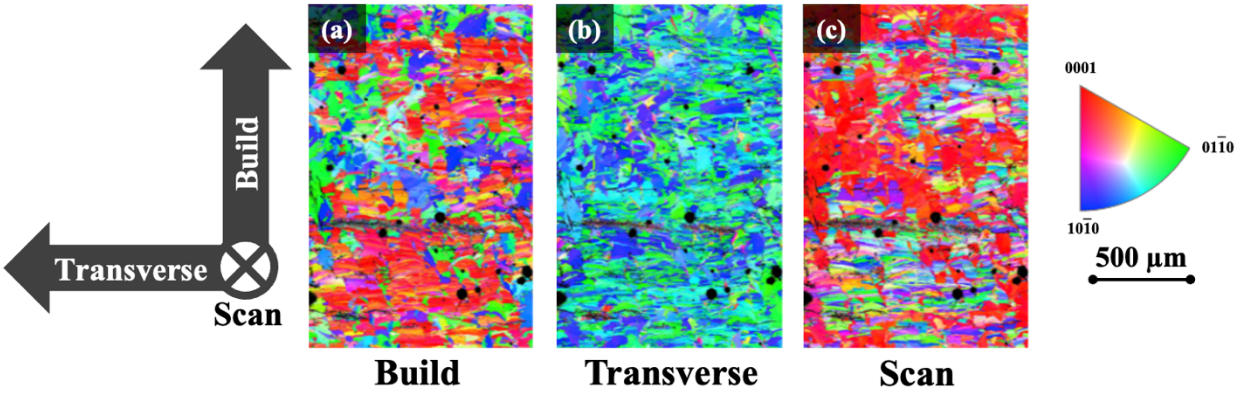

Figure 4-6. *EBSD crystallographic orientation map for a LPBF-built* $Bi_2Te_{2.5}Se_{0.5}$ *sample after annealing at 350 ºC for 24 hours. (**a**) shows the build direction, (**b**) shows the transverse direction, and (**c**) shows the scan direction. With respect to the sample geometry, the build direction is vertical, the transverse direction is horizontal, and the scan direction is into the page.*

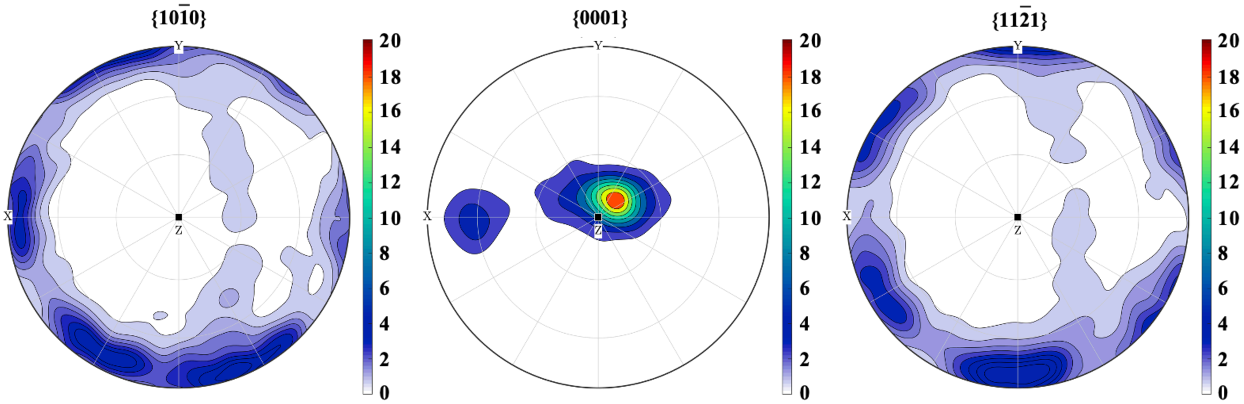

Figure 4-7. *Pole figures (PF) in the xy-plane for LPBF-built* $Bi_2Te_{2.5}Se_{0.5}$ *after annealing at 350 ºC for 24 hours. The x-direction refers to the build direction, the y-direction refers to the transverse direction, and the z-direction refers to the scan direction.*

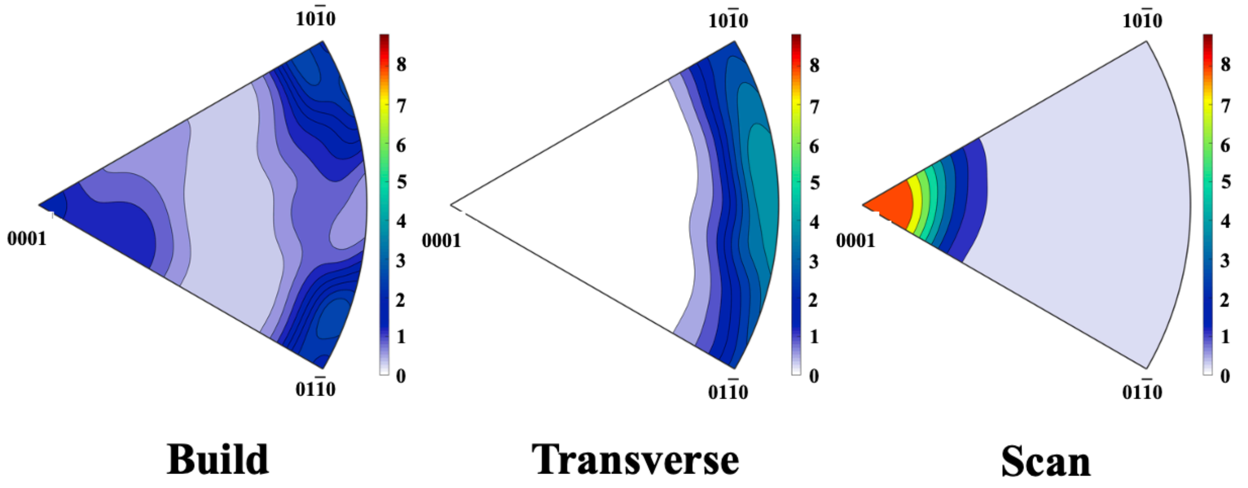

Figure 4-8. *Inverse pole figures (IPF) for LPBF-built $Bi_2Te_{2.5}Se_{0.5}$ after annealing at 350 ºC for 24 hours.*

The strengths of the [0001] textures (alignment with the *c*-axis) were quantified using the Kearns texture factor, where it was found that F = 0.42, 0.05, and 0.53 for the build, transverse, and scan directions, respectively. It is observed that the crystallographic textures prior to annealing are largely maintained after annealing. Therefore, the same claims about the preferred crystallographic orientations of LPBF-built $Bi_2Te_{2.5}Se_{0.5}$ remain true. The *c*-axis is isolated to the build and scan directions, meanwhile the transverse direction lies almost entirely in the basal plane. As a result, the same trends in TE properties are expected, where the transport properties are enhanced in the transverse direction compared to the build direction. The only notable difference is that, as discussed in *Section 3.3.1*, the grain size has increased from an average max Feret diameter of 14.0 μm^2 to 15.0 μm^2 after annealing. Once again, the unchanged texture provides evidence that recrystallization has not occurred at these annealing conditions, similar to the results of Hu *et al.* [99].

When comparing the RT TE property measurements between the build and transverse directions shown in **Table 4-2** for the annealed samples, it is confirmed that the same expected transport property trends are observed. Even after annealing, the κ and σ are enhanced by 13.1 %

and 38.9 % in the transverse direction, respectively. Additionally, a larger σ anisotropy is still observed compared to the κ. However, it is noted that these disparities are smaller in their percent changes than those measured prior to annealing.

Table 4-2. *RT TE property measurements conducted for the build and transverse direction LPBF-built $Bi_2Te_{2.5}Se_{0.5}$ samples after annealing at 350 ºC for 24 hours. TE property measurement data is provided as the average ± standard deviation.*

RT Measurements (Annealed)	***S*** **(μV/K)**	$\boldsymbol{\kappa}$ **(W/m*K)**	$\boldsymbol{\sigma}$ **(S/cm)**	***ZT***
Annealed Build	-199 ± 0.4	1.17 ± 0.02	352 ± 3.5	0.352 ± 0.012
Annealed Transverse	-199 ± 4.0	1.32 ± 0.04	489 ± 23	0.431 ± 0.039
Percent Change (%)	-0.16	13.1	38.9	22.5

At the same time, the anisotropic behavior observed in the *S* of the as-built samples (**Table 4-1**) has been almost completely removed by the annealing process. It is argued that the annealing-induced reductions in point defect and charge carrier concentrations (discussed in *Section 3.3.1*) have eliminated the RT bipolar effects that caused the previously observed *S* anisotropy. As a result, the typically expected isotropic *S* is restored [137]. It is also noted that the magnitude of the *S* increased substantially in both directions after annealing, which can be attributed to the decrease in carrier concentration (*Section 3.3.3*) and the corresponding removal of RT multicarrier effects. Additionally, after annealing it is measured that the *ZT* has become more strongly anisotropic and is now enhanced by roughly 22.5 % in the transverse direction. This anisotropy in TE efficiency ($ZT = \frac{\sigma S^2}{\kappa} T$) is attributed to the disproportionally larger anisotropy and increase in the σ compared to the κ. Therefore, it is demonstrated that annealing provides a post-processing pathway by which both the transport properties and the *ZT* can be intentionally improved in the transverse direction of LPBF-built $Bi_2Te_{2.5}Se_{0.5}$ parts.

Finally, in the interest of completionism, the RT TE properties both before and after annealing are compared for the build direction samples, similar to the work done with the transverse direction samples in Chapter 3. The as-built and annealed RT TE properties are provided and compared for the build direction samples $Bi_2Te_{2.5}Se_{0.5}$ in **Table 4-3**. The as-built and annealed RT TE properties for the transverse direction samples originally provided in **Table 3-3** are re-produced in **Table 4-3** for comparison.

Table 4-3. *RT TE property measurements conducted for the build and transverse direction LPBF-built* $Bi_2Te_{2.5}Se_{0.5}$ *samples both as-built and after annealing at 350 ºC for 24 hours. TE property measurement data is provided as the average ± standard deviation.*

RT Measurements (As-Built vs. Annealed)	**S (µV/K)**	**κ (W/m*K)**	**σ (S/cm)**	**ZT**
As-Built Build	-75.1 ± 0.5	1.30 ± 0.02	263 ± 1.9	0.034 ± 0.001
Annealed Build	-199 ± 0.4	1.17 ± 0.02	352 ± 3.5	0.352 ± 0.012
Percent Change (%)	165	-9.80	33.8	944
As-Built Transverse	-63.8 ± 3.4	1.62 ± 0.03	416 ± 8.6	0.031 ± 0.003
Annealed Transverse	-199 ± 4.0	1.32 ± 0.04	489 ± 23	0.431 ± 0.039
Percent Change (%)	212	-18.4	17.5	1300

It is evident that the same trends as previously observed and discussed for the transverse direction samples remain true for the build direction samples after annealing: the Seebeck coefficient (S) has increased in magnitude, the thermal conductivity (κ) has decreased, the electrical conductivity (σ) has increased, and the thermoelectric figure of merit (ZT) has increased dramatically. It is therefore argued that the same posited mechanisms discussed in Chapter 3 are applicable and can also explain the observed changes in the RT TE properties in the build directions of these LPBF-built $Bi_2Te_{2.5}Se_{0.5}$ parts. Additionally, the fact that these annealing-induced TE property trends are largely unaffected by the sample orientation indicates that the previously proposed mechanisms are not dependent upon the crystallographic texture.

However, it should be noted that even though the overarching trends in TE property enhancement may not depend upon the crystallographic orientations, the magnitude of these changes might. Larger percent increases are observed in all of the transverse TE properties after annealing except for the σ, which still achieved higher values but a smaller percent change. While interactions with the grain boundaries are likely a dominant contributor, a proper explanation for this phenomenon is not yet known and remains a possibility for future study.

4.4 Conclusions

This work demonstrates the ability of LPBF to fabricate $Bi_2Te_{2.5}Se_{0.5}$ parts with strong and intentional crystallographic textures. EBSD data provided significant evidence that the *c*-axis of the $Bi_2Te_{2.5}Se_{0.5}$ crystal remained in the build-scan plane, while the perpendicular transverse direction was almost entirely within the basal plane. Additionally, it was demonstrated that these aspects of the texture were preserved after annealing at 350 ºC for 24 hours. RT TE property measurements showed that the transport properties (κ and σ) were enhanced in the transverse direction due to these LPBF-produced textures and that this enhancement was maintained after annealing as well.

Further, it has been demonstrated that the Seebeck coefficient (S) anisotropy can be removed by annealing. This is explained by the results and mechanisms discussed in Chapter 3, where the annealing-induced reduction in carrier contributing point defects and minority charge carriers eliminated the RT bipolar conduction effects that caused the anisotropic S. Lastly, annealing was also shown to have enhanced the thermoelectric figure of merit (ZT) along the transverse direction in the basal plane owing to the greater anisotropy of the σ compared to the κ.

Therefore, it is concluded that LPBF is a viable technique for building TE $Bi_2Te_{2.5}Se_{0.5}$ samples with directionally enhanced transport properties via intentionally developed crystallographic textures. Further, annealing can be used as a post-processing technique to both effectively increase the transport properties and enhance the TE efficiency in the basal plane and transverse direction.

4.5 Recommendations for Future Work

So far, crystallographic orientation control and directional TE properties have only been demonstrated in bulk, LPBF-built $Bi_2Te_{2.5}Se_{0.5}$ parts constructed using a singular scan and processing strategy. While this work demonstrates the ability to produce directionally dependent TE properties through LPBF-produced crystallographic textures, the LPBF construction of bismuth telluride parts with site-specific crystallographic orientation control has not yet been explored and has only been demonstrated in a limited number of materials. For future work, it would be interesting to study the ability of LPBF to create intentionally varied, site-specific crystallographic orientations within a single part by transitioning between different solidification regimes through alterations to the laser parameters and the scan strategy, similar to the work conducted by DeHoff *et al.* [34] and shown in **Figure 4-1**. In doing so, it may be possible to create channels of increased transport properties within a LPBF-built part.

To study this capability, spatial thermal and electrical transport measurements with a high resolution would need to be utilized to create maps and visualize the dimensionally varied transport properties within a single part. Unfortunately, this is outside of the capabilities and scope of the current work, where only bulk TE property measurements were performed.

Chapter 5. The Alteration of Charge Carrier Type and Concentration via Process Parameter Manipulation in LPBF

5.1 Introduction

5.1.1 Compositional Control of Charge Carriers in V_2VI_3 Materials

In *Section 3.1.1*, the role of vacancy and antisite point defects in V_2VI_3 materials was discussed using Bi_2Te_3 as a representative example. Anionic vacancies ($V_{Te}^{\cdot\cdot}$) and antisite ($Te_{Bi}^{\cdot}$) defects can act as electron donors and promote n-type character. Alternatively, cationic vacancies ($V_{Bi}^{'''}$) and antisite ($Bi_{Te}^{'}$) defects will act as electron acceptors and promote p-type character [27]. Examples of these intrinsic point defects in a representative bismuth telluride system are shown in **Figure 3-1** and a summary of their charge carrier contributions are provided in **Table 3-1**. Ultimately, when creating V_2VI_3 compounds for use as TE materials, the charge carrier type and concentration are often intentionally manipulated through the preferential formation and concentration of these specific carrier contributing point defects. One of the most common methods of controlling point defect chemistry in V_2VI_3 materials is through modifications to the starting composition [27].

The binary bismuth-tellurium phase diagram (**Figure 5-1**) has a solubility range in the region around the bismuth telluride stoichiometric composition, Bi_2Te_3 [147]. Prior studies have determined that this is facilitated by the formation of antisite defects, where an excess of bismuth is accommodated by sitting on empty tellurium atom sites ($Bi_{Te}^{'}$), or vice-versa ($Te_{Bi}^{\cdot}$) [148]. In short, a cation-rich environment can be used to facilitate cationic antisite defects and therefore increase the hole concentration and p-type character. In contrast, anion-rich environments favor anionic antisite defects and increase the free electron concentration and n-type character. These relationships are applicable to all binary V_2VI_3 compounds.

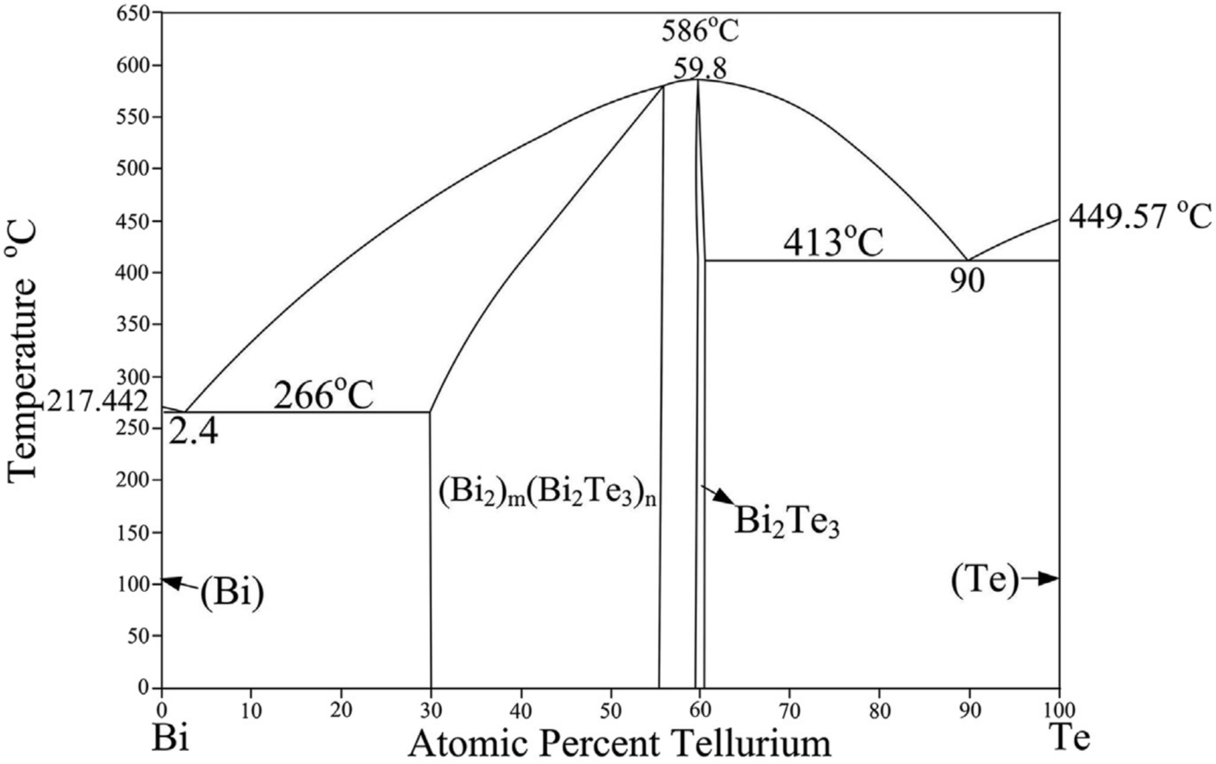

Figure 5-1. *Binary bismuth-tellurium phase diagram* [147].

Researchers have also determined another means of compositionally controlling the intrinsic point defect and charge carrier concentrations known as the (χ, r)-model. This model posits that the smaller the differences in the electronegativities (χ) and covalent radii (r) are between the cations and anions, the lower the cation antisite defect formation energy (E_{AS}) will be. Specifically, this refers to the substitution of a cationic Group V element (Bi or Sb) onto an anionic Group VI element (Te, Se, or S) lattice site to form electron accepting point defects (*e.g.*, Bi'_{Te}, Sb'_{Se}). This can be attributed to the fact that more chemically and physically similar atoms will be able to substitute into each other's lattice sites more easily. In contrast, the greater the difference in χ and r between the cations and anions, the lower the anionic vacancy formation energy (E_V) will be, meaning the creation of electron donating Te, Se, and/or S vacancies (*e.g.*, $V_{Te}^{\cdot\cdot}$, $V_{Se}^{\cdot\cdot}$) will be enhanced [27,75]. These relationships can be enumerated for V_2VI_3 compounds through the following trends:

$$E_{AS}(\text{Sb-Te}) < E_{AS}(\text{Bi-Te}) < E_{AS}(\text{Sb-Se}) < E_{AS}(\text{Bi-Se}) < E_{AS}(\text{Bi-S})$$

$$E_{V}(\text{Sb-Te}) > E_{V}(\text{Bi-Te}) > E_{V}(\text{Sb-Se}) > E_{V}(\text{Bi-Se}) > E_{V}(\text{Bi-S})$$

Notably, these trends present an inverse relationship, where increasing the difference between χ and r will inhibit the formation of cation antisite defects, while aiding the formation of anionic vacancies and enhancing n-type character, and vice-versa. This (χ, r)-model can be applied to binary, ternary, and quaternary V_2VI_3 materials for charge carrier type and concentration control. For example, the hole concentration of $Bi_{2-x}Sb_xTe_3$ can be increased by increasing the Sb content and therefore lowering the formation energy of the electron accepting cationic antisite defects [27,149]. For low temperature applications, one of the most common and efficient p-type TE materials is $Bi_{0.3}Sb_{1.7}Te_3$, while one of the most efficient n-type TE materials is $Bi_2Te_{2.3}Se_{0.7}$ [75]. Therefore, prior work with traditionally manufactured TE V_2VI_3 materials has demonstrated that composition can be used as both an effective predictor and driver of a material's charge carrier type and concentration.

Lastly, the Seebeck coefficient (S) can be used as an indicator of the dominant charge carrier type and changes to the carrier concentration for TE V_2VI_3 materials. As previously discussed in *Section 3.3.3*, it is known that a positive S value indicates a p-type character and hole dominated transport, while a negative S value indicates an n-type character and that electrons are the dominant charge carrier. The S is also inversely proportional to the carrier concentration (n) by $|S| \sim n^{-\frac{2}{3}}$, and so changes to the magnitude of S are also indicative of changes to the carrier concentration in a semiconducting material [86,131,132].

5.1.2 Impact of Oxides on the Seebeck Coefficient of Bismuth Telluride Compounds

While the pre-synthesis composition of the starting material is frequently used as a means of controlling point defect and charge carrier formation, research has also indicated the importance of the processing method itself on the carrier concentration and S of V_2VI_3 materials. Several works have emphasized the role and significance of oxide inclusions as major contributors to the increased and preferential formation of carrier contributing point defects in bismuth telluride materials. However, the exact influence and mechanism of these oxides is not yet well understood or agreed upon.

Welch *et al.* [28] recently studied the formation and impact of nano- and micro-structures in a LPBF-built, selenium-doped bismuth telluride material. The starting powder had a composition of $Bi_2Te_{2.7}Se_{0.3}$, which is conventionally n-type as discussed in *Section 5.1.1*. However, following LPBF fabrication, Welch *et al.* found that these $Bi_2Te_{2.7}Se_{0.3}$ samples were strongly p-type with a positive, maximum S of 143 μV/K at 95 ºC. For comparison, a melt grown sample was also prepared from the same starting material and a maximum S of -210 μV/K at 94.3 ºC was achieved, indicating an n-type behavior. Therefore, it was observed that the LPBF process triggered a conversion to p-type character from this n-type starting composition, indicating a change in the primary charge carrier from electrons to holes.

This shift in semiconducting character was attributed to the presence of both nanoscale, bismuth-rich oxide inclusions and tellurium-rich eutectic features. It was posited that these features resulted in a bismuth depletion of the matrix that produced bismuth vacancies (V_{Bi}''') and a tellurium depletion that produced bismuth antisite (Bi_{Te}') defects. As previously discussed, cationic vacancy and antisite point defects act as electron acceptors and present a possible mechanism by which bismuth and tellurium redistribution can produce the observed n-type to p-type transition via LPBF. A similar p-type character has also previously been reported by Zhang *et al.* [31], who used LPBF to successfully fabricate Bi_2Te_3 samples with positive Seebeck coefficient values ranging from 85 μV/K to 189 μV/K.

However, more recent work conducted by Liu *et al.* [150] tells a contrasting story about the impact of oxide formation on the charge carriers of a Bi_2Te_3 polycrystalline material. In their work, a Bi_2Te_3 ingot was ball milled and then hot pressed both in an argon environment and an oxygen-rich environment. When prepared in a high-purity argon environment, it was found that the samples remained p-type and the majority hole concentration was stable across all processing stages. However, when exposed to oxygen during ball milling and/or loading, the Bi_2Te_3 samples became n-type with increasing electron concentrations. Through a combination of electron probe microanalyzation (EPMA), XRD, and transmission electron microscopy (TEM), it was shown that the introduction of oxygen into the processing environment resulted in the formation of bismuth-rich Bi_2TeO_5 nanoscale oxide inclusions. Density functional theory (DFT) calculations found that the most energetically favorable point defect changed from electron accepting bismuth antisite (Bi_{Te}') defects to electron donating tellurium antisite $(Te_{Bi}^{\cdot})$ defects in the presence of this oxygen-induced Bi_2TeO_5 phase. Therefore, in contrast to the conclusions of Welch *et al.*, Liu *et al.* argued that the formation of bismuth-rich nanoscale oxides produced a tellurium-rich matrix that promoted the increased formation of electron donating point defects instead, which explains their observed transition from p-type to n-type character.

The influence of these oxide inclusions on bismuth telluride semiconducting behavior is not yet well understood, with both proposed explanations and experimental observations of n-type to p-type conversions and vice-versa. However, their potential impact on the local chemical environment emphasizes that considerations of these oxide inclusions are crucial during the LPBF process, where the increased surface area of the fine powders may have resulted in increased oxidation of the starting material. Additionally, the SLM®125 LPBF chamber used to fabricate the $Bi_2Te_{2.7}Se_{0.3}$ samples for this work had a maximum oxygen content cutoff value of only 1,000 ppm. While samples were typically built at lower oxygen contents closer to 10 – 100 ppm, the consequence is still that oxide inclusion formation is probable in these LPBF-built parts and that their impact needs to be contemplated.

5.2 Methods

5.2.1 Sample Fabrication and Starting Powder

The majority of the bismuth telluride samples discussed in this chapter were constructed using the same starting powder and build strategy as the three-dimensional, rectangular bar samples shown and studied in Chapter 2, similar to those shown in the SEM micrographs in **Figure 2-10**. The starting powder is a ball milled $Bi_2Te_{2.7}Se_{0.3}$, the same one discussed in *Section 2.2.1*. The XRD pattern for this powder is provided in **Figure 2-2** and an SEM micrograph is shown in **Figure 2-3**. As explained in *Section 2.2.3*, these LPBF-built samples were fabricated using a manual process that involved leveling the powder by hand in an argon-filled, SLM®125 chamber. Through this process, rectangular bars of $Bi_2Te_{2.7}Se_{0.3}$ were built with dimensions of approximately 6 mm long x 2 mm wide x 1.1 mm tall using a scan strategy where the laser line scans were unidirectional and parallel to the long axis of the samples without rotation between layers.

These rectangular $Bi_2Te_{2.7}Se_{0.3}$ bars are referred to as high throughput samples due to the capability of this process to produce multiple parts at a time with different processing strategies (laser power (p), scan speed (v), hatch spacing (h)), except for the layer thickness (t) which was kept at 75 µm for all samples. Additionally, these samples were left attached to their p-type bismuth antimony telluride substrate during Seebeck coefficient (*S*) and porosity measurements. These *S* measurements were taken parallel to the long axis and scan direction of the high throughput samples using a surface probe technique that avoided interactions with the attached substrate and adjacent samples. This *S* measurement process is discussed in more depth in the following *Section 5.2.2*. The porosity measurement system is identical to the one explained previously in *Section 2.2.3* and is reiterated in *Section 5.2.3*. In total, 35 high throughput samples were constructed and their LPBF processing parameters are provided in **Table 5-1** in the Appendix, along with their *S* and average porosity percentage values. An example of one of these high throughput $Bi_2Te_{2.7}Se_{0.3}$ samples is shown in **Figure 5-2**.

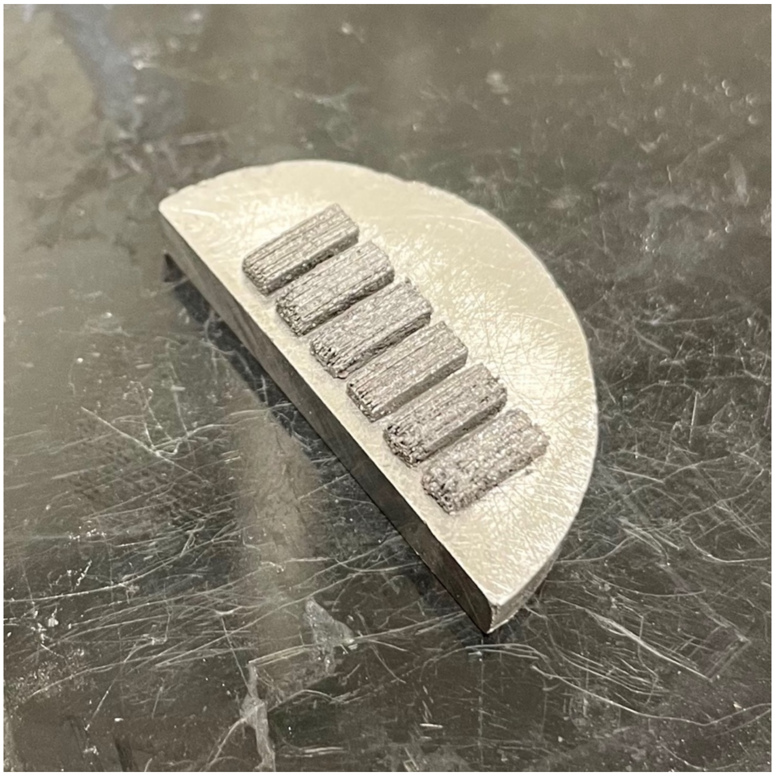

Figure 5-2. *High-throughput, LPBF-built* $Bi_2Te_{2.7}Se_{0.3}$ *samples attached to a p-type bismuth antimony telluride substrate. The rectangular bar samples had dimensions of roughly 6 mm x 2 mm x 1.1 mm.*

Additional bismuth telluride samples were also constructed for the sole purpose of wavelength dispersive spectroscopy (WDS) composition measurements. These samples were fabricated using LPBF by Open Additive from a Bi_2Te_3 starting composition. Their build process was very similar to the ternary $Bi_2Te_{2.7}Se_{0.3}$ samples, except that an automated powder leveling system was employed and the laser scans were bidirectional, meaning that they alternated and returned in the opposite direction after every line scan. Additionally, a larger, consistent layer thickness of 150 μm was used to fabricate these Bi_2Te_3 samples. Otherwise, a parallel line scan strategy was still employed along the long axis and without rotation between layers. Final part geometries were rectangular prisms with approximate dimensions of 4 mm x 4 mm x 10 mm and were removed from their substrates. In total, four of these samples were constructed and their compositions measured using WDS. A different, bulk Seebeck coefficient measurement process was also carried out parallel to the long axis and scan direction for these samples using the Linseis LSR-3 system described further in the following *Section 5.2.2*.

5.2.2 Seebeck Coefficient (S) Measurements

RT Seebeck coefficient (S) measurements for the high throughput $Bi_2Te_{2.7}Se_{0.3}$ samples (**Figure 5-2**) were carried out using a surface probe technique at the National Institute of Standards and Technology (NIST). These measurements utilized the quasi-steady state condition of the differential method in an upgraded version of the custom-built thermoelectric property screening instrument previously developed by Yan *et al*. [151]. The Seebeck coefficient is given by $S(T_o) = \frac{V}{\Delta T}$, where V is the thermoelectric voltage, ΔT is the temperature difference between the measurement probes, and T_o is the average sample temperature [152]. Two type R thermocouple probes were pressed onto the sample surface and independently supported in spring-loaded alumina tubes for structural stability. The thermocouples were spatially separated 3 mm center to center and the contacting surface of each thermocouple bead was flattened to a 0.8 mm diameter circular face to improve thermal contact with the sample surface [153]. A bifilar heater coil enclosing one of the thermocouple probes is used to generate a local temperature difference (ΔT) by applying a small current. Heat flows into the sample through the hot thermocouple and the temperature difference increases with time.

Since the temperature difference is quasi-steady-state, three separate bus triggered Keithley 2182A nanovoltmeters were used to eliminate correspondence distortion by simultaneously measuring the thermoelectric voltage and the two thermocouple temperatures [153]. The thermoelectric voltage, measured between the platinum lead wires of the type R thermocouples, and the temperature of each thermocouple were recorded at five intervals between ≈1 K and ≈3 K. The S is calculated as the slope of the unconstrained linear fit of these V and T differences. The measured S is then subtracted from the absolute S of the platinum reference wires to obtain the corrected S of the sample. The S measurement uncertainty (one standard deviation) is ± 6.5 %. A representative diagram of these surface probe S measurements is provided in **Figure 5-3**.

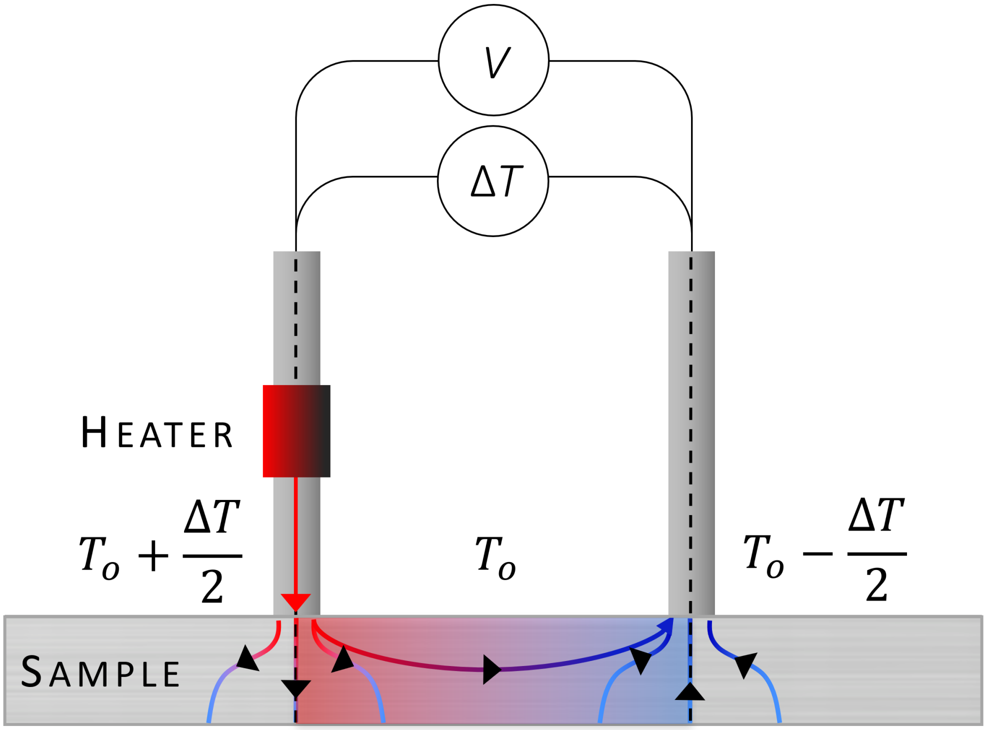

Figure 5-3. *Representative diagram of the Seebeck coefficient (S) surface probe measurement system.*

The advantages of this surface probe S measurement system are that it is a nondestructive technique and can be used to conduct high throughput S measurements in rapid succession. Additionally, the low interaction volume associated with this procedure meant that RT S measurements could be taken without influence from the attached substrate or adjacent samples. Images showing the high throughput samples during S measurement are provided in **Figure 5-4**. The third probe visible in these images can be used to conduct electrical resistivity measurements, but required a surface quality that many of these high throughput samples did not satisfy.

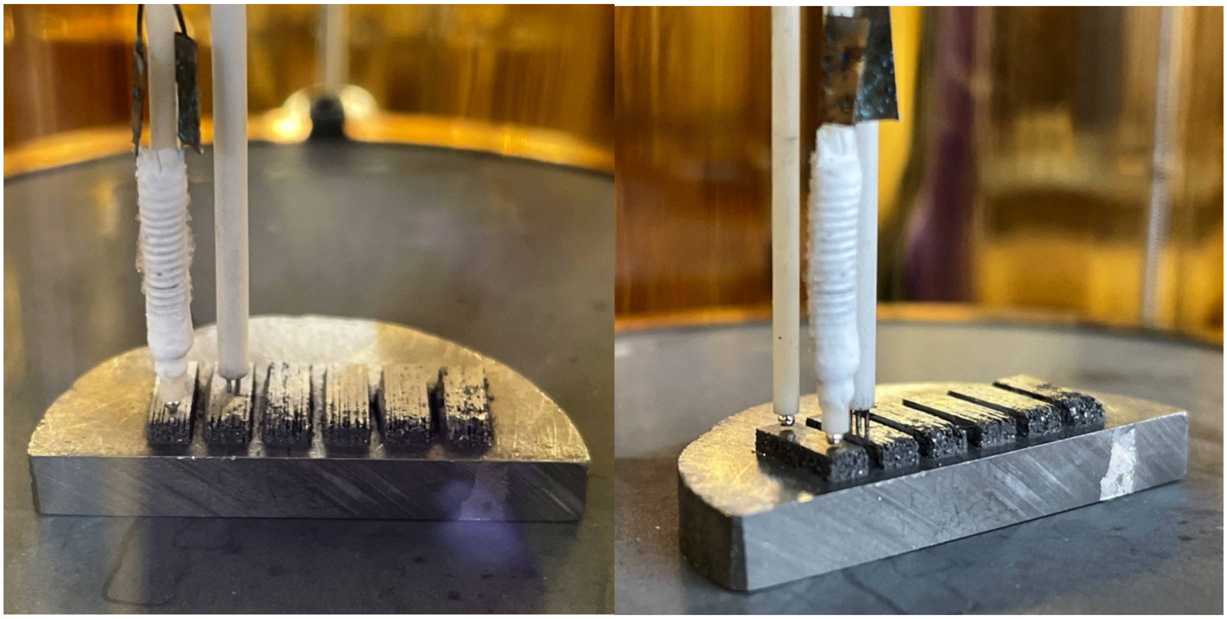

Figure 5-4. *High throughput, LPBF-built* $Bi_2Te_{2.7}Se_{0.3}$ *samples undergoing RT Seebeck coefficient (S) measurements using a surface probe technique. Measurements were taken long the long axes and parallel scan directions of these samples.*

S measurements for the 4 mm x 4 mm x 10 mm Bi_2Te_3 samples constructed by Open Additive were conducted using a bulk measurement technique in a Linseis LSR-3 system, similar to the S measurement technique previously discussed in *Section 3.2.2*. For these measurements, heaters are attached to both ends of a sample's long axis while two voltage probes are attached at a measured distance apart in the middle of the sample. These measurements are also conducted inside of a furnace to set the environmental temperature. Eventually, the two heaters at either end of the sample are elevated to different temperatures to create a predetermined thermal gradient ($\Delta T = T_{hot} - T_{cold}$). The voltage probes then measure the resulting thermovoltage (V_{th}). Correspondingly, the S can be measured as $S = -\frac{V_{th}}{\Delta T}$. These measurements are performed for three thermal gradients and three S are collected at each environmental (or furnace) temperature. The slope is then taken from the linear regression of these three points to calculate the average S at that environmental temperature. The uncertainty is calculated from the diagonal of the covariance matrix for the linear regression and was found to be very low (less than 1 μV/K) at RT for the four characterized samples. The uncertainties associated with these *S* measurements are visualized as error bars in the relevant figures.

5.2.3 Porosity Measurements

The relative densities of all 35 high throughput samples were assessed by measuring their porosity fractions through a process identical to the one previously described in *Section 2.2.3*. First, high throughput samples were cross-sectioned and polished perpendicular to their laser scan directions and long axes while still attached to their substrate. Then, SEM micrographs were collected. The porosity fraction of these cross-sections was measured based upon contrast using ImageJ, where the pores appeared either brighter at their borders due to charging from the electron beam or darker due to their depth when compared to the flat, dense surface. These measurements were conducted across three cross-sections for each sample and the resulting average porosity percentage data can be found in **Table 5-1** in the Appendix. Examples of these contrast-based porosity measurements can be found in **Figure 2-5**.

5.2.4 Micro X-Ray Fluorescence (μXRF) and Wavelength Dispersive Spectroscopy (WDS)

Composition measurements were carried out on these samples using one of two different techniques: micro X-ray fluorescence (μXRF) and wavelength dispersive spectroscopy (WDS). μXRF was used to conduct composition measurements for six LPBF-built, $Bi_2Te_{2.7}Se_{0.3}$ bars from a single high throughput sample batch. XRF is a technique that utilizes high energy X-rays to eject an inner shell electron from a sample of interest. Then, an electron from one of the atom's higher energy electron shells moves to the vacant spot in the lower energy shell. This difference in energy is released as a characteristic fluorescent X-ray that is unique to an element based upon the energy difference between the relaxed electron's initial and final orbital shells. As a result, the outgoing, detected X-rays can be used to both identify and quantify the elements present in a sample. XRF has the advantage of being nondestructive and µXRF specifically makes use of a small spot size (20 µm) to gather composition information with a reasonably high spatial resolution. Multiple µXRF point measurements were collected across the top surfaces of each high throughput rectangular bar sample. These multiple compositions measurements were then used to calculate the average bismuth, tellurium, and selenium compositions and standard deviations for each sample.

WDS was also used to characterize the compositions of the four Bi_2Te_3 rectangular prism samples built by Open Additive. The fundamental mechanics of WDS are very similar to XRF, with the only significant difference being that an electron beam (typically in an SEM) is used to eject the inner shell electrons instead of high energy X-rays. Compared to the similar energy-dispersive X-ray spectroscopy (EDS) technique, WDS uses X-ray diffraction to separate the characteristic X-rays by their wavelengths instead of their energies. WDS not only shares the advantage of being nondestructive, but also has a very small, variable spot size (1 to 30 µm) that can be used to isolate or avoid specific microstructural features and phases during composition analysis. WDS composition point measurements were collected at the centers of the Bi_2Te_3 samples after being cross-sectioned and polished perpendicular to their long axes/laser scan directions. Lastly, this WDS technique was conducted with a Bi_2Te_3 standard of known composition, which yielded low uncertainty values of ± 0.17 at% and ± 0.39 at% for the tellurium and bismuth contents, respectively. The uncertainties associated with the WDS and µXRF composition measurements are visualized using error bars in the relevant figures.

5.3 Results and Discussion

5.3.1 Seebeck Coefficient Variation Throughout the Processing Parameter Space

Despite creating all the high throughput samples from the same $Bi_2Te_{2.7}Se_{0.3}$ starting powder, parts could be produced with Seebeck coefficients (S) that not only varied in their magnitudes, but also varied in their signs through alterations to the processing parameters. While a similar n-type to p-type conversion was reported by Welch *et al.* [28], this observation is notable because the dominant and most energetically favorable point defects for $Bi_2Te_{2.7}Se_{0.3}$ should be electron donating anionic vacancies ($V_{Te}^{\cdot\cdot}$ and $V_{Se}^{\cdot\cdot}$), which promote n-type character [27]. In other words, variations to the LPBF processing strategy were found to manipulate the concentrations and dominant transport of electrons and holes to produce parts with a wide range of positive or negative S values.

To better understand and predict the impacts of the LPBF processing parameters on the S values of these parts, an iterative augmented machine learning (ML) process was once again employed, similar to the system used in Chapter 2 and explained in *Section 2.2.4*. However, for this application, the output ML predictions were the RT S instead of the melt pool dimensions. The only other major change is that in addition to laser power (p) and scan speed (v), hatch spacing (h) was introduced as a third variable to fully model the processing parameter space for these three-dimensional $Bi_2Te_{2.7}Se_{0.3}$ samples. The layer thickness (t) was held constant at 75 µm for all the LPBF-built, high throughput parts.

An iterative process of experimental data input and ML predictions was used to generate an ML predictive model for the value of S with changing process parameters. A high throughput system of sample fabrication and characterization allowed for the simultaneous construction of six $Bi_2Te_{2.7}Se_{0.3}$ samples at one time (**Figure 5-2**) followed by rapid RT S measurements (**Figure 5-3** and **Figure 5-4**). Each round of experimental data was used to educate the ML model. The ML predictions and associated uncertainties were visualized using heat maps, which were then used to determine the next set of experimental data points. In the end, a total of 35 high throughput samples were built using LPBF. Their *S* and average porosity percentages were measured, and the full data set is provided in **Table 5-1** in the Appendix. The final ML-predicted RT *S* map and associated uncertainty map are provided in **Figure 5-5** and **Figure 5-6**, respectively. It should be noted that while the ML model is three-dimensional, the following figures are provided at a constant h = 100 µm value so that two-dimensional maps with variable p and v are shown.

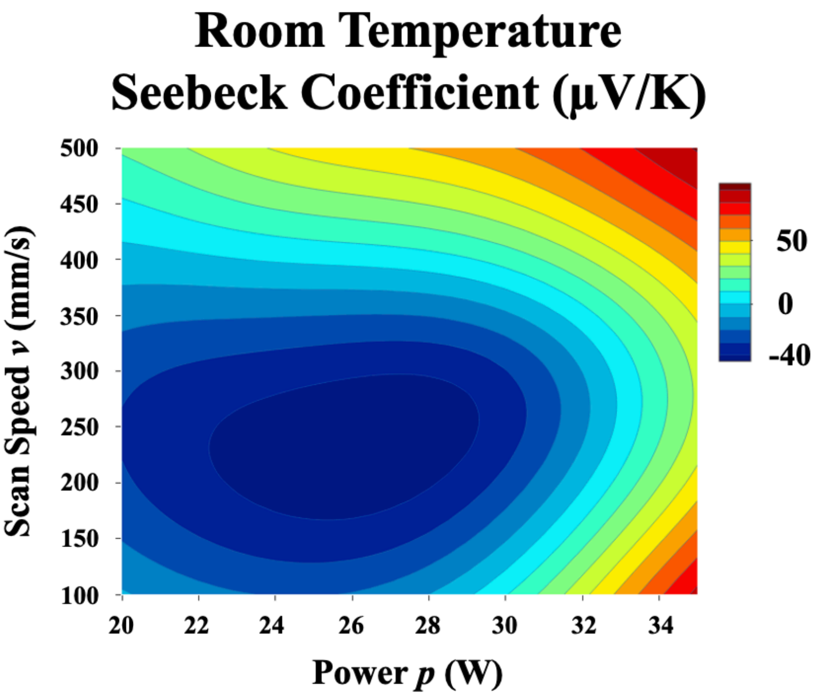

Figure 5-5. *ML-predicted map of RT Seebeck coefficient (S) within the LPBF processing parameter space (p vs. v). All samples were constructed from a* $Bi_2Te_{2.7}Se_{0.3}$ *starting powder. The hatch spacing (h) is held constant at 100 µm.*

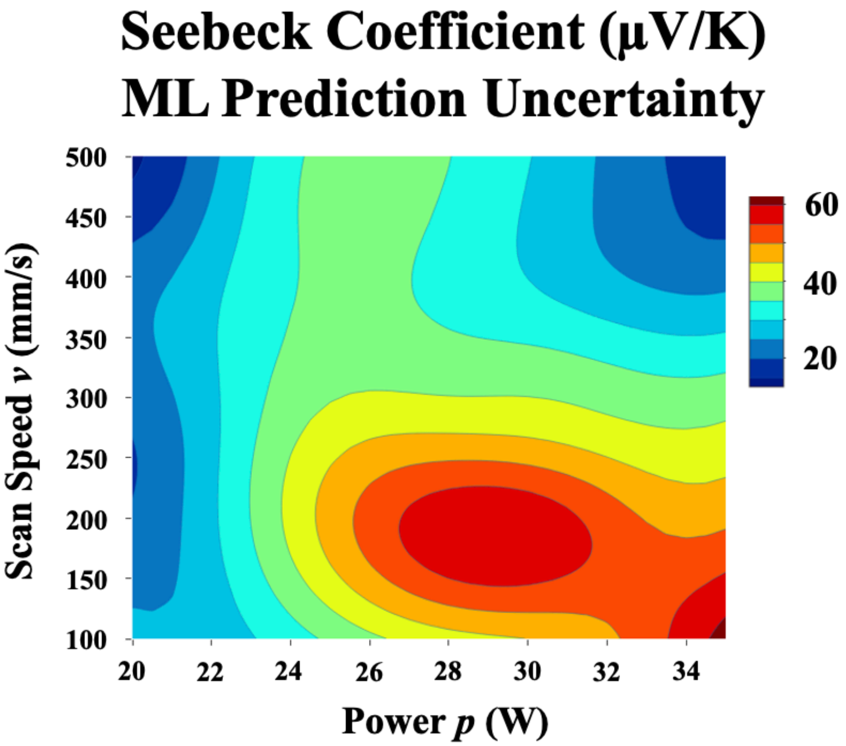

Figure 5-6. *ML-predicted uncertainty map of RT Seebeck coefficient (S) within the LPBF processing parameter space (p vs. v). All samples were constructed from a* $Bi_2Te_{2.7}Se_{0.3}$ *starting powder. The hatch spacing (h) is held constant at 100 µm.*

Upon inspection of the ML-predicted RT *S* map, it is noted that changes to the LPBF processing parameters effectively altered both the sign and magnitude of the *S* to create either n-type or p-type samples from the $Bi_2Te_{2.7}Se_{0.3}$ starting powder. This LPBF-enabled ability to create both n-type and p-type parts during the same build process and from the same starting powder has the potential to enable a manufacturing process in which the n-type and p-type legs can be simultaneously fabricated directly onto the electrical shunts of a TE module, beneficially reducing the manufacturing time. However, to effectively produce TE parts with intentional semiconducting behaviors, the mechanisms and relationships that are producing these variations in charge carrier type must be understood. Therefore, further work on understanding how the LPBF process is affecting the $Bi_2Te_{2.7}Se_{0.3}$ material properties and therefore yielding these *S* values is highly motivated.

It should be acknowledged that the uncertainty values are very large in some areas of the map shown in **Figure 5-6**, even reaching as high as ± 60 μV/K. It is known that the repeatability of AM-built parts and properties is a pervasive issue in the field that can be exacerbated for specific processing parameter combinations [154–157], although this problem is outside the scope of this work. As a result, the following discussions comparing material properties to their S values will be done against the experimentally measured S values of the discussed samples, and not the ML-predicted values shown in **Figure 5-5**.

5.3.2 Impact of Oxide Inclusions in LPBF-Built $Bi_2Te_{2.7}Se_{0.3}$ *Parts*

As discussed in *Section 5.1.2*, both Welch *et al.* [28] and Liu *et al.* [150] discovered the presence of nanoscale, bismuth-rich oxides in their $Bi_2Te_{2.7}Se_{0.3}$ and Bi_2Te_3 samples, respectively. Welch *et al.* used bismuth-rich oxides to explain an observed transition from n-type to p-type character for their LPBF-built samples. Conversely, Liu *et al.* attributed their observed p-type to n-type conversion to the presence of similar bismuth-rich oxides. After building the high throughput $Bi_2Te_{2.7}Se_{0.3}$ samples and examining their cross-sections, it was discovered that oxide inclusions were present in our samples as well. Specifically, both bismuth-rich oxides and tellurium-rich lamellae were observed and are labeled in the backscattered electron (BSE) micrograph provided in **Figure 5-7**. Additionally, EDS results shown in **Figure 5-8** provided the necessary evidence to identify the oxide inclusions as bismuth-rich and the lamellae as tellurium-rich.

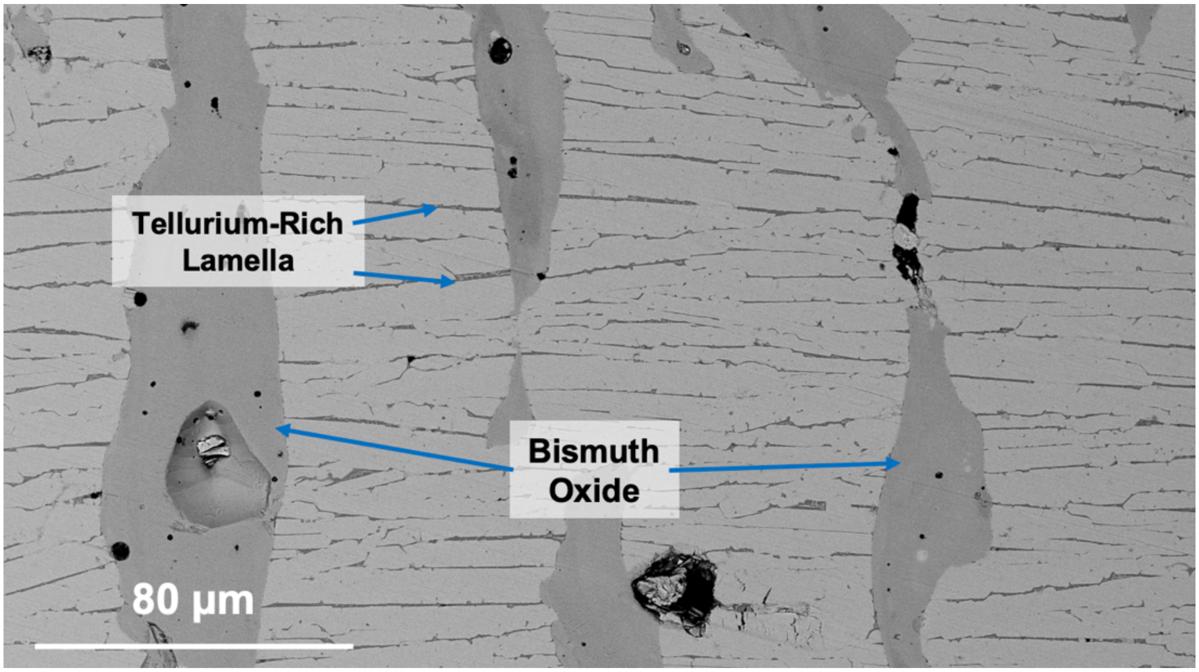

Figure 5-7. *Backscattered electron (BSE) micrograph of the microstructure of a high throughput, LPBF-built* $Bi_2Te_{2.7}Se_{0.3}$ *part. The presence of bismuth-rich oxides and tellurium-rich lamellae are labeled.*

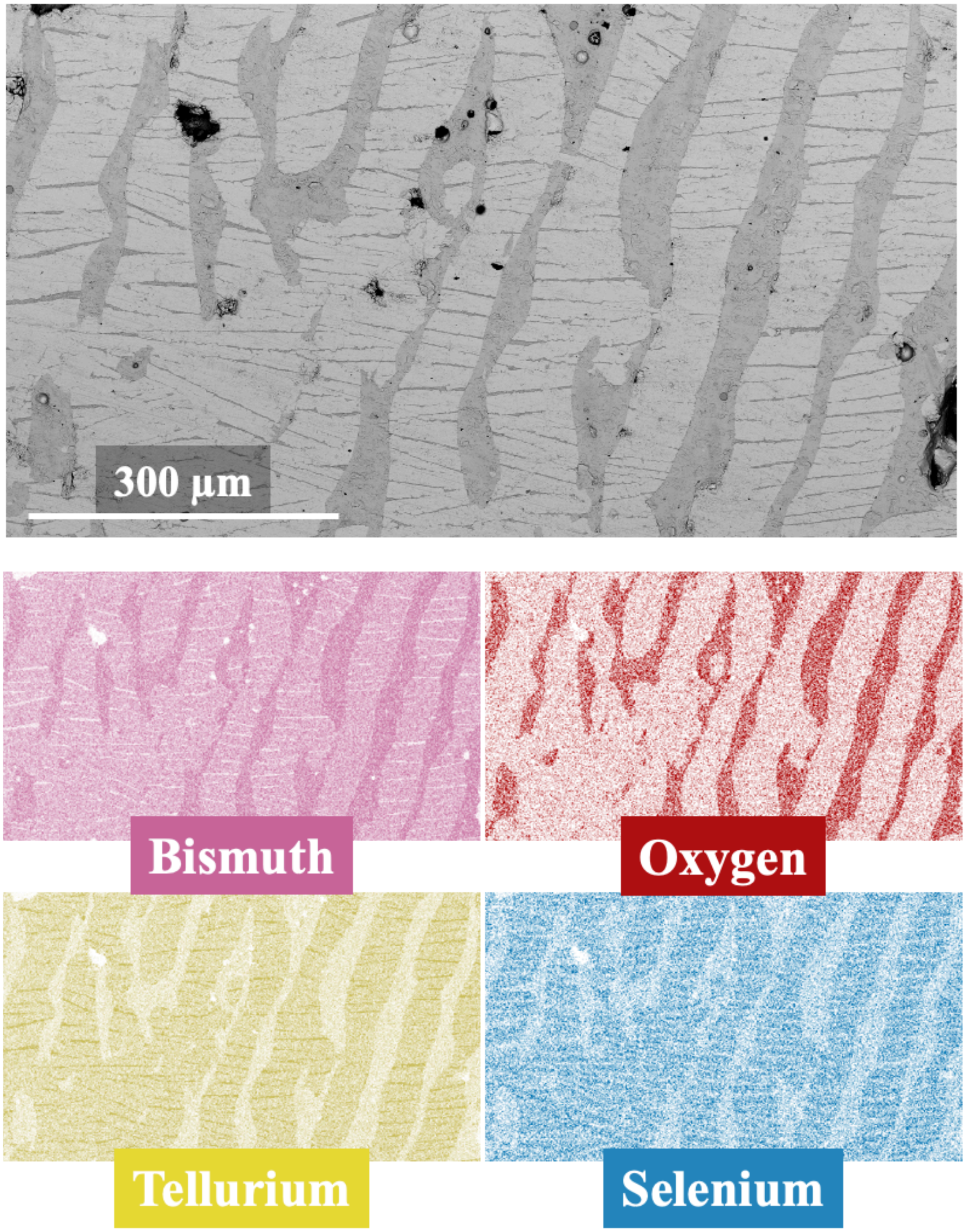

Figure 5-8. *Energy-dispersive X-ray spectroscopy (EDS) results used to identify the oxide inclusions as bismuth-rich and the dark lamellae as tellurium-rich. Higher concentrations are indicated by the darker colored regions for each of the analyzed elements.*

The bismuth-rich oxide inclusions present in these high throughput $Bi_2Te_{2.7}Se_{0.3}$ samples were not nanoscale, and instead were larger microscale oxides that tended to form vertically (along the build direction) and in between the parallel laser line scans. In contrast, the tellurium-rich lamellae typically formed horizontally, spanning the gap between these bismuth-rich oxides, similar to the results of Welch *et al*. With respect to the binary bismuth-tellurium phase diagram shown in **Figure 5-1**, it is argued that the formation of these bismuth-rich oxides caused a bismuth depletion in the local environment that resulted in a $Bi_2Te_{2.7}Se_{0.3}$-Te eutectic to form in the now tellurium-rich matrix. This would then explain the presence of the tellurium-rich lamellae. It is also believed that oxygen was introduced to these samples either through the oxidation of the starting powder and/or during the LPBF process due to the presence of oxygen in the build chamber. However, while bismuth-rich oxides were regularly observed in these LPBF-built, high throughput $Bi_2Te_{2.7}Se_{0.3}$ samples, there does not appear to be an obvious relationship between the presence of these bismuth-rich oxides and the magnitude or sign of S. It is also noted that these microscale bismuth-rich oxides were not observed in all LPBF-built samples and their formation did appear to depend on the processing conditions, as shown in **Figure 5-9**.

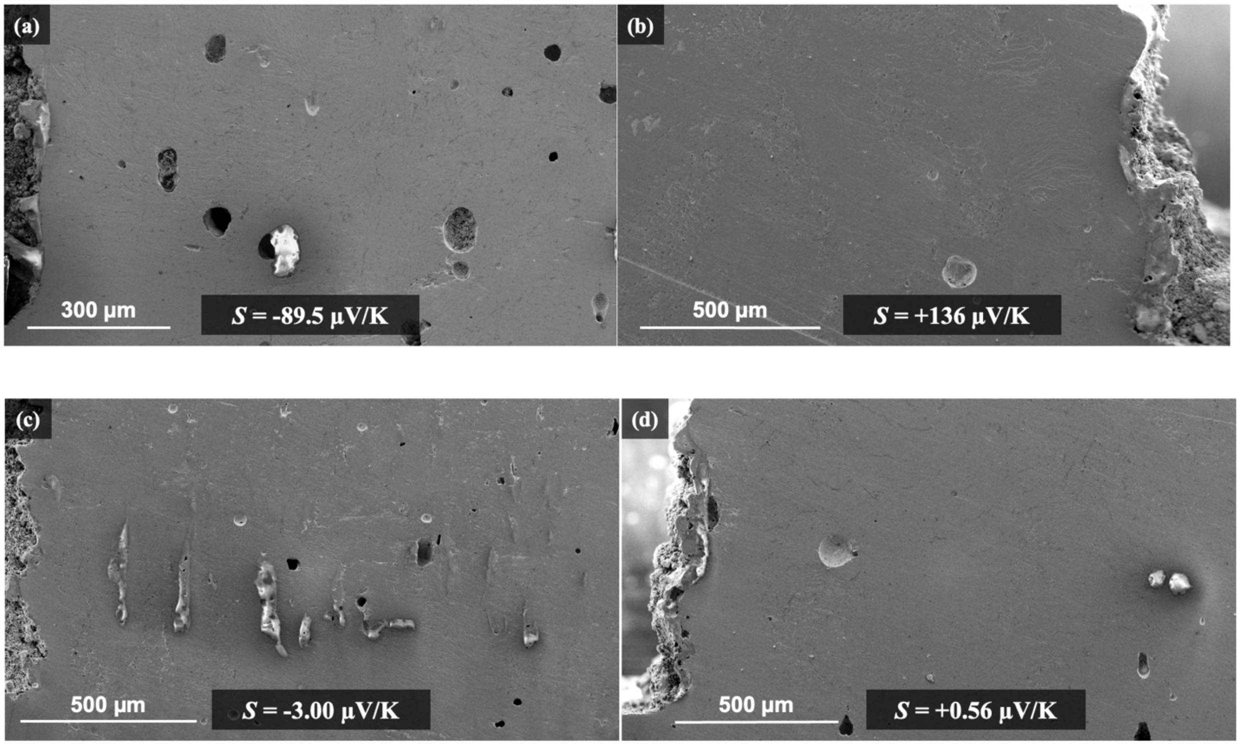

Figure 5-9. *Secondary electron (SE) cross-sectional micrographs of the LPBF-built* $Bi_2Te_{2.7}Se_{0.3}$ *samples. These samples were built using the following LPBF build parameters: (**a**) p = 30 W, v = 200 mm/s, h = 100 µm; (**b**) p = 35 W, v = 100 mm/s, h = 100 µm; (**c**) p = 30 W, v = 300 mm/s, h = 90 µm; and (**d**) p = 25 W, v = 100 mm/s, h = 90 µm. A layer thickness of t = 75 µm was used when building all four samples. The bismuth-rich oxides are visibly distinct and appear whiter due to charging.*

Provided in **Figure 5-9** are cross-sectional micrographs of four different high throughput $Bi_2Te_{2.7}Se_{0.3}$ samples containing varying amounts of the bulk, bismuth-rich oxides and varying values of S. The bismuth-rich oxides experienced some charging from the electron beam and so are visibly distinct from the rest of the matrix in these secondary electron micrographs owing to their whiter color. It should be noted that these micrographs of the bismuth-rich oxides were collected while conducting the porosity measurements, which means that three micrographs were collected for each high throughput, rectangular bar sample. While the volume of these oxides was not calculated like the porosity, the micrographs provided in **Figure 5-9** are representative of the oxide amount present in the other cross-sections for that sample.

Based upon these micrographs, there does not appear to be a clear correlation between the bismuth-rich oxides and the *S* magnitude or sign. It is observed that the sample in **Figure 5-9a** appeared to have a low volume of bulk bismuth-rich oxides, while no oxides were observed for the sample in **Figure 5-9b**. However, the **Figure 5-9a** sample had a very negative *S* (-89.5 μV/K) and the **Figure 5-9b** sample had a very positive *S* (+136 μV/K). Therefore, it seems unlikely that the presence or absence of the bismuth-rich oxides has a dominating impact on the charge carrier type or sign of *S*.

Then, to investigate the possible relationship between the bismuth-rich oxides and the magnitude of *S*, micrographs of two samples with near-zero values of *S* are provided in **Figure 5-9c** and **Figure 5-9d** (-3.00 and +0.56 μV/K, respectively). However, despite their similarly low magnitude *S* values, the **Figure 5-9c** sample clearly has a much larger volume of the bismuth-rich oxides than the **Figure 5-9d** sample. Therefore, it is posited that the bismuth-rich oxides do not play a significant role in the charge carrier concentration or magnitude of *S* either. This proposed and observed lack of correlation between the charge carrier type and the bismuth-rich oxides would seemingly contradict the already competing findings of both Welch *et al*. and Liu *et al*. It is acknowledged that these bismuth-rich oxides are much larger than the nanoscale oxide inclusions studied previously, however it is argued that if the proposed mechanism is a depletion of bismuth in the matrix, then this effect would logically be similar or even enhanced by larger, microscale oxides compared to sparse, nanoscale inclusions.

It is proposed that the limited impact of the bismuth-rich oxide inclusions is due to a self-regulating phenomenon in the matrix composition via tellurium-rich lamellae formation. Essentially, large bismuth depletions due to oxide formation are countered by the formation of a $Bi_2Te_{2.7}Se_{0.3}$-Te eutectic (observed in **Figure 5-7**) that removes excess tellurium from the matrix by forming tellurium-rich lamellae. The result is that the matrix maintains a composition close to the $Bi_2Te_{2.7}Se_{0.3}$ stoichiometry of the starting powder and the formation energies of the carrier contributing point defects are largely unaffected by the formation of bismuth-rich oxides. It should be emphasized that the takeaway is not specifically that the presence of these oxides has no impact on the *S*. Instead, it is concluded that these bismuth-rich oxide inclusions are not the main contributor to or a good indicator of the *S* values for these LPBF-built $Bi_2Te_{2.7}Se_{0.3}$ samples. Therefore, oxide formation is not the mechanism to explain or make use of the process parameter-dependent *S* variations shown in **Figure 5-5**.

5.3.3 LPBF-Produced Compositional Changes

The chemical composition of the matrix may still be a viable method of explaining and controlling the observed changes in *S* and should be investigated further. While oxide-induced bismuth depletion of the matrix may not significantly impact the material's *S* value, the potential impact of an anionic depletion of the matrix (reduced tellurium and/or selenium content) remains to be considered. It is well established for traditionally manufactured V_2VI_3 compounds that off-stoichiometric compositional changes can have a significant impact on the dominant charge carrier type and concentration through the stabilization of either electron donating or accepting point defects [27]. Even a 0.1 at% shift in composition can change the carrier concentration by 5×10^{19} cm^{-3} and shift the sign of the *S* [28].

It is known that the anionic elements (tellurium and selenium) of $Bi_2Te_{2.7}Se_{0.3}$ are more volatile than the cationic element (bismuth). This means that during high temperature processing conditions, selenium and tellurium are preferentially vaporized and their relative compositions are reduced in the final part compared to bismuth [27,158,159]. Further, it has been shown that the extent of this vaporization can be controlled through changes to the LPBF processing parameters, where the preferential loss of more volatile elements can be reduced by minimizing the laser energy density [160–162]. This relationship between the laser energy density and final composition has even been experimentally demonstrated previously for a $Bi_2Te_{2.7}Se_{0.3}$ starting stoichiometry in a selective laser melting (SLM) process, where Mao *et al.* [24] found that their laser-processed samples became more bismuth-rich with increasing volume energy density ($VED = \frac{p}{vht}$) values due to the higher vaporization rates of selenium and tellurium.

This presents a potential mechanism by which the processing parameters can be manipulated to intentionally change the composition of LPBF-built parts and therefore determine the final *S*. By increasing the VED, it may be possible increase the preferential vaporization of the anionic components and create LPBF-built parts that are tellurium- and selenium-deficient in the matrix. Consequently, this reduction in the anion concentration (and increased relative cation concentration) could be expected to result in the increased formation of electron accepting point defects and explain the observed formation of p-type parts from an n-type $Bi_2Te_{2.7}Se_{0.3}$ starting composition. To study this possible mechanism, μXRF was used to analyze the bismuth, tellurium, and selenium compositions of six high throughput, LPBF-built samples. The small spot size associated with μXRF allowed the composition of the matrix in between the bismuth-rich oxides to be isolated and probed. These results are provided in **Figure 5-10** as graphs that plot the μXRF composition results against the measured *S* values for these high throughput samples.

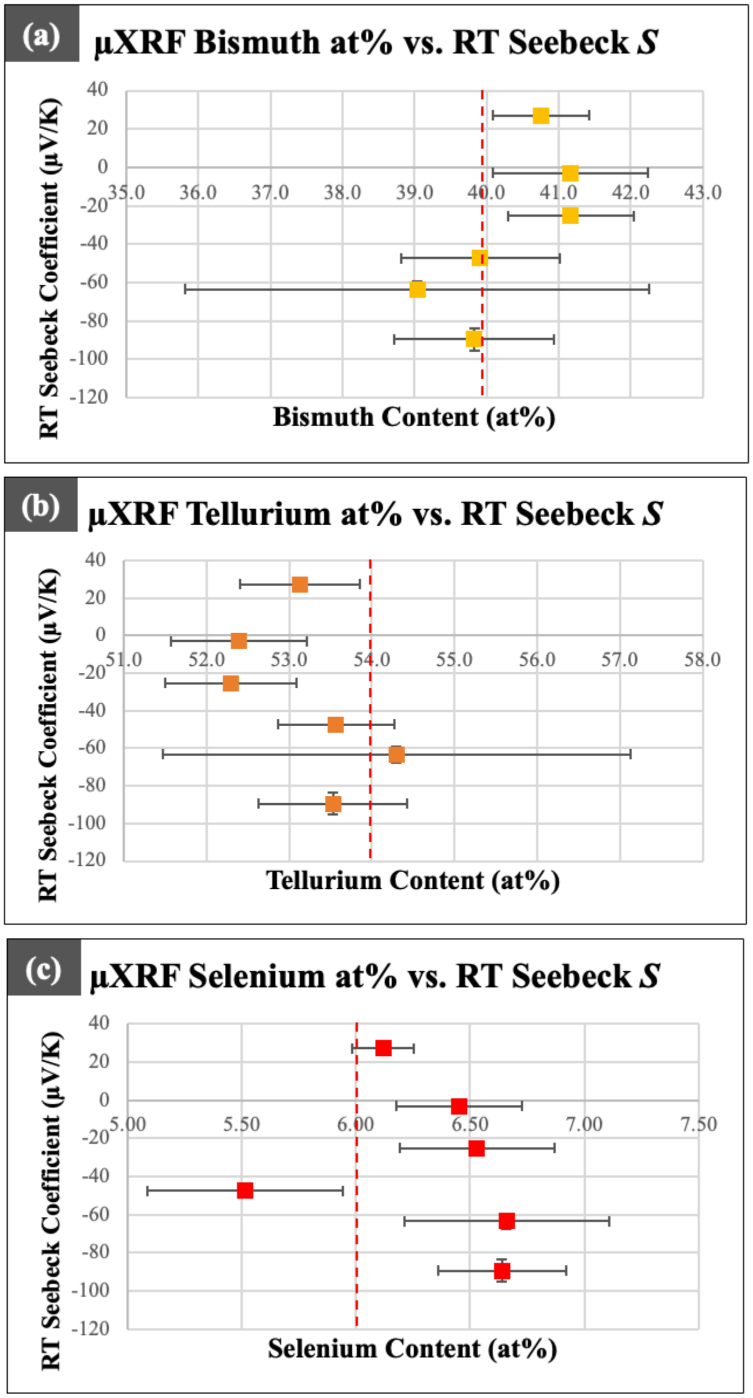

Figure 5-10. *Scatterplots showing the relationship between the (**a**) bismuth, (**b**) tellurium, and (**c**) selenium at% compositions (measured using µXRF) against the RT Seebeck coefficients (S) for the LPBF-built, high throughput* $Bi_2Te_{2.7}Se_{0.3}$ *samples. The expected at% compositions for stoichiometric* $Bi_2Te_{2.7}Se_{0.3}$ *are shown using the red dashed lines. The S error bars come from the ± 6.5 % uncertainty in their measurements and the error bars in the µXRF data were calculated from the standard deviations of the multiple point measurements conducted for each sample.*

The expectation is that the *S* should increase (increased p-type character) with increasing bismuth content. Conversely, the *S* should decrease (increased n-type character) with increasing tellurium and selenium content. With respect to the average composition values shown in **Figure 5-10**, it is possible that this trend is observed. However, the large error bars in the composition data make it difficult to state any trends conclusively. As a result, WDS measurements were also conducted for four LPBF-built Bi_2Te_3 samples against a standard, binary Bi_2Te_3 sample of known composition to yield low uncertainty values of ± 0.39 at% for bismuth and ± 0.17 at% for tellurium. This WDS composition data is provided in **Figure 5-11** and compared against the RT *S* values for these samples. One interesting observation to note is that despite all being built from powders with the same Bi_2Te_3 starting composition, large compositional deviations are observed in several of these samples approaching a BiTe stoichiometry.

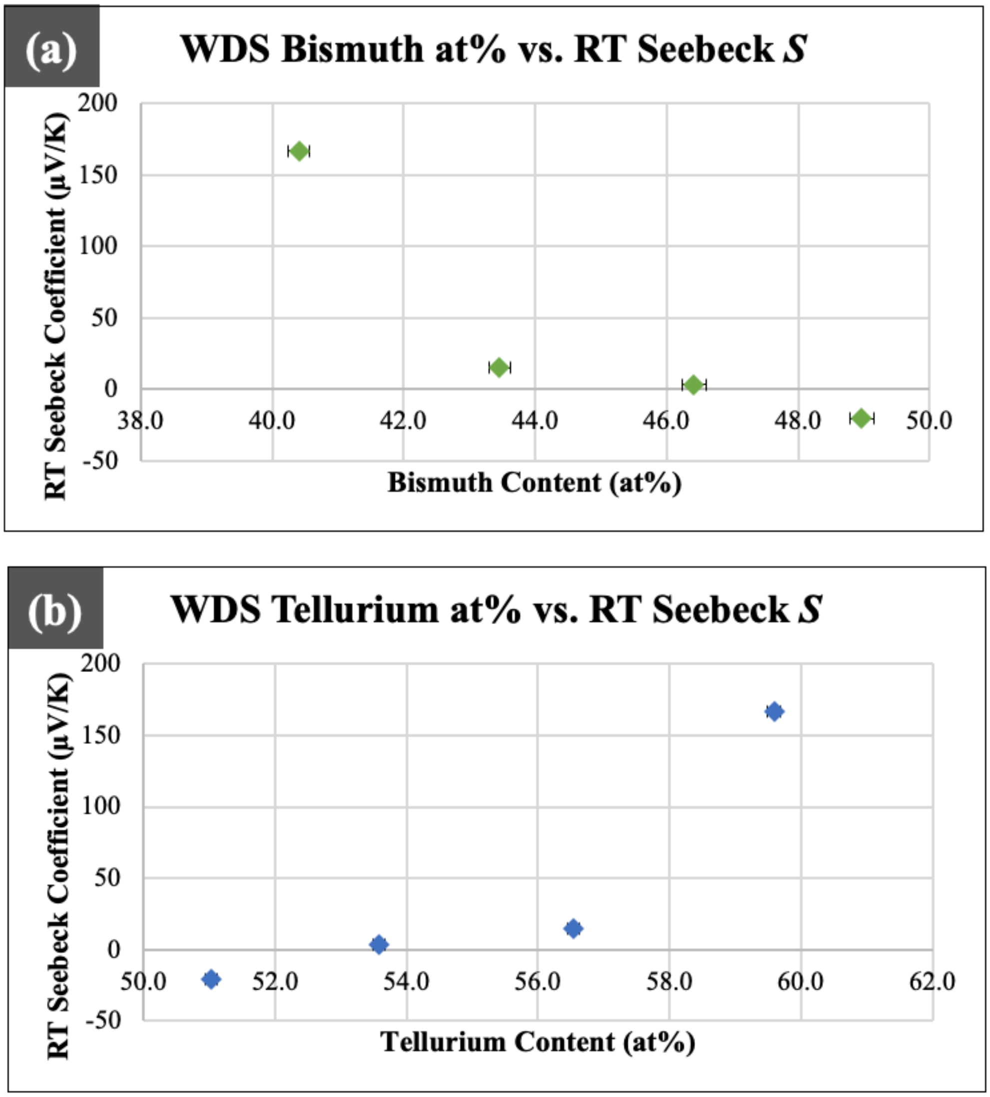

Figure 5-11. *Scatterplots showing the relationship between the (**a**) bismuth and (**b**) tellurium at% compositions (measured using WDS) against the RT Seebeck coefficients (S) for the LPBF-built* Bi_2Te_3 *samples constructed by Open Additive. Error bars for the S and WDS composition measurement uncertainties are provided, although many are too small to visualize for these data ranges.*

From the data shown in **Figure 5-11**, it is much easier to make observations about the relationship between the RT *S* and composition values for the LPBF-built samples. For these four samples, it appears to be the case that the S is decreasing with increasing bismuth content and decreasing tellurium content. However, this is exactly the opposite of the trend expected from traditionally manufactured V_2VI_3 materials. A mechanism for a cation-induced reduction in the *S* is both unexpected and has not been previously explored.

Finally, the plot shown in **Figure 5-12** is created to collectively compare the impact of matrix composition for all the characterized samples on their RT *S* values. For these purposes, it is assumed that the anionic selenium in $Bi_2Te_{2.7}Se_{0.3}$ substitutes in at the anionic tellurium sites, and so comparisons of the RT *S* are isolated to changes in the similar cationic bismuth composition. For both the $Bi_2Te_{2.7}Se_{0.3}$ (µXRF) and Bi_2Te_3 (WDS) samples, the expected relative bismuth composition is 40 at %. It is acknowledged that the presence of selenium likely impacts the *S* value of the µXRF measured samples and is expected to increase their n-type character. As a result, **Figure 5-12** is provided to make relative, qualitative comparisons of the observed trends.

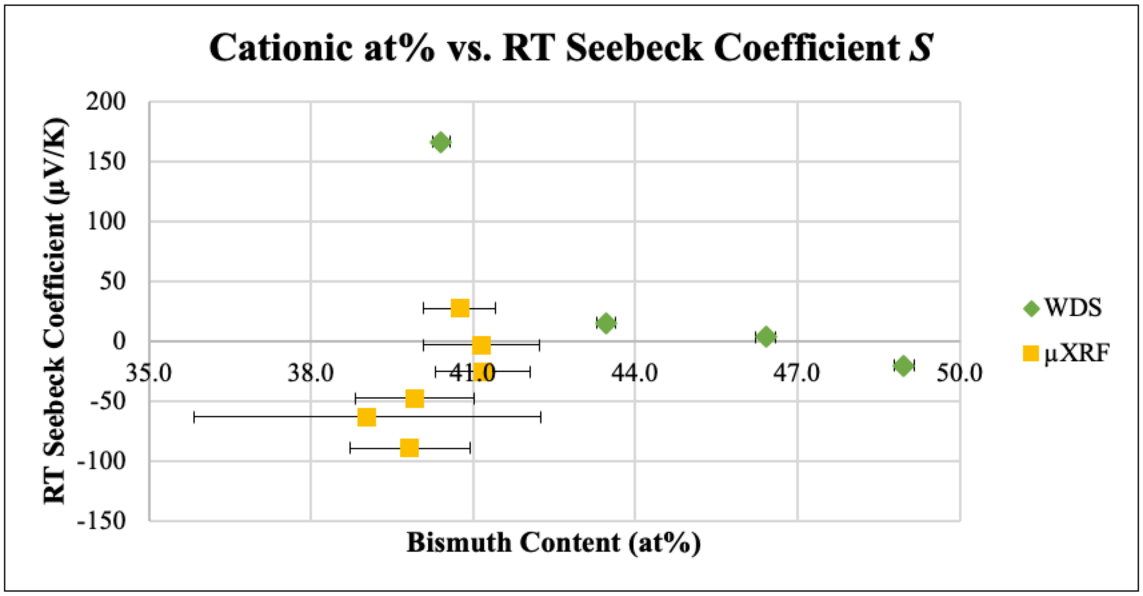

Figure 5-12. Scatterplots showing the relationship between the cationic bismuth at% composition against the RT Seebeck coefficients (S) for the LPBF-built $Bi_2Te_{2.7}Se_{0.3}$ (µXRF) and Bi_2Te_3 (WDS) samples. Error bars for the S and composition measurement uncertainties are provided, although several are too small to visualize for these data ranges.

From the combined µXRF and WDS data shown in **Figure 5-12**, there does not appear to be any obvious trend or relationship between the relative cation content and the sign of the RT *S*.

For small perturbations around the expected bismuth content of 40 at%, both negative and positive *S* values are observed ranging from -89.5 to 167 μV/K. At larger bismuth contents approaching 50 at%, the magnitude of *S* does appear to be diminished to near-zero values. This data is not meant to indicate that definitive claims can be made from ten data points. However, a broad range of over 10 at% is investigated and it is argued that if composition is a primary driver of the LPBF-produced *S* variations, then large changes and obvious trends should be observed. Ultimately, such relationships are not clear from the composition data provided in **Figure 5-12**. Therefore, it is argued that the matrix composition is also not a not the main contributor to or a good indicator of the charge carrier type for these LPBF-built bismuth telluride samples.

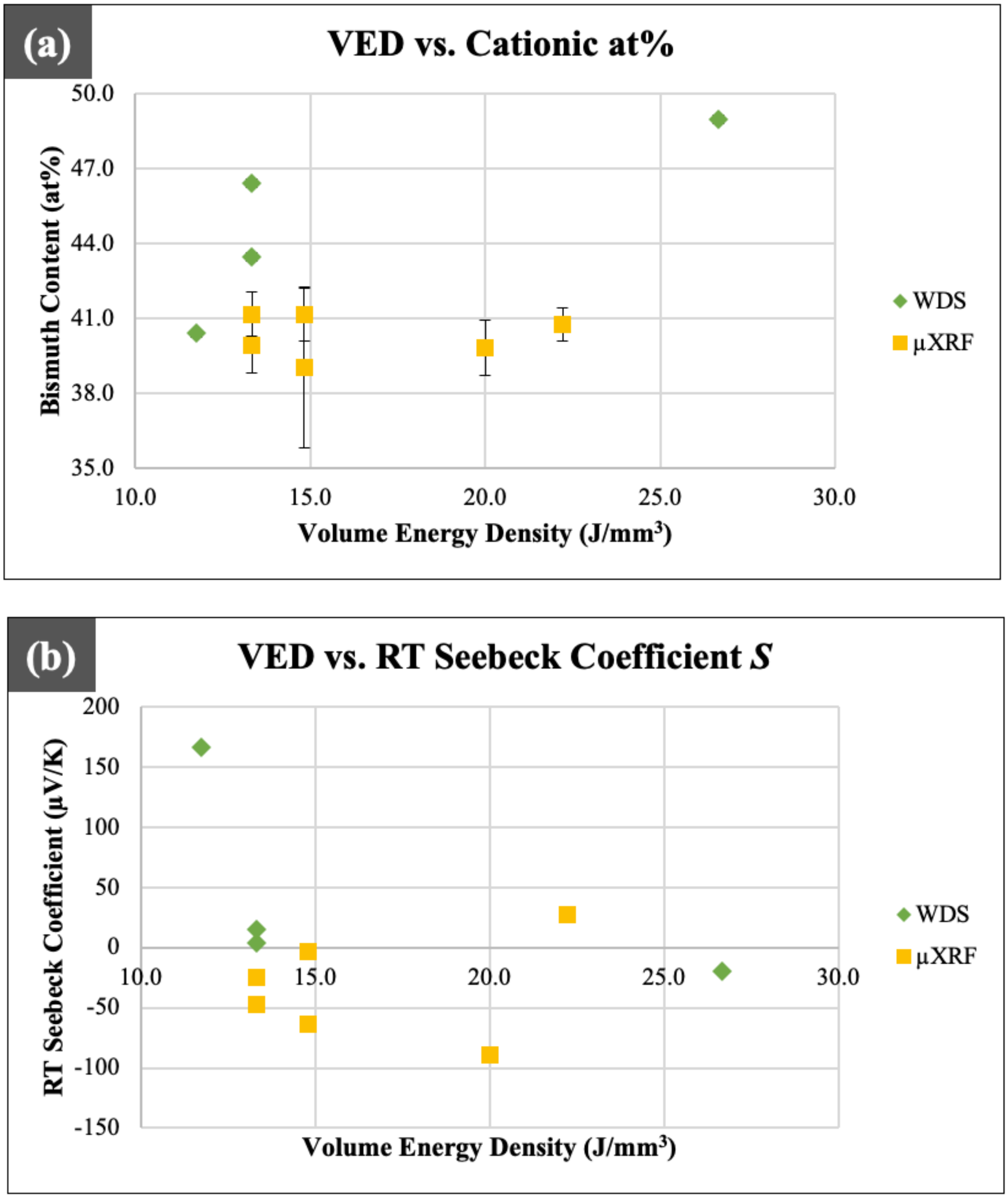

Figure 5-13. *Scatterplots showing the relationship of the Volume Energy Density (VED) to the (**a**) cationic bismuth at% composition and (**b**) RT Seebeck coefficient (S) for the LPBF-built* $Bi_2Te_{2.7}Se_{0.3}$ *(µXRF) and* Bi_2Te_3 *(WDS) samples.*

Comparison of the VED to the cationic bismuth content and RT *S* were created and are shown in **Figure 5-13**. With respect to the data in **Figure 5-13a**, there appears to be a slight trend where an increase in the VED generally correlates with an increased relative bismuth at%. This aligns well with the previously described expectations and prior findings from Mao *et al.* [24]: larger laser energy densities result in increased vaporization of the more volatile anionic elements and the relative bismuth concentration is correspondingly increased. As a result, the VED is also compared to the RT *S* measurements in **Figure 5-13b**. However, similar to the composition comparisons to *S*, there does not appear to be a significant relationship between the laser energy density and the magnitude or sign of the *S* in the final, LPBF-built parts. Therefore, it is concluded that while the expected relationship between energy density and composition is observed, this correlation is not carried over to the RT *S*. Once again, while we cannot conclude that composition has no impact on the semiconducting behavior of these LPBF-built, bismuth telluride samples, the results shown in this section suggest that matrix composition is also not a primary (or at least dominating) driver of the LPBF processing parameter controlled *S* values observed in **Figure 5-5**.

5.3.4 Impact of Bulk Porosity in LPBF-Built $Bi_2Te_{2.7}Se_{0.3}$ Parts

After fabricating and measuring the *S* for the high throughput, $Bi_2Te_{2.7}Se_{0.3}$ samples, their cross-sections were also studied using SEM to investigate the resulting microstructural features and porosities. As a result, a graph could be generated that compared the average porosity to the RT *S* values for these 35 samples and is provided in **Figure 5-14**. The raw porosity data for these 35 high throughput samples can be found in **Table 5-1** in the Appendix. It is known that the *S* depends most heavily on the Fermi level, carrier concentration, carrier effective mass, and temperature [163]. As a result, a change in bulk porosity is not expected to have a significant impact on a bulk material's *S*. Experimentally, this has been previously demonstrated in Bi_2Te_3 and $Bi_{0.4}Sb_{1.6}Te_3$ materials where an increase in bulk porosity yielded a decrease in the electrical conductivity (σ) and an even greater decrease in the thermal conductivity (κ) with little change to the *S* [164,165]. Similar results are evident from the data shown in **Figure 5-14**, where no discernable relationship between the amount of porosity and RT *S* is observed. This is especially true for high-density samples (>90 %), where both positive and negative *S* values were measured with a range of magnitudes (-89.5 to 136.0 μV/K).

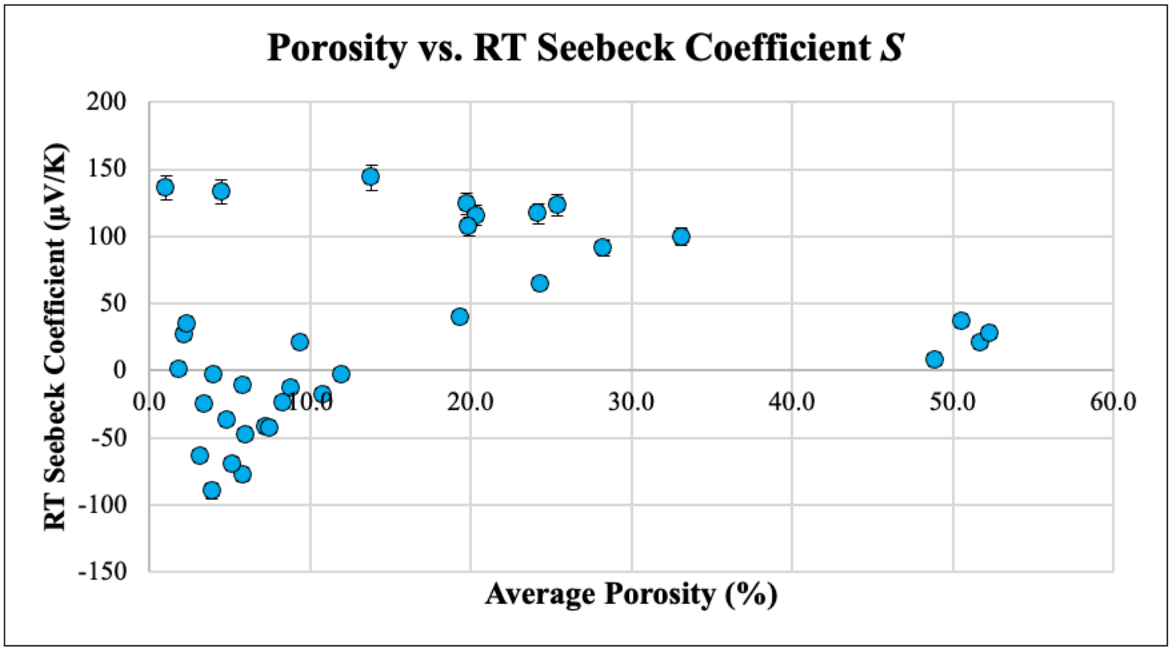

Figure 5-14. *Scatterplot showing the average percent porosity versus RT Seebeck coefficient (S) for the 35 high throughput, LPBF-built $Bi_2Te_{2.7}Se_{0.3}$ parts.*

It is worth pointing out that the p-type LPBF-built $Bi_2Te_{2.7}Se_{0.3}$ parts created by Welch *et al*. [28] had an average density of 74 %. Around similar density values, only p-type character was observed in our samples as well. It is also noted that n-type behavior was not observed in the lower density samples when the average porosity exceeded 15 %. However, in practice it would not be productive to intentionally fabricate low-density, bulk bismuth telluride samples due to the resulting loss in mechanical performance and expected inability to construct enhanced geometry parts. Therefore, further study on porosity's ability to change the *S* value for LPBF-built bismuth telluride materials is expected to yield limited correlation and is difficult to justify for real-world applications.

5.3.5 Considerations of the Donor-Like Effect in LPBF-Built $Bi_2Te_{2.7}Se_{0.3}$ Parts

Another possible contributor to this LPBF-facilitated n-type to p-type transition could be the "donor-like effect," which has been frequently studied and applied to traditionally manufactured V_2VI_3 TE materials. This effect describes a mechanism by which deformation can be used as a means of controlling the carrier type and concentration of a TE material. With sufficient mechanical deformation, it has been found that p-type materials may be inverted to n-type. This deformation can be carried out pre-synthesis (*e.g.*, ball milling), during synthesis (*e.g.*, hot deformation), or post-synthesis (*e.g.*, pressing). The explanation for this phenomenon is that heavy plastic deformation produces non-basal slips, anionic vacancies, and therefore excess electrons in V_2VI_3 compounds [150,166]. The conventional mechanism for the donor-like effect is expressed in the following equation for Bi_2Te_3 [27,150]:

$$2V_{Bi}''' + 3V_{Te}^{\cdot\cdot} + Bi_{Te}' \rightarrow V_{Bi}''' + Bi_{Bi}^{x} + 4V_{Te}^{\cdot\cdot} + 6e'$$

The extent of deformation (*e.g.*, ball milling time) has consistently been shown to correlate well with increased electron concentration and n-type character. As a result, one might expect the donor-like effect to be impactful during the LPBF process where repeated thermal cycles are known to induce distortions and residual stress that may provide the necessary mechanical deformation [167–169]. However, it is argued that this donor-like effect would not provide a reasonable explanation for the majority charge carrier switching observed in these LPBF-built parts. First, the donor-like effect describes a process by which p-type to n-type conversion can be facilitated by a deformation-induced generation of electron donating point defects. In contrast, it has been found in this study and in prior works that LPBF produces conversions in the opposite direction, where an n-type $Bi_2Te_{2.7}Se_{0.3}$ starting material is converted to p-type at certain processing conditions.

Second, our results do not agree with the expectations of the “recovery effect,” which is often used as a post-processing technique in tandem with the donor-like effect. The recovery effect describes a thermal control process where annealing can reverse the donor-like effect through the annihilation of anionic vacancies through dislocation climb and array formation [26,27,166]. As a result, deformed n-type materials can be converted back to p-type with sufficient annealing conditions. In contrast, the annealing results shown and discussed in Chapters 3 and 4 once again demonstrate an opposite result, where the S became more negative after annealing and the n-type character was increased. Additionally, the proposed point defect mechanism provided above has met challenges both experimentally and theoretically. For example, the anionic tellurium vacancies ($V_{Te}^{\cdot\cdot}$) are energetically unfavorable in nearly all bismuth telluride chemical environments and their formation energy is much higher than that of the possible antisite defects ($Bi_{Te}'$and $Te_{Bi}^{\cdot}$) [150]. Therefore, it is argued that the donor-like effect cannot accurately predict or explain the LPBF-induced deformation impacts to TE properties and is not a promising option for future experimental effort.

5.4 Conclusions

Through an iterative system of ML predictive modeling and experimental validation, it was both predicted and experimentally observed that the magnitude and sign of the Seebeck coefficient (S) could be intentionally manipulated through changes to the LPBF processing parameters. It was hypothesized that this variation in S was the result of changes to the formation and concentrations of carrier contributing point defects in the bismuth telluride parts. As a result, it was deemed necessary to identify and study the impact that the LPBF process was having on the as-built material properties that ultimately yielded the observed changes in S. To this end, the roles of bismuth-rich oxide formation, matrix composition, and bulk porosity in deciding or predicting the RT *S* of LPBF-built bismuth telluride parts were studied. In the end, experimental results failed to produce any clear trends between these three material properties and the corresponding *S* values. Additionally, it is argued that the deformation-based mechanisms explained by the donor-like effect can also not adequately explain the observed, LPBF-induced charge carrier modifications shown in **Figure 5-5**. Consequently, it was concluded that none of these factors are responsible for dominating the observed changes in *S* produced by variations in the LPBF fabrication process. Ultimately, a LPBF-enabled ability to alter the dominant charge carrier type and concentration of bismuth telluride materials to produce a range of *S* values is demonstrated. However, the underlying mechanism for this behavior remains to elucidated.

5.5 Recommendations for Future Work

While the presented data have been unable to explain this LPBF-controlled Seebeck coefficient phenomenon through the presence of oxide inclusions, matrix composition changes, or bulk porosity, it is still believed that control over the intrinsic point defect types and formations is the most likely explanation for the altered *S* values and charge carrier concentrations of these LPBF-built parts. It is consequently argued that further and more rigorous study of these point defects as a result of LPBF processing parameter manipulation is highly justified. The pair distribution function (PDF) is a very promising technique for further research as it can be used to generate a scaled histogram of the interatomic distances in a material [170,171]. As a result, the PDF can be used in combination with crystal structure computational models to not only locate and quantify the various point defects, but also to correlate those findings to the measured *S* and other TE property values. However, such capabilities are only possible using high energy neutron and X-ray sources, such as those found at synchrotron facilities. Another possible technique to consider is photoemission electron microscopy (PEEM), which could be used to spatially measure the work function to correlate with stoichiometry.

5.6 Appendix

The full raw data for the 35 high throughput, LPBF-built $Bi_2Te_{2.7}Se_{0.3}$ samples are provided in **Table 5-1**, along with their RT Seebeck coefficient (S) and average percent porosity values. This data was used to iteratively train the ML model and produce the *S* prediction and uncertainty maps provided in **Figure 5-5** and **Figure 5-6**, respectively. These experimentally determined RT *S* and average porosity percentage values were also used to construct the scatterplot shown in **Figure 5-14**.

Table 5-1. *The full 35 high throughput, LPBF-built $Bi_2Te_{2.7}Se_{0.3}$ samples alongside their RT Seebeck coefficient (S) and average porosity values. The uncertainty for the experimentally measured RT S values is ± 6.5 % (1 sigma). The average percent porosity measurements collected across three cross sections for each sample are also provided.*

LPBF Processing Parameters				**RT Seebeck Coefficient**	**Average Porosity**
Power *p* (W)	**Scan Speed *v* (mm/s)**	**Hatch Spacing *h* (µm)**	**Layer Thickness *t* (µm)**	***S* (µV/K)**	**(%)**
25	400	130	75	143	13.8
25	400	120	75	-2.79	12.0
20	300	100	75	-12.5	8.8
20	300	90	75	21.1	9.4
23	500	90	75	116	24.2
23	500	80	75	124	19.7
20	200	100	75	-25.2	3.4
30	300	100	75	-47.4	6.0
30	200	100	75	-89.5	3.9
20	200	90	75	-63.4	3.2
30	300	90	75	-3.00	4.0
30	200	90	75	27.2	2.2
35	100	100	75	136	1.1
30	150	90	75	35.1	2.3
25	100	90	75	0.563	1.9
30	450	80	75	-23.8	8.4
25	400	130	75	116	20.3
30	200	100	75	133	4.5

20	300	90	75	-10.6	5.8
20	300	90	75	-36.3	4.8
20	300	90	75	-41.4	7.3
20	300	90	75	-43.0	7.5
20	300	90	75	-17.7	10.8
25	400	80	75	39.9	19.4
35	500	90	75	64.7	24.3
20	500	90	75	36.9	50.5
35	500	100	75	91.1	28.2
20	500	100	75	7.43	48.9
30	200	100	75	-77.6	5.8
25	400	80	75	107	19.9
35	500	90	75	123	25.4
20	500	90	75	20.5	51.7
35	500	100	75	99.4	33.1
20	500	100	75	28.0	52.3
30	200	100	75	-69.5	5.2

Chapter 6. Conclusions and Recommendations for Future Work

6.1 Summary of Research

The works described in this dissertation present a hierarchical methodology by which LPBF can be successfully applied to the creation of bismuth telluride parts for the intentional modification and enhancement of TE properties. Specifically, the effects of the LPBF process on material properties and TE behaviors are explored and relationships are established. Further, alterations of these TE properties by a post-processing anneal are identified and potential mechanisms are defined. Ultimately, TE property control has been demonstrated across multiple length-scales through modifications to the LPBF manufacturing process.

Significant results concluded from these studies can be summarized by the following:

1) An iterative process of experimental validation and augmented machine learning (ML) predictive modeling was created that allowed for the rapid understanding and visualization of $Bi_2Te_{2.7}Se_{0.3}$ melting behavior within the LPBF processing parameter space (laser power (p) vs. scan speed (v)). Consequently, processing parameter combinations capable of building crack-free, highly dense (>99 %) $Bi_2Te_{2.7}Se_{0.3}$ samples were quickly identified: $p = 25$ W, $v = 400$ mm/s, $h = 80$ µm, and $t = 75$ µm. The high quality achieved in these parts was successfully demonstrated through the LPBF fabrication of free-standing $Bi_2Te_{2.7}Se_{0.3}$ parts in complex, nonstandard geometries (**Figure 2-11**). The most noteworthy benefits of this work are two-fold:
   i. The ability to manufacture bismuth telluride parts through LPBF creates an opportunity to improve TE efficiency through bulk geometry enhancements, as predicted by prior modeling work (**Figure 2-1**) using shapes that are currently impossible to produce using traditional manufacturing methods.

    ii. This augmented ML approach is not specific to bismuth telluride or TE materials. Instead, it can be similarly and broadly applied to the rapid development of LPBF processing strategies for any new AM material.

2) A post-processing anneal of 350 ºC for 24 hours was employed to connect the material properties and TE behaviors of as-built and heat treated $Bi_2Te_{2.5}Se_{0.5}$ samples fabricated using LPBF. Positron annihilation Doppler broadening spectroscopy (DBS), Hall measurements, and EBSD were all used to characterize the annealing-affected properties of the $Bi_2Te_{2.5}Se_{0.5}$ parts to propose mechanisms for the observed improvements to electrical conductivity (σ), thermal conductivity (κ), Seebeck coefficient (S), and TE figure of merit (ZT). These conclusions are best understood when separately addressed as changes to the material properties and then the corresponding impacts to the TE properties.

   First, impacts to the material properties via LPBF and annealing were identified:

    i. DBS (**Figure 3-6**) and Hall measurements (**Figure 3-7**) were used to directly measure an annealing-induced reduction in cationic vacancy point defect and charge carrier concentrations, respectively. Additionally, temperature-dependent (TD) σ measurements shown in **Figure 3-5** provided evidence for semiconductor degeneracy and metal-like behavior in the LPBF-built parts, induced by a high saturation of charge carriers. Therefore, it is said that the rapid solidification LPBF process resulted in samples with high point defect and charge carrier concentrations. Further, these concentrations could then be reduced by annealing.

    ii. EBSD data showed that not only did LPBF produce parts composed almost entirely of low angle grain boundaries (LAGBs), but that the average misorientation angles of these LAGBs experienced a slight 6.0 % increase after annealing. It is argued that annealing provided the necessary energy for dislocation motion from the bulk to the grain boundaries, where the resulting increase in dislocation density yielded the observed increase in misorientation angle. Additionally, a heavily dominant number of LAGBs was maintained even after annealing at 350 ºC for 24 hours.

Second, mechanisms are posited to connect these material property changes to the improved TE property behaviors observed:

i. The RT σ <u>increased</u> by roughly 17.5 % after annealing. It is argued that this enhanced σ is driven by an improved carrier mobility (μ) resulting from the removal of electron scattering, charged point defects and a reduced carrier concentration (n). Additionally, an observed increase in grain size and the expected reduction in bulk dislocation density may have reduced electron scattering sites after annealing, thus improving the μ and contributing to the annealing-induced increase in σ.

ii. The RT κ <u>decreased</u> by roughly 18.4 % after annealing. This reduced κ is attributed to the annealing-induced increase in LAGB misorientation angles and associated increase in dislocation density. This decrease in dislocation spacing at the grain boundaries is expected to improve phonon scattering and decrease the lattice component of the thermal conductivity (κ_L), which then drives the observed reduction in the overall κ. Additionally, this is accomplished while maintaining LAGBs and therefore without adversely impacting the charge carrier transport.

iii. The RT S <u>increased</u> by roughly 212 % after annealing. This is explained by the known relation $|S| \sim n^{-\frac{2}{3}}$, where the annealing-induced removal of charge carrier contributing point defects and consequent reduction in carrier concentration directly yielded an improved Seebeck coefficient for these degenerate semiconductors.

iv. Finally, the RT ZT increased by roughly 1300 % after annealing. The σ, κ, and S values were all altered in beneficial ways to improve the TE efficiency, as expected from the equation $ZT = \frac{\sigma S^2}{\kappa} T$.

3) It was found that the thermal gradients and directional solidification associated with LPBF can be used to intentionally fabricate $Bi_2Te_{2.5}Se_{0.5}$ parts with strong crystallographic textures. Specifically, it was found that the c-axis ([0001] direction) is isolated to the build and scan sample directions, while the perpendicular transverse direction lies almost entirely in the basal plane for these LPBF-built samples. Consequently, TE property measurements confirmed that the electrical and thermal transport properties (σ and κ) were enhanced when measured in the basal plane (along the transverse direction) compared to measurements taken along the build direction, in agreement with prior literature on traditionally manufactured bismuth telluride materials. Further, these directionally enhanced transport properties persisted after annealing.

It was also shown that an anisotropic S in the as-built parts could be converted to isotropic behavior after annealing due to the removal of RT bipolar conduction and multicarrier effects. This provided further evidence for a reduction in supersaturated majority and minority charge carrier concentrations after a 350 ºC anneal for 24 hours. Finally, it is concluded that the enhanced transport properties and restored S isotropy after annealing can be purposefully leveraged to increase the TE efficiency (ZT) in the basal plane and transverse direction of LPBF-built, $Bi_2Te_{2.5}Se_{0.5}$ parts.

4) A system of high throughput sample fabrication and characterization alongside ML predictive modeling allowed for the rapid visualization of changing *S* values throughout the LPBF processing parameter space (*p* vs. *v* vs. *h*). This work demonstrated that the sign and magnitude of *S* can be purposefully controlled through alterations to the LPBF processing conditions. It is argued that this variation in *S* is due to changes in the preferential formation of carrier contributing point defects that are ultimately responsible for the dominant charge carrier types and concentrations. Bismuth-rich oxide formation, matrix compositions, and bulk porosity were all studied as potential drivers for this LPBF-enabled ability to modify *S*. However, obvious trends and relationships between the experimental data and corresponding *S* values were not observed and so it was concluded that these LPBF-affected material properties do not dominate the observed changes in carrier type or concentration. Additionally, it is argued that the deformation-based donor-like effect that is commonly applied to traditionally manufactured V_2VI_3 parts also cannot adequately account for the n-type to p-type transition found in these LPBF-built samples. In the end, it is shown that LPBF can be used to deliberately alter the dominant charge carrier type and concentration of a $Bi_2Te_{2.7}Se_{0.3}$ material to produce a range of *S* values. However, the mechanisms for this control are not yet understood.

Therefore, meaningful connections are observed and established between the LPBF process and resulting TE behaviors of bismuth telluride alloys through modified material properties across a range of length-scales. In the end, these studies and conclusions are provided with the unifying goal of purposefully controlling TE properties through LPBF process alterations. Additionally, these defined relationships should not only benefit the continued fabrication of optimized bismuth telluride parts for TE applications, but also the necessary pool of knowledge for the successful AM construction of materials with enhanced, intentional functional properties.

6.2 Recommendations for Future Work

One of the greatest challenges to studying TE materials and properties is the complex interrelationships that they share with one another. For example, the formation of charge carrier contributing point defects can directly impact the electrical conductivity, thermal conductivity, and Seebeck coefficient in a myriad of potentially self-conflicting ways based upon their type and concentration. As a result, specific mechanisms and impacts to the TE efficiency can be difficult to isolate and discern without exhaustive and time-consuming experimental effort. For these reasons, the works discussed in this dissertation have heavily emphasized the use and investigation of one processing parameter combination (p = 25 W, v = 400 mm/s, h = 80 μm, and t = 75 μm) and one annealing condition (350 ºC for 24 hours). In doing so, multi-scale characterization efforts were employed to thoroughly study and confidently establish relationships that connect the bismuth telluride alloy material properties to their resulting TE properties.

However, it is neither believed nor argued that this specific set of processing and post-processing conditions has yielded the best TE materials that LPBF can create. Therefore, in addition to the suggested future research enumerated at the ends of Chapters 2 through 5, the most significant work that remains on this topic essentially amounts to an optimization problem. Specifically, an investigation into an expanded range of LPBF process parameters and annealing conditions alongside ML predictive modeling efforts could be used to better understand the systems that control TE properties (σ, κ, and S). It is the hope that the mechanisms defined and defended in this dissertation can provide essential tools for the creation of optimized TE materials with improved conversion efficiencies through LPBF.

References

[1] J. He, T.M. Tritt, Advances in thermoelectric materials research: Looking back and moving forward, Science (80-.). 357 (2017). https://doi.org/10.1126/science.aak9997.

[2] Z.G. Chen, G. Hana, L. Yanga, L. Cheng, J. Zou, Nanostructured thermoelectric materials: Current research and future challenge, Prog. Nat. Sci. Mater. Int. 22 (2012) 535–549. https://doi.org/10.1016/j.pnsc.2012.11.011.

[3] G. Tan, L.D. Zhao, M.G. Kanatzidis, Rationally Designing High-Performance Bulk Thermoelectric Materials, Chem. Rev. 116 (2016) 12123–12149. https://doi.org/10.1021/acs.chemrev.6b00255.

[4] C. Forman, I.K. Muritala, R. Pardemann, B. Meyer, Estimating the global waste heat potential, Renew. Sustain. Energy Rev. 57 (2016) 1568–1579. https://doi.org/10.1016/j.rser.2015.12.192.

[5] G.J. Snyder, S. LeBlanc, D. Crane, H. Pangborn, C.E. Forest, A. Rattner, L. Borgsmiller, S. Priya, Distributed and localized cooling with thermoelectrics, Joule. 5 (2021) 748–751. https://doi.org/10.1016/j.joule.2021.02.011.

[6] W.O.I. Bohorquez, J.R. Barbosa, L.A.H. Nogueira, E.E.S. Lora, Repowering: An option for refurbishment of old thermal power plants in Latin-American countries, Proc. ASME Turbo Expo. 1 (2010) 825–834. https://doi.org/10.1115/GT2010-23058.

[7] A. El-Desouky, M. Carter, M.A. Andre, P.M. Bardet, S. LeBlanc, Rapid processing and assembly of semiconductor thermoelectric materials for energy conversion devices, Mater. Lett. 185 (2016) 598–602. https://doi.org/10.1016/j.matlet.2016.07.152.

[8] R. He, G. Schierning, K. Nielsch, Thermoelectric Devices: A Review of Devices, Architectures, and Contact Optimization, Adv. Mater. Technol. 3 (2018).

https://doi.org/10.1002/admt.201700256.

[9] C. Oztan, R. Welch, S. Leblanc, Additive Manufacturing of Bulk Thermoelectric Architectures: A Review, Energies. 15 (2022). https://doi.org/10.3390/en15093121.

[10] J.J. Lewandowski, M. Seifi, Metal Additive Manufacturing: A Review of Mechanical Properties, Annu. Rev. Mater. Res. 46 (2016) 151–186. https://doi.org/10.1146/annurev-matsci-070115-032024.

[11] N. Hrabe, T. Quinn, Effects of processing on microstructure and mechanical properties of a titanium alloy (Ti-6Al-4V) fabricated using electron beam melting (EBM), Part 2: Energy input, orientation, and location, Mater. Sci. Eng. A. 573 (2013) 271–277. https://doi.org/10.1016/j.msea.2013.02.065.

[12] L.E. Murr, E. V. Esquivel, S.A. Quinones, S.M. Gaytan, M.I. Lopez, E.Y. Martinez, F. Medina, D.H. Hernandez, E. Martinez, J.L. Martinez, S.W. Stafford, D.K. Brown, T. Hoppe, W. Meyers, U. Lindhe, R.B. Wicker, Microstructures and mechanical properties of electron beam-rapid manufactured Ti-6Al-4V biomedical prototypes compared to wrought Ti-6Al-4V, Mater. Charact. 60 (2009) 96–105. https://doi.org/10.1016/j.matchar.2008.07.006.

[13] G. Kasperovich, J. Hausmann, Improvement of fatigue resistance and ductility of TiAl6V4 processed by selective laser melting, J. Mater. Process. Technol. 220 (2015) 202–214. https://doi.org/10.1016/j.jmatprotec.2015.01.025.

[14] D. Greitemeier, C. Dalle Donne, F. Syassen, J. Eufinger, T. Melz, Effect of surface roughness on fatigue performance of additive manufactured Ti–6Al–4V, Mater. Sci. Technol. (United Kingdom). 32 (2016) 629–634. https://doi.org/10.1179/1743284715Y.0000000053.

[15] P. Edwards, A. O'Conner, M. Ramulu, Electron beam additive manufacturing of titanium components: Properties and performance, J. Manuf. Sci. Eng. 135 (2013) 1–7. https://doi.org/10.1115/1.4025773.

[16] X. Tan, Y. Kok, Y.J. Tan, M. Descoins, D. Mangelinck, S.B. Tor, K.F. Leong, C.K. Chua, Graded microstructure and mechanical properties of additive manufactured Ti-6Al-4V via electron beam melting, Acta Mater. 97 (2015) 1–16. https://doi.org/10.1016/j.actamat.2015.06.036.

[17] O.L. Rodriguez, P.G. Allison, W.R. Whittington, D.K. Francis, O.G. Rivera, K. Chou, X. Gong, T.M. Butler, J.F. Burroughs, Dynamic tensile behavior of electron beam additive manufactured Ti6Al4V, Mater. Sci. Eng. A. 641 (2015) 323–327. https://doi.org/10.1016/j.msea.2015.06.069.

[18] P. Edwards, M. Ramulu, Fatigue performance evaluation of selective laser melted Ti-6Al-4V, Mater. Sci. Eng. A. 598 (2014) 327–337. https://doi.org/10.1016/j.msea.2014.01.041.

[19] S. Leuders, T. Lieneke, S. Lammers, T. Tröster, T. Niendorf, On the fatigue properties of metals manufactured by selective laser melting - The role of ductility, J. Mater. Res. 29 (2014) 1911–1919. https://doi.org/10.1557/jmr.2014.157.

[20] P. Edwards, M. Ramulu, Effect of build direction on the fracture toughness and fatigue crack growth in selective laser melted Ti-6Al-4-‰V, Fatigue Fract. Eng. Mater. Struct. 38 (2015) 1228–1236. https://doi.org/10.1111/ffe.12303.

[21] B. Van Hooreweder, D. Moens, R. Boonen, J.P. Kruth, P. Sas, Analysis of fracture toughness and crack propagation of Ti6Al4V produced by selective laser melting, Adv. Eng. Mater. 14 (2012) 92–97. https://doi.org/10.1002/adem.201100233.

[22] A. El-Desouky, M. Carter, M. Mahmoudi, A. Elwany, S. LeBlanc, Influences of energy

density on microstructure and consolidation of selective laser melted bismuth telluride thermoelectric powder, J. Manuf. Process. 25 (2017) 411–417. https://doi.org/10.1016/j.jmapro.2016.12.008.

[23] Y. Zheng, T.J. Slade, L. Hu, X.Y. Tan, Y. Luo, Z.-Z. Luo, J. Xu, Q. Yan, M.G. Kanatzidis, Defect engineering in thermoelectric materials: what have we learned?, Chem. Soc. Rev. 50 (2021) 9022–9054. https://doi.org/10.1039/d1cs00347j.

[24] Y. Mao, Y. Yan, K. Wu, H. Xie, Z. Xiu, J. Yang, Q. Zhang, C. Uher, X. Tang, Non-equilibrium synthesis and characterization of n-type Bi2Te2.7Se0.3 thermoelectric material prepared by rapid laser melting and solidification, RSC Adv. 7 (2017) 21439–21445. https://doi.org/10.1039/c7ra02677c.

[25] Y. Thimont, S. Leblanc, The impact of thermoelectric leg geometries on thermal resistance and power output, J. Appl. Phys. 126 (2019). https://doi.org/10.1063/1.5115044.

[26] Q. Zhang, B. Gu, Y. Wu, T. Zhu, T. Fang, Y. Yang, J. Liu, B. Ye, X. Zhao, Evolution of the Intrinsic Point Defects in Bismuth Telluride-Based Thermoelectric Materials, ACS Appl. Mater. Interfaces. 11 (2019) 41424–41431. https://doi.org/10.1021/acsami.9b15198.

[27] T.J. Zhu, L.P. Hu, X.B. Zhao, J. He, New insights into intrinsic point defects in v2vi3 thermoelectric materials, Adv. Sci. 3 (2016). https://doi.org/10.1002/advs.201600004.

[28] R. Welch, D. Hobbis, A.J. Birnbaum, G. Nolas, S. LeBlanc, Nano- and Micro-Structures Formed during Laser Processing of Selenium Doped Bismuth Telluride, Adv. Mater. Interfaces. 8 (2021). https://doi.org/10.1002/admi.202100185.

[29] S. Leblanc, S.K. Yee, M.L. Scullin, C. Dames, K.E. Goodson, Material and manufacturing cost considerations for thermoelectrics, Renew. Sustain. Energy Rev. 32 (2014) 313–327.

https://doi.org/10.1016/j.rser.2013.12.030.

[30] S. LeBlanc, Thermoelectric generators: Linking material properties and systems engineering for waste heat recovery applications, Sustain. Mater. Technol. 1 (2014) 26–35. https://doi.org/10.1016/j.susmat.2014.11.002.

[31] H. Zhang, D. Hobbis, G.S. Nolas, S. Leblanc, Laser additive manufacturing of powdered bismuth telluride, J. Mater. Res. 33 (2018) 4031–4039. https://doi.org/10.1557/jmr.2018.390.

[32] T. DebRoy, H.L. Wei, J.S. Zuback, T. Mukherjee, J.W. Elmer, J.O. Milewski, A.M. Beese, A. Wilson-Heid, A. De, W. Zhang, Additive manufacturing of metallic components – Process, structure and properties, Prog. Mater. Sci. 92 (2018) 112–224. https://doi.org/10.1016/j.pmatsci.2017.10.001.

[33] H.L. Wei, T. Mukherjee, W. Zhang, J.S. Zuback, G.L. Knapp, A. De, T. DebRoy, Mechanistic models for additive manufacturing of metallic components, Prog. Mater. Sci. 116 (2021). https://doi.org/10.1016/j.pmatsci.2020.100703.

[34] R.R. Dehoff, M. Kirka, W.J. Sames, H. Bilheux, A.S. Tremsin, L.E. Lowe, S.S. Babu, Site specific control of crystallographic grain orientation through electron beam additive manufacturing, Mater. Sci. Technol. (United Kingdom). 31 (2015) 931–938. https://doi.org/10.1179/1743284714Y.0000000734.

[35] T. Ishimoto, S. Wu, Y. Ito, S.H. Sun, H. Amano, T. Nakano, Crystallographic orientation control of 316L austenitic stainless steel via selective laser melting, ISIJ Int. 60 (2020) 1758–1764. https://doi.org/10.2355/isijinternational.ISIJINT-2019-744.

[36] O. Gokcekaya, N. Hayashi, T. Ishimoto, K. Ueda, T. Narushima, T. Nakano, Crystallographic orientation control of pure chromium via laser powder bed fusion and

improved high temperature oxidation resistance, Addit. Manuf. 36 (2020) 101624. https://doi.org/10.1016/j.addma.2020.101624.

[37] C. Oztan, B. Şişik, R. Welch, S. LeBlanc, Process-microstructure relationship of laser processed thermoelectric material Bi2Te3, Front. Electron. Mater. 2 (2022) 1–15. https://doi.org/10.3389/femat.2022.1046694.

[38] J.P. Oliveira, T.G. Santos, R.M. Miranda, Revisiting fundamental welding concepts to improve additive manufacturing: From theory to practice, Prog. Mater. Sci. 107 (2020) 100590. https://doi.org/10.1016/j.pmatsci.2019.100590.

[39] Z. Zhu, W. Li, Q.B. Nguyen, X. An, W. Lu, Z. Li, F.L. Ng, S.M. Ling Nai, J. Wei, Enhanced strength–ductility synergy and transformation-induced plasticity of the selective laser melting fabricated 304L stainless steel, Addit. Manuf. 35 (2020) 101300. https://doi.org/10.1016/j.addma.2020.101300.

[40] Y. Li, K. Chen, R.L. Narayan, U. Ramamurty, Y. Wang, J. Long, N. Tamura, X. Zhou, Multi-scale microstructural investigation of a laser 3D printed Ni-based superalloy, Addit. Manuf. 34 (2020) 101220. https://doi.org/10.1016/j.addma.2020.101220.

[41] B. Şişik, S. LeBlanc, The Influence of Leg Shape on Thermoelectric Performance Under Constant Temperature and Heat Flux Boundary Conditions, Front. Mater. 7 (2020) 1–13. https://doi.org/10.3389/fmats.2020.595955.

[42] T.J. Horn, O.L.A. Harrysson, Overview of current additive manufacturing technologies and selected applications, Sci. Prog. 95 (2012) 255–282. https://doi.org/10.3184/003685012X13420984463047.

[43] G. Li, Q. An, B. Duan, L. Borgsmiller, M. Al Malki, M. Agne, U. Aydemir, P. Zhai, Q. Zhang, S.I. Morozov, W.A. Goddard, G.J. Snyder, Fracture toughness of thermoelectric

materials, Mater. Sci. Eng. R Reports. 144 (2021) 1–12. https://doi.org/10.1016/j.mser.2021.100607.

[44] K. Wu, Y. Yan, J. Zhang, Y. Mao, H. Xie, J. Yang, Q. Zhang, C. Uher, X. Tang, Preparation of n-type Bi2Te3 thermoelectric materials by non-contact dispenser printing combined with selective laser melting, Phys. Status Solidi - Rapid Res. Lett. 11 (2017). https://doi.org/10.1002/pssr.201700067.

[45] S. Mondal, D. Gwynn, A. Ray, A. Basak, Investigation of melt pool geometry control in additive manufacturing using hybrid modeling, Metals (Basel). 10 (2020) 1–23. https://doi.org/10.3390/met10050683.

[46] R. Seede, D. Shoukr, B. Zhang, A. Whitt, S. Gibbons, P. Flater, A. Elwany, R. Arroyave, I. Karaman, An ultra-high strength martensitic steel fabricated using selective laser melting additive manufacturing: Densification, microstructure, and mechanical properties, Acta Mater. 186 (2020) 199–214. https://doi.org/10.1016/j.actamat.2019.12.037.

[47] M. Kusano, H. Kitano, M. Watanabe, Novel calibration strategy for validation of finite element thermal analysis of selective laser melting process using Bayesian optimization, Materials (Basel). 14 (2021). https://doi.org/10.3390/ma14174948.

[48] Z. Wang, C. Jiang, P. Liu, W. Yang, Y. Zhao, M.F. Horstemeyer, L.Q. Chen, Z. Hu, L. Chen, Uncertainty quantification and reduction in metal additive manufacturing, Npj Comput. Mater. 6 (2020). https://doi.org/10.1038/s41524-020-00444-x.

[49] J. Ye, M.S. Yasin, M. Muhammad, J. Liu, A. Vinel, D. Silva, N. Shamsaei, S. Shao, Bayesian Process Optimization for Additively Manufactured Nitinol, in: Solid Free. Fabr. 2021 Proc. 32nd Annu. Int., 2021: pp. 284–296. https://www.researchgate.net/publication/357031811.

[50] H. Kitano, M. Kusano, M. Tsujii, A. Yumoto, M. Watanabe, Process parameter optimization framework for the selective laser melting of hastelloy x alloy considering defects and solidification crack occurrence, Crystals. 11 (2021). https://doi.org/10.3390/cryst11060578.

[51] A. Agarwal, T. Banerjee, J. Gockel, S. LeBlanc, J. Walker, J. Middendorf, Predicting Thermoelectric Power Factor of Bismuth Telluride During Laser Powder Bed Fusion Additive Manufacturing, ArXiv E-Prints. (2023) arXiv:2303.15663. https://doi.org/10.48550/arXiv.2303.15663.

[52] B. Gould, S. Wolff, N. Parab, C. Zhao, M.C. Lorenzo-Martin, K. Fezzaa, A. Greco, T. Sun, In Situ Analysis of Laser Powder Bed Fusion Using Simultaneous High-Speed Infrared and X-ray Imaging, Jom. 73 (2021) 201–211. https://doi.org/10.1007/s11837-020-04291-5.

[53] N.D. Parab, C. Zhao, R. Cunningham, L.I. Escano, K. Fezzaa, W. Everhart, A.D. Rollett, L. Chen, T. Sun, Ultrafast X-ray imaging of laser–metal additive manufacturing processes, J. Synchrotron Radiat. 25 (2018) 1467–1477. https://doi.org/10.1107/S1600577518009554.

[54] J.P. Kruth, J. Deckers, E. Yasa, R. Wauthlé, Assessing and comparing influencing factors of residual stresses in selective laser melting using a novel analysis method, Proc. Inst. Mech. Eng. Part B J. Eng. Manuf. 226 (2012) 980–991. https://doi.org/10.1177/0954405412437085.

[55] H. Ali, H. Ghadbeigi, K. Mumtaz, Effect of scanning strategies on residual stress and mechanical properties of Selective Laser Melted Ti6Al4V, Mater. Sci. Eng. A. 712 (2018) 175–187. https://doi.org/10.1016/j.msea.2017.11.103.

[56] B. Efron, Bootstrap Methods: Another Look at the Jackknife BT - Breakthroughs in Statistics: Methodology and Distribution, in: S. Kotz, N.L. Johnson (Eds.), Springer New York, New York, NY, 1992: pp. 569–593. https://doi.org/10.1007/978-1-4612-4380-9_41.

[57] P. V. Balachandran, Adaptive machine learning for efficient materials design, MRS Bull. 45 (2020) 579–586. https://doi.org/10.1557/mrs.2020.163.

[58] D. Morgan, R. Jacobs, Opportunities and Challenges for Machine Learning in Materials Science, Annu. Rev. Mater. Res. 50 (2020) 71–103. https://doi.org/10.1146/annurev-matsci-070218-010015.

[59] L. Huelsenbeck, S. Jung, R. Herrera Del Valle, P. V. Balachandran, G. Giri, Accelerated HKUST-1 Thin-Film Property Optimization Using Active Learning, ACS Appl. Mater. Interfaces. 13 (2021) 61827–61837. https://doi.org/10.1021/acsami.1c20788.

[60] K. Nawa, K. Hagiwara, K. Nakamura, Prediction-accuracy improvement of neural network to ferromagnetic multilayers by Gaussian data augmentation and ensemble learning, Comput. Mater. Sci. 219 (2023) 112032. https://doi.org/10.1016/j.commatsci.2023.112032.

[61] A.J. Smola, B. Schölkopf, A tutorial on support vector regression, Stat. Comput. 14 (2004) 199–222. https://doi.org/10.1023/B:STCO.0000035301.49549.88.

[62] A. Karatzoglou, D. Meyer, K. Hornik, Support Vector Algorithm in R, J. Stat. Softw. 15 (2006) 1–28.

[63] Q. Guo, C. Zhao, M. Qu, L. Xiong, L.I. Escano, S.M.H. Hojjatzadeh, N.D. Parab, K. Fezzaa, W. Everhart, T. Sun, L. Chen, In-situ characterization and quantification of melt pool variation under constant input energy density in laser powder bed fusion additive manufacturing process, Addit. Manuf. 28 (2019) 600–609.

https://doi.org/10.1016/j.addma.2019.04.021.

[64] T. Wang, Y. Wang, C. Chen, H. Zhu, Relationships between the characteristics of porosity, melt pool and process parameters in laser powder bed fusion Al Zn alloy, J. Manuf. Process. 68 (2021) 1236–1244. https://doi.org/10.1016/j.jmapro.2021.06.027.

[65] C. Kusuma, S.H. Ahmed, A. Mian, R. Srinivasan, Effect of Laser Power and Scan Speed on Melt Pool Characteristics of Commercially Pure Titanium (CP-Ti), J. Mater. Eng. Perform. 26 (2017) 3560–3568. https://doi.org/10.1007/s11665-017-2768-6.

[66] S. Waqar, Q. Sun, J. Liu, K. Guo, J. Sun, Numerical investigation of thermal behavior and melt pool morphology in multi-track multi-layer selective laser melting of the 316L steel, Int. J. Adv. Manuf. Technol. 112 (2021) 879–895. https://doi.org/10.1007/s00170-020-06360-0.

[67] J.J.S. Dilip, S. Zhang, C. Teng, K. Zeng, C. Robinson, D. Pal, B. Stucker, Influence of processing parameters on the evolution of melt pool, porosity, and microstructures in Ti-6Al-4V alloy parts fabricated by selective laser melting, Prog. Addit. Manuf. 2 (2017) 157–167. https://doi.org/10.1007/s40964-017-0030-2.

[68] E. Hüllermeier, W. Waegeman, Aleatoric and epistemic uncertainty in machine learning: an introduction to concepts and methods, Springer US, 2021. https://doi.org/10.1007/s10994-021-05946-3.

[69] A. Possolo, Simple Guide for Evaluating and Expressing the Uncertainty of NIST Measurement Results, Washington, DC, 2015. http://dx.doi.org/10.6028/NIST.TN.1900.

[70] R. Cunningham, C. Zhao, N. Parab, C. Kantzos, J. Pauza, K. Fezzaa, T. Sun, A.D. Rollett, Keyhole threshold and morphology in laser melting revealed by ultrahigh-speed x-ray imaging, Science (80-.). 363 (2019) 849–852. https://doi.org/10.1126/science.aav4687.

[71] J. Bustillos, J. Kim, A. Moridi, Exploiting lack of fusion defects for microstructural engineering in additive manufacturing, Addit. Manuf. 48 (2021) 102399. https://doi.org/10.1016/j.addma.2021.102399.

[72] S.P. Narra, A.D. Rollett, A. Ngo, D. Scannapieco, M. Shahabi, T. Reddy, J. Pauza, H. Taylor, C. Gobert, E. Diewald, F.X. Dugast, A. To, R. Wicker, J. Beuth, J.J. Lewandowski, Process qualification of laser powder bed fusion based on processing-defect structure-fatigue properties in Ti-6Al-4V, J. Mater. Process. Technol. 311 (2023) 117775. https://doi.org/10.1016/j.jmatprotec.2022.117775.

[73] C. V Headley, R.J. Herrera del Valle, J. Ma, P. Balachandran, V. Ponnambalam, S. LeBlanc, D. Kirsch, J.B. Martin, The development of an augmented machine learning approach for the additive manufacturing of thermoelectric materials, J. Manuf. Process. 116 (2024) 165–175. https://doi.org/https://doi.org/10.1016/j.jmapro.2024.02.045.

[74] R. Deng, X. Su, T. Luo, J. Li, W. Liu, Y. Yan, X. Tang, Modulation of carrier concentration and microstructure for high performance BixSb2-xTe3 thermoelectrics prepared by rapid solidification, J. Solid State Chem. 264 (2018) 141–147. https://doi.org/10.1016/j.jssc.2018.04.038.

[75] L. Hu, T. Zhu, X. Liu, X. Zhao, Point defect engineering of high-performance bismuth-telluride-based thermoelectric materials, Adv. Funct. Mater. 24 (2014) 5211–5218. https://doi.org/10.1002/adfm.201400474.

[76] W. Cai, W.D. Nix, Imperfections in Crystalline Solids, 1st Editio, Cambridge University Press, 2016. https://doi.org/10.1017/cbo9781316389508.

[77] W.D. Callister, D.G. Rethwisch, Materials Science and Engineering, Ninth, John Wiley & Sons, Inc., 2014.

[78] P. Rudolph, Fundamentals and engineering of defects, Prog. Cryst. Growth Charact. Mater. 62 (2016) 89–110. https://doi.org/10.1016/j.pcrysgrow.2016.04.004.

[79] J. Kansy, A. Hanc, D. Giebel, The influence of heat treatment on point defect concentration in Fe-Al and Fe-Al-Cr systems, Nukleonika. 55 (2010) 21–25.

[80] H.F. He, X.F. Li, Z.Q. Chen, Y. Zheng, D.W. Yang, X.F. Tang, Interplay between point defects and thermal conductivity of chemically synthesized Bi2te3nanocrystals studied by positron annihilation, J. Phys. Chem. C. 118 (2014) 22389–22394. https://doi.org/10.1021/jp508085a.

[81] H. Yao, R. Katona, J. Zhou, M.I. Islam, J. Raush, F. Lu, S. Guo, Defects evaluation of selective laser melting stainless steel 316 parts using Positron Annihilation Lifetime measurement, ASME Int. Mech. Eng. Congr. Expo. Proc. 8B-2018 (2018). https://doi.org/10.1115/imece2018-86729.

[82] S. Li, H.M.A. Soliman, J. Zhou, M.S. Toprak, M. Muhammed, D. Platzek, P. Ziolkowski, E. Müller, Effects of annealing and doping on nanostructured bismuth telluride thick films, Chem. Mater. 20 (2008) 4403–4410. https://doi.org/10.1021/cm800696h.

[83] T. Feng, B. Qiu, X. Ruan, Coupling between phonon-phonon and phonon-impurity scattering: A critical revisit of the spectral Matthiessen's rule, Phys. Rev. B - Condens. Matter Mater. Phys. 92 (2015) 1–5. https://doi.org/10.1103/PhysRevB.92.235206.

[84] J. He, The Roles of Grain Boundaries in Thermoelectric Transports, Mater. Lab. 1 (2022) 1–6. https://doi.org/10.54227/mlab.20220012.

[85] M.G. Holland, Phonon scattering in semiconductors from thermal conductivity studies, Phys. Rev. 134 (1964). https://doi.org/10.1103/PhysRev.134.A471.

[86] G.J. Snyder, E.S. Toberer, Complex TE meterials, Nat. Mater. 7 (2008) 105–114.

[87] C. Hu, K. Xia, C. Fu, X. Zhao, T. Zhu, Carrier grain boundary scattering in thermoelectric materials, Energy Environ. Sci. 15 (2022) 1406–1422. https://doi.org/10.1039/d1ee03802h.

[88] X. Meng, Z. Liu, B. Cui, D. Qin, H. Geng, W. Cai, L. Fu, J. He, Z. Ren, J. Sui, Grain Boundary Engineering for Achieving High Thermoelectric Performance in n-Type Skutterudites, Adv. Energy Mater. 7 (2017). https://doi.org/10.1002/aenm.201602582.

[89] S. Il Kim, K.H. Lee, H.A. Mun, H.S. Kim, S.W. Hwang, J.W. Roh, D.J. Yang, W.H. Shin, X.S. Li, Y.H. Lee, G.J. Snyder, S.W. Kim, Dense dislocation arrays embedded in grain boundaries for high-performance bulk thermoelectrics, Science (80-.). 348 (2015) 109–114. https://doi.org/10.1126/science.aaa4166.

[90] Q. Zhang, Y. Lin, N. Lin, Y. Yu, F. Liu, C. Fu, B. Ge, O. Cojocaru-Mirédin, T. Zhu, X. Zhao, Enhancing the room temperature thermoelectric performance of n-type Bismuth-telluride-based polycrystalline materials by low-angle grain boundaries, Mater. Today Phys. 22 (2022). https://doi.org/10.1016/j.mtphys.2021.100573.

[91] C. Shao, H. Bao, Thermal transport in bismuth telluride quintuple layer: Mode-resolved phonon properties and substrate effects, Sci. Rep. 6 (2016) 2–11. https://doi.org/10.1038/srep27492.

[92] Z. Rashid, A.S. Nissimagoudar, W. Li, Phonon transport and thermoelectric properties of semiconducting Bi2Te2X (X = S, Se, Te) monolayers, Phys. Chem. Chem. Phys. 21 (2019) 5679–5688. https://doi.org/10.1039/c8cp05793a.

[93] O. Hellman, D.A. Broido, Phonon thermal transport in Bi2 Te3 from first principles, Phys. Rev. B - Condens. Matter Mater. Phys. 90 (2014) 1–7. https://doi.org/10.1103/PhysRevB.90.134309.

[94] Y. Wang, B. Qiu, A.J.H. McGaughey, X. Ruan, X. Xu, Mode-wise thermal conductivity of bismuth telluride, J. Heat Transfer. 135 (2013) 1–6. https://doi.org/10.1115/1.4024356.

[95] H. Zhang, C. Li, G. Yao, Y. Shi, Y. Zhang, Effect of annealing treatment on microstructure evolution and deformation behavior of 304 L stainless steel made by laser powder bed fusion, Int. J. Plast. 155 (2022) 103335. https://doi.org/10.1016/j.ijplas.2022.103335.

[96] T. Voisin, J.B. Forien, A. Perron, S. Aubry, N. Bertin, A. Samanta, A. Baker, Y.M. Wang, New insights on cellular structures strengthening mechanisms and thermal stability of an austenitic stainless steel fabricated by laser powder-bed-fusion, Acta Mater. 203 (2021). https://doi.org/10.1016/j.actamat.2020.11.018.

[97] J.J. Shen, T.J. Zhu, X.B. Zhao, S.N. Zhang, S.H. Yang, Z.Z. Yin, Recrystallization induced in situ nanostructures in bulk bismuth antimony tellurides: A simple top down route and improved thermoelectric properties, Energy Environ. Sci. 3 (2010) 1519–1523. https://doi.org/10.1039/c0ee00012d.

[98] M.W. Lee, P. Dharmaiah, C.H. Lee, S.H. Song, J.H. Lee, S.J. Hong, Recrystallization stimulated hierarchical structures for the simultaneous enhancement of Seebeck coefficient and electrical conductivity in Bi-Sb-Te alloys, J. Alloys Compd. 842 (2020) 155804. https://doi.org/10.1016/j.jallcom.2020.155804.

[99] Q. Hu, W. Qiu, J. Guo, X. Wu, L. Wu, J. Tang, Boosting thermoelectric performance of n-type Bi2Te2.7Se0.3 alloy by 3D printing induced in-situ texture engineering, J. Alloys Compd. 937 (2023). https://doi.org/10.1016/j.jallcom.2022.168172.

[100] H. Wang, S. Bai, L. Chen, A. Cuenat, G. Joshi, H. Kleinke, J. König, H.W. Lee, J. Martin, M.W. Oh, W.D. Porter, Z. Ren, J. Salvador, J. Sharp, P. Taylor, A.J. Thompson, Y.C.

Tseng, International Round-Robin Study of the Thermoelectric Transport Properties of an n-Type Half-Heusler Compound from 300 K to 773 K, J. Electron. Mater. 44 (2015) 4482–4491. https://doi.org/10.1007/s11664-015-4006-z.

[101] X. Ji, J. He, Z. Su, N. Gothard, T.M. Tritt, Improved thermoelectric performance in polycrystalline p -type Bi2 Te3 via an alkali metal salt hydrothermal nanocoating treatment approach, J. Appl. Phys. 104 (2008). https://doi.org/10.1063/1.2963706.

[102] M.J. Kirkham, A.M. Dos Santos, C.J. Rawn, E. Lara-Curzio, J.W. Sharp, A.J. Thompson, Abinitio determination of crystal structures of the thermoelectric material MgAgSb, Phys. Rev. B - Condens. Matter Mater. Phys. 85 (2012) 1–7. https://doi.org/10.1103/PhysRevB.85.144120.

[103] P. Gill, T.T. Moghadam, B. Ranjbar, Differential scanning calorimetry techniques: applications in biology and nanoscience., J. Biomol. Tech. 21 (2010) 167–193.

[104] R. Auguste, M.O. Liedke, F.A. Selim, B.P. Uberuaga, A. Wagner, P. Hosemann, Measurement and Simulation of Vacancy Formation in 2-MeV Self-irradiated Pure Fe, Jom. 72 (2020) 2436–2444. https://doi.org/10.1007/s11837-020-04116-5.

[105] S.S. Huang, T. Yoshiie, Q. Xu, K. Sato, T.D. Troev, Positron annihilation studies of electron-irradiated F82H model alloys, J. Nucl. Mater. 440 (2013) 617–621. https://doi.org/10.1016/j.jnucmat.2013.05.015.

[106] F. Tuomisto, Identification of Point Defects in Multielement Compounds and Alloys with Positron Annihilation Spectroscopy: Challenges and Opportunities, Phys. Status Solidi - Rapid Res. Lett. 15 (2021). https://doi.org/10.1002/pssr.202100177.

[107] H. Schut, A. Van Veen, G.F.A. Van De Walle, A.A.V. Gorkum, Positron beam defect profiling of silicon epitaxial layers, J. Appl. Phys. 70 (1991) 3003–3006.

https://doi.org/10.1063/1.349329.

[108] I. Miccoli, F. Edler, H. Pfnür, C. Tegenkamp, The 100th anniversary of the four-point probe technique: The role of probe geometries in isotropic and anisotropic systems, J. Phys. Condens. Matter. 27 (2015). https://doi.org/10.1088/0953-8984/27/22/223201.

[109] P.M. Hemenger, Measurement of High Resistivity Semiconductors Using the van der Pauw Method, 44 (1973) 698–700.

[110] F.S. Oliveira, R.B. Cipriano, F.T. Silva, E.C. Romão, C.A.M. Santos, Simple analytical method for determining electrical resistivity and sheet resistance using the van der Pauw procedure, Sci. Rep. 10 (2020) 1–8. https://doi.org/10.1038/s41598-020-72097-1.

[111] J. Martin, Z.Q. Lu, W. Wong-Ng, S. Krylyuk, D. Wang, Z. Ren, Development of a high-temperature (295–900 K) Seebeck coefficient Standard Reference Material, J. Mater. Res. 36 (2021) 3339–3352. https://doi.org/10.1557/s43578-021-00362-8.

[112] Y. Zheng, Q. Zhang, X. Su, H. Xie, S. Shu, T. Chen, G. Tan, Y. Yan, X. Tang, C. Uher, G.J. Snyder, Mechanically robust BiSbTe alloys with superior thermoelectric performance: A case study of stable hierarchical nanostructured thermoelectric materials, Adv. Energy Mater. 5 (2015) 1–11. https://doi.org/10.1002/aenm.201401391.

[113] S. Kasap, Principles of Electronic Materials and Devices, Third, McGraw-Hill Education, 2005.

[114] V. Lordi, P. Erhart, D. Åberg, Charge carrier scattering by defects in semiconductors, Phys. Rev. B - Condens. Matter Mater. Phys. 81 (2010) 1–7. https://doi.org/10.1103/PhysRevB.81.235204.

[115] N. Ma, D. Jena, Charge scattering and mobility in atomically thin semiconductors, Phys. Rev. X. 4 (2014) 1–9. https://doi.org/10.1103/PhysRevX.4.011043.

[116] Y. Anno, M. Takeuchi, M. Matsuoka, K. Takei, S. Akita, T. Arie, Effect of defect-induced carrier scattering on the thermoelectric power of graphene, Appl. Phys. Lett. 110 (2017). https://doi.org/10.1063/1.4989820.

[117] V.D. Das, N. Soundararajan, Size and temperature effects on the thermoelectric power and electrical resistivity of bismuth telluride thin films, Phys. Rev. B. 37 (1988) 4552–4559.

[118] H.J. Goldsmid, The electrical conductivity and thermoelectric power of bismuth telluride, Proc. Phys. Soc. 71 (1958) 633–646. https://doi.org/10.1088/0370-1328/71/4/312.

[119] A. Mavrokefalos, A.L. Moore, M.T. Pettes, L. Shi, W. Wang, X. Li, Thermoelectric and structural characterizations of individual electrodeposited bismuth telluride nanowires, J. Appl. Phys. 105 (2009). https://doi.org/10.1063/1.3133145.

[120] S. Yang, H. Ming, D. Li, T. Chen, S. Li, J. Zhang, H. Xin, X. Qin, Enhanced phonon scattering and thermoelectric performance for N-type Bi2Te2.7Se0.3 through incorporation of conductive polyaniline particles, Chem. Eng. J. 455 (2023). https://doi.org/10.1016/j.cej.2022.140923.

[121] M.T. Pettes, J. Maassen, I. Jo, M.S. Lundstrom, L. Shi, Effects of surface band bending and scattering on thermoelectric transport in suspended bismuth telluride nanoplates, Nano Lett. 13 (2013) 5316–5322. https://doi.org/10.1021/nl402828s.

[122] D. Jena, A.C. Gossard, U.K. Mishra, Dislocation scattering in a two-dimensional electron gas, Appl. Phys. Lett. 76 (2000) 1707–1709. https://doi.org/10.1063/1.126143.

[123] H. Eskandari Sabzi, P.E.J. Rivera-Díaz-del-Castillo, Composition and process parameter dependence of yield strength in laser powder bed fusion alloys, Mater. Des. 195 (2020) 109024. https://doi.org/10.1016/j.matdes.2020.109024.

[124] Y.M. Wang, T. Voisin, J.T. McKeown, J. Ye, N.P. Calta, Z. Li, Z. Zeng, Y. Zhang, W.

Chen, T.T. Roehling, R.T. Ott, M.K. Santala, P.J. Depond, M.J. Matthews, A. V. Hamza, T. Zhu, Additively manufactured hierarchical stainless steels with high strength and ductility, Nat. Mater. 17 (2018) 63–70. https://doi.org/10.1038/NMAT5021.

[125] M.A. Galindo-Fernández, K. Mumtaz, P.E.J. Rivera-Díaz-del-Castillo, E.I. Galindo-Nava, H. Ghadbeigi, A microstructure sensitive model for deformation of Ti-6Al-4V describing Cast-and-Wrought and Additive Manufacturing morphologies, Mater. Des. 160 (2018) 350–362. https://doi.org/10.1016/j.matdes.2018.09.028.

[126] X. Tong, H. Zhang, D.Y. Li, Effect of Annealing Treatment on Mechanical Properties of Nanocrystalline α-iron: An Atomistic Study, Sci. Rep. 5 (2015) 1–7. https://doi.org/10.1038/srep08459.

[127] J. Dheepa, R. Sathyamoorthy, S. Velumani, A. Subbarayan, K. Natarajan, P.J. Sebastian, Electrical resistivity of thermally evaporated bismuth telluride thin films, Sol. Energy Mater. Sol. Cells. 81 (2004) 305–312. https://doi.org/10.1016/j.solmat.2003.11.008.

[128] Q. Hao, J. Garg, Review on Phonon Transport within Polycrystalline Materials, ES Mater. Manuf. 14 (2021) 36–50. https://doi.org/10.30919/esmm5f480.

[129] P.G. Klemens, The scattering of low-frequency lattice waves by static imperfections, Proc. Phys. Soc. Sect. A. 68 (1955) 1113–1128. https://doi.org/10.1088/0370-1298/68/12/303.

[130] D. Lee, S. Lee, B.S. An, T.H. Kim, C.W. Yang, J.W. Suk, S. Baik, Dependence of the In-Plane Thermal Conductivity of Graphene on Grain Misorientation, Chem. Mater. 29 (2017) 10409–10417. https://doi.org/10.1021/acs.chemmater.7b03821.

[131] E.M. Levin, Charge carrier effective mass and concentration derived from combination of Seebeck coefficient and Te 125 NMR measurements in complex tellurides, Phys. Rev. B. 93 (2016) 1–5. https://doi.org/10.1103/PhysRevB.93.245202.

[132] M. Cutler, J.F. Leavy, R.L. Fitzpatrick, Electronic transport in semimetallic cerium sulfide, Phys. Rev. 133 (1964). https://doi.org/10.1103/PhysRev.133.A1143.

[133] A. Hashibon, C. Elsässer, First-principles density functional theory study of native point defects in Bi2Te3, Phys. Rev. B - Condens. Matter Mater. Phys. 84 (2011) 14–16. https://doi.org/10.1103/PhysRevB.84.144117.

[134] J.J. Shen, L.P. Hu, T.J. Zhu, X.B. Zhao, The texture related anisotropy of thermoelectric properties in bismuth telluride based polycrystalline alloys, Appl. Phys. Lett. 99 (2011). https://doi.org/10.1063/1.3643051.

[135] R.A. Masut, C. André, D. Vasilevskiy, S. Turenne, Charge transport anisotropy in hot extruded bismuth telluride: Scattering by acoustic phonons, J. Appl. Phys. 128 (2020). https://doi.org/10.1063/5.0018016.

[136] T. Caillat, M. Carle, P. Pierrat, H. Scherrer, S. Scherrer, Thermoelectric properties of (BixSb1-x)2Te3 single crystal solid solutions grown by the T.H.M. method, J. Phys. Chem. Solids. 53 (1992) 1121–1129. https://doi.org/10.1016/0022-3697(92)90087-T.

[137] I.T. Witting, T.C. Chasapis, F. Ricci, M. Peters, N.A. Heinz, G. Hautier, G.J. Snyder, The Thermoelectric Properties of Bismuth Telluride, Adv. Electron. Mater. 5 (2019) 1–20. https://doi.org/10.1002/aelm.201800904.

[138] S. Kudo, S. Tanaka, K. Miyazaki, Y. Nishi, M. Takashiri, Anisotropic analysis of nanocrystalline bismuth telluride thin films treated by homogeneous electron beam irradiation, Mater. Trans. 58 (2017) 513–519. https://doi.org/10.2320/matertrans.M2016295.

[139] K. Yamauchi, M. Takashiri, Highly oriented crystal growth of nanocrystalline bismuth telluride thin films with anisotropic thermoelectric properties using two-step treatment, J.

Alloys Compd. 698 (2017) 977–983. https://doi.org/10.1016/j.jallcom.2016.12.284.

[140] O.E. Femi, K. Akkiraju, B.S. Murthy, N. Ravishankar, K. Chattopadhyay, Effect of processing route on the bipolar contribution to the thermoelectric properties of n-type eutectic Bi22.5Sb7.5Te70 alloy, J. Alloys Compd. 682 (2016) 791–798. https://doi.org/10.1016/j.jallcom.2016.05.054.

[141] J.A. Gruber, S.A. Brown, G.A. Lucadamo, Generalized Kearns texture factors and orientation texture measurement, J. Nucl. Mater. 408 (2011) 176–182. https://doi.org/https://doi.org/10.1016/j.jnucmat.2010.11.031.

[142] D.S. Patil, R.R. Arakerimath, P. V. Walke, Thermoelectric materials and heat exchangers for power generation – A review, Renew. Sustain. Energy Rev. 95 (2018) 1–22. https://doi.org/10.1016/j.rser.2018.07.003.

[143] K. Hagihara, T. Ishimoto, M. Suzuki, R. Ozasa, A. Matsugaki, P. Wang, T. Nakano, Factor which governs the feature of texture developed during additive manufacturing; clarified from the study on hexagonal C40-NbSi2, Scr. Mater. 203 (2021) 114111. https://doi.org/10.1016/j.scriptamat.2021.114111.

[144] X. Wang, Y. Yang, L. Zhu, Effect of grain sizes and shapes on phonon thermal conductivity of bulk thermoelectric materials, J. Appl. Phys. 110 (2011). https://doi.org/10.1063/1.3611421.

[145] B. Poudel, Q. Hao, Y. Ma, Y. Lan, A. Minnich, B. Yu, X. Yan, D. Wang, A. Muto, D. Vashaee, X. Chen, J. Liu, M.S. Dresselhaus, G. Chen, Z. Ren, High-thermoelectric performance of nanostructured bismuth antimony telluride bulk alloys, Science (80-.). 320 (2008) 634–638. https://doi.org/10.1126/science.1156446.

[146] H. Wu, J. Carrete, Z. Zhang, Y. Qu, X. Shen, Z. Wang, L.D. Zhao, J.Q. He, Strong

enhancement of phonon scattering through nanoscale grains in lead sulfide thermoelectrics, NPG Asia Mater. 6 (2014). https://doi.org/10.1038/am.2014.39.

[147] S. wen Chen, S. ting Lu, J. shen Chang, Bi-In-Te phase diagram, J. Alloys Compd. 722 (2017) 499–508. https://doi.org/10.1016/j.jallcom.2017.06.144.

[148] G.R. Miller, C.Y. Li, Evidence for the existence of antistructure defects in bismuth telluride by density measurements, J. Phys. Chem. Solids. 26 (1965) 173–177. https://doi.org/10.1016/0022-3697(65)90084-3.

[149] J. Horák, Z. Starý, P. Lošťák, J. Pancíř, Antisite defects in Sb2-xInxTe3 mixed crystals, J. Phys. Chem. Solids. 49 (1988) 191–198. https://doi.org/10.1016/0022-3697(88)90050-9.

[150] F. Liu, M. Zhang, P. Nan, X. Zheng, Y. Li, K. Wu, Z. Han, B. Ge, X. Zhao, C. Fu, T. Zhu, Unraveling the Origin of Donor-Like Effect in Bismuth–Telluride-Based Thermoelectric Materials, Small Sci. (2023) 1–11. https://doi.org/10.1002/smsc.202300082.

[151] Y.G. Yan, J. Martin, W. Wong-Ng, M. Green, X.F. Tang, A temperature dependent screening tool for high throughput thermoelectric characterization of combinatorial films, Rev. Sci. Instrum. 84 (2013). https://doi.org/10.1063/1.4830295.

[152] J. Martin, T. Tritt, C. Uher, High temperature Seebeck coefficient metrology, J. Appl. Phys. 108 (2010) 1–12. https://doi.org/10.1063/1.3503505.

[153] J. Martin, Protocols for the high temperature measurement of the Seebeck coefficient in thermoelectric materials, Meas. Sci. Technol. 24 (2013). https://doi.org/10.1088/0957-0233/24/8/085601.

[154] F. Venturi, R. Taylor, Additive Manufacturing in the Context of Repeatability and Reliability, J. Mater. Eng. Perform. 32 (2023) 6589–6609. https://doi.org/10.1007/s11665-023-07897-3.

[155] L. Dowling, J. Kennedy, S. O'Shaughnessy, D. Trimble, A review of critical repeatability and reproducibility issues in powder bed fusion, Mater. Des. 186 (2020) 108346. https://doi.org/10.1016/j.matdes.2019.108346.

[156] P.R. Gradl, D.C. Tinker, J. Ivester, S.W. Skinner, T. Teasley, J.L. Bili, Geometric feature reproducibility for laser powder bed fusion (L-PBF) additive manufacturing with Inconel 718, Addit. Manuf. 47 (2021) 102305. https://doi.org/10.1016/j.addma.2021.102305.

[157] D.J. Huang, H. Li, A machine learning guided investigation of quality repeatability in metal laser powder bed fusion additive manufacturing, Mater. Des. 203 (2021) 109606. https://doi.org/10.1016/j.matdes.2021.109606.

[158] A.E. Shupenev, I.S. Korshunov, A.G. Grigoryants, On the Pulsed-Laser Deposition of Bismuth-Telluride Thin Films on Polyimide Substrates, Semiconductors. 54 (2020) 378–382. https://doi.org/10.1134/S1063782620030173.

[159] G.S. Hegde, A.N. Prabhu, R.Y. Huang, Y.K. Kuo, Reduction in thermal conductivity and electrical resistivity of indium and tellurium co-doped bismuth selenide thermoelectric system, J. Mater. Sci. Mater. Electron. 31 (2020) 19511–19525. https://doi.org/10.1007/s10854-020-04383-7.

[160] J. Liu, P. Wen, Metal vaporization and its influence during laser powder bed fusion process, Mater. Des. 215 (2022) 110505. https://doi.org/10.1016/j.matdes.2022.110505.

[161] J.P. Oliveira, A.D. LaLonde, J. Ma, Processing parameters in laser powder bed fusion metal additive manufacturing, Mater. Des. 193 (2020) 1–12. https://doi.org/10.1016/j.matdes.2020.108762.

[162] W.E. King, H.D. Barth, V.M. Castillo, G.F. Gallegos, J.W. Gibbs, D.E. Hahn, C. Kamath, A.M. Rubenchik, Observation of keyhole-mode laser melting in laser powder-bed fusion

additive manufacturing, J. Mater. Process. Technol. 214 (2014) 2915–2925. https://doi.org/10.1016/j.jmatprotec.2014.06.005.

[163] Y. Mishima, Y. Kimura, S. Wng Kim, CHAPTER 11 - Enhancement of Thermoelectric Figure of Merit through Nanostructural Control on Intermetallic Semiconductors toward High-Temperature Applications, in: H. Hosono, Y. Mishima, H. Takezoe, K.J.D. MacKenzie, K. MacKenzie, Y. Mishima, H. Takezoe (Eds.), Nanomaterials, Elsevier Science Ltd, Oxford, 2006: pp. 383–418. https://doi.org/https://doi.org/10.1016/B978-008044964-7/50013-3.

[164] Z. Zhang, J.K. Yee, P.A. Sharma, N. Yang, E.J. Lavernia, Influence of porosity o. The transport properties of Bi2Te 3-based alloys by field-assisted sintering, J. Mater. Res. 28 (2013) 1853–1861. https://doi.org/10.1557/jmr.2013.99.

[165] J. Hu, X.A. Fan, C. Jiang, B. Feng, Q. Xiang, G. Li, Z. He, Y. Li, Introduction of porous structure: A feasible and promising method for improving thermoelectric performance of Bi2Te3 based bulks, J. Mater. Sci. Technol. 34 (2018) 2458–2463. https://doi.org/10.1016/j.jmst.2018.05.010.

[166] J.M. Schultz, J.P. McHugh, W.A. Tiller, Effects of heavy deformation and annealing on the electrical properties of Bi2Te3, J. Appl. Phys. 33 (1962) 2443–2450. https://doi.org/10.1063/1.1728990.

[167] T.M. Mower, M.J. Long, Mechanical behavior of additive manufactured, powder-bed laser-fused materials, Mater. Sci. Eng. A. 651 (2016) 198–213. https://doi.org/10.1016/j.msea.2015.10.068.

[168] Y.P. Yang, M. Jamshidinia, P. Boulware, S.M. Kelly, Prediction of microstructure, residual stress, and deformation in laser powder bed fusion process, Comput. Mech. 61

(2018) 599–615. https://doi.org/10.1007/s00466-017-1528-7.

[169] G. Gong, J. Ye, Y. Chi, Z. Zhao, Z. Wang, G. Xia, X. Du, H. Tian, H. Yu, C. Chen, Research status of laser additive manufacturing for metal: a review, J. Mater. Res. Technol. 15 (2021) 855–884. https://doi.org/10.1016/j.jmrt.2021.08.050.

[170] M.W. Terban, S.J.L. Billinge, Structural Analysis of Molecular Materials Using the Pair Distribution Function, Chem. Rev. 122 (2022) 1208–1272. https://doi.org/10.1021/acs.chemrev.1c00237.

[171] S.J.L. Billinge, The rise of the X-ray atomic pair distribution function method: A series of fortunate events, Philos. Trans. R. Soc. A Math. Phys. Eng. Sci. 377 (2019). https://doi.org/10.1098/rsta.2018.0413.